EXPERIMENTAL STUDY OF SATELLITE WAKES IN A SIMULATED IONOSPHERIC PLASMA

Thesis by

Donald L. Blumenthal

In Partial Fulfillment of the Requirements

For the Degree of

Doctor of Philosophy

California Institute of Technology

Pasadena, California

1970

(Submitted May 21, 1970)

ACKNOWLEDGMENTS

I would like to express my appreciation to Professor Miklos Sajben for his guidance, interest, and patience in the course of this research and to Professor Lester Lees for his guidance and supervision of certain phases of the theoretical work.

I would also like to thank the staff of the GALCIT Hypersonic Wind Tunnel, especially Mr. Henry Mazurowski, and the staff of the Aeronautics Machine Shop for their help and advice in the experimental program.

I wish to gratefully express my appreciation for the financial support of the McDonnell Douglas Corporation, the Rand Corporation, the California Institute of Technology and the National Science Foundation. Acknowledgment is also due to the Air Force Cambridge Research Laboratory which supported this research under Contract No. AF 33(615)-5012.

Finally, I would like to thank my wife, Heidi, who typed the rough draft of this thesis and who provided moral support throughout this endeavor, and Mrs. Virginia Conner who typed the final copy of this thesis.

ABSTRACT

Wakes of simple bodies (discs, strips) were investigated using an electrostatically accelerated stream of argon ions and electrons. Typical conditions are: beam ion energy is 80 eV, ion density is 10^7-10^8 cm^{-3}, electron temperature 1-3 eV, ion thermal speed very small compared to mean ion velocity. The dimensionless parameters closely approximate satellite flight conditions, with the exception of the electron-ion temperature ratio, which is near unity in flight and large in these experiments.

The dependence of principal near wake features (such as the large ion current peak on the centerline behind the body) on the shape of the body was investigated systematically. All trends can be explained qualitatively by recognizing the dominant role of those portions of the sheath where the free stream ion velocity is tangential to the body.

The far wake of a strip (downstream of the ion current peak) displays a decaying radial distribution on the scale of the body size, somewhat similar to what is expected from a neutral gas. For axial symmetric models, the far wake displays a small structure on the scale of the ion current peak. The evolution of these disturbances is qualitatively explained by a simple, linearized two fluid theory. These features are initiated by the interaction of the inwardly deflected ion streams behind the body. At least in certain regions of the flow field, this interaction involves two-humped ion distribution functions, which may play a role in the further development of the far wake.

Abstract (Cont'd)

The effects on the simulation of varying the vacuum chamber background pressure was also examined in detail.

TABLE OF CONTENTS

PART	TITLE	PAGE
	Acknowledgments	ii
	Abstract	iii
	Table of Contents	v
	List of Tables	viii
	List of Figures	ix
	List of Symbols	xiii
I.	INTRODUCTION	1
II.	APPARATUS AND PROCEDURES	12
	II. 1. The Ion Source	13
	II. 2. Chamber and Vacuum System	16
	II. 3. Models	18
	II. 4. Instrumentation	19
	II. 4. 1. The Langmuir Probe	20
	The Temperature Mode	21
	Ion Flux Mode	22
III.	THE PLASMA BEAM	24
	III. 1. Properties of the Beam	24
	III. 2. Effect of the Earth's Magnetic Field	26
	III. 3. Repeatability	27
IV.	INVESTIGATION OF THE NEAR WAKE	30
	IV. 1. Description of the Near Wake	31
	IV. 2. The Effects of Body Potention on the Near Wake	34
	IV. 3. Effect of Body Shape and Size	37

Table of Contents (Cont'd)

PART	TITLE	PAGE
	IV. 4. Effect of Electron Temperature	39
	IV. 5. A Crude Theory to Predict Peak Position	40
V.	THE FAR WAKE	43
	V. 1. A Theory for the Far Wake	45
	V. 1. 1. Deveopment of the Theory	45
	V. 1. 2. Application of the Theory	50
	V. 1. 3. The One-Dimensional (Strip) Case	52
	V. 1. 4. The Cylindrical (Disc) Case	54
	V. 1. 5. Effect of the Initial Velocity Distribution	55
	V. 1. 6. Effect of Non-Zero Ion Temperature	56
	V. 1. 7. Transformation to Steady State	56
	V. 2. Experimental Study of the Far Wake	57
	V. 2. 1. Effects of Electron Temperature and Ion Density	58
	V. 2. 2. Dependence of the Far Wake on Initial Conditions	60
VI.	EFFECT OF BACKGROUND PRESSURE ON THE SIMULATION OF SATELLITE WAKES	67
	VI. 1. Effects of Background Pressure on the Near Wake Structure	67
	VI. 2. Effects of Background Pressure and Slow Ions on the Far Wake	70
VII.	CONCLUSION	72
	Tables	76
	Figures	83

Table of Contents (Cont'd)

PART	TITLE	PAGE
	APPENDIX 1 -- First Generation Ion Source and Beam	129
	Figure	132
	APPENDIX 2 -- The Resonance Probe	133
	Figure	135
	APPENDIX 3 -- Effects of Pressure and Collisions	136
	Figure	141
	APPENDIX 4 -- Estimate of the Relative Magnitudes of the Electric Fields in the Void and Sheath Regions	142
	APPENDIX 5 -- Wakes of Segmented Sphere and Screen Models	145
	Segmented Sphere	145
	Screen	145
	Figures	147
	APPENDIX 6 -- Details of the Near Wake Theory of Chapter IV	152
	APPENDIX 7 -- Some Details of the Far Wake Solutions of Chapter V	157
	One Dimensional Case	157
	Cylindrical Case	160
	Figures	162
	REFERENCES	166

LIST OF TABLES

No.	Title	Page No.
1.1	Approximate Conditions in the Ionosphere and Lab	76
1.2	Dimensionless Parameters	77
2.1	Power Supply Settings for High and Low Mode	78
4.1	Experimental Conditions	79
5.1	Comparison of Conditions for Figs. 4.6 and 5.7	81

LIST OF FIGURES

Fig. No.	Title	Page No.
1.1	Schematic of the Wake of a Wide Body	83
2.1	Plasma Beam Source and Chamber	84
2.2	Photo of Facility	85
2.3	Schematic of Source	86
2.4	Photograph of Source	87
2.5	High Mode Circuit	88
2.6	Low Mode Circuit	89
2.7	Disc Model and Coordinate System	90
2.8	Strip Model and Coordinate System	91
2.9	Spherical Model. Center Section Can be Biased Separately	92
2.10	Guarded Langmuir Probe and Associated Circuit	93
2.11	Spherical Langmuir Probe	94
2.12	Langmuir Probe Curve Indicating Graphical Determination of Electron Temperature	95
3.1	Determination of Effective Origin of Source Flow Like Beams for Low Mode	96
3.2	Cross Section of a 54V Beam for Various Distances from Source. Z = 0 is 8" from Effective Origin, 9" from Source Grid.	97
3.3	Replot of Figure 3.2 to Show Source Flow Nature of Beam	98
3.4	Effect of the Earth's Magnetic Field on Electron Temperature	99
3.5	Comparison of Two Disc Wakes Taken Under Approximately the Same Conditions at Different Times	100
3.6	Continuation of Figure 3.5	101

List of Figures (Cont'd)

Fig. No.	Title	Page No.
4.1	Cross Section of a Typical Wake	102
4.2	Near Wake of a Slightly Negative Thin Disc	103
4.3	Far Wake of a Slightly Negative Thin Disc	104
4.4	Effect of Model Potential on the Wake of a Thin Disc (Axial Traces)	105
4.5	Near Wake of a Highly Negative Thin Disc	106
4.6	Far Wake of a Highly Negative Thin Disc	107
4.7	Comparison of Thin Disc and Strip Axial Traces	108
4.8	Near Wake of a Highly Negative Thin Strip	109
4.9	Far Wake of a Highly Negative Thin Strip	110
4.10	Comparison of Thick and Thin Disc Axial Traces	111
4.11	Near Wake of a Highly Negative Thick Disc	112
4.12	Far Wake of a Highly Negative Thick Disc	113
4.13	Schematic of Ion Trajectories in the Near Wake as Assumed for Theory	114
4.14	Comparison of Theoretical and Actual Peak Positions	115
5.1	Theoretical Development with Time of Wide One-Dimensional Disturbance (2b/h = 40)	116
5.2	Development of a One-Dimensional Disturbance (2b/h = 6)	117
5.3	Development of a Narrow Density Disturbance in a One-Dimensional Plasma (2b/h = 2)	118
5.4	Development of a Wide Cylindrical Density Disturbance (2b/h = 40)	119
5.5	Development of a Cylindrical Density Disturbance (2b/h = 6)	120

List of Figures (Cont'd)

Fig. No.	Title	Page No.
5.6	Development of a Cylindrical Density Disturbance with Zero and Non-zero Initial Velocity Perturbation	121
5.7	Far Wake of a Highly Negative Thin Disc for S = 31	122
5.8	Radial Ion Velocity and Axial Flux Profiles for the First Far Wake Traces of a Thin Disc and a Thin Strip	123
5.9	Theoretical Development of the Far Wake for an Initial Condition Similar to the Z/a = 6 Flux Profile of Figure 4.6. Radial Velocities are Assumed to be Zero at $\tau = 0$.	124
6.1	Dependence of the Near Wake of a Highly Negative Thin Disc on Background Pressure	125
6.2	Dependence of the Far Wake of a Highly Negative Thin Disc on Background Pressure	126
6.3	Effect of Background Pressure on the Wake of a Highly Negative Thin Disc (Axial Traces)	127
6.4	Effect of Background Pressure on the Wake of a Slightly Negative Thin Disc (Axial Traces)	128
A.1.1	First Generation Plasma Beam Source and Chamber	132
A.2.1	Resonance Probe and Circuitry	135
A.3.1	Electron and Secondary Ion Densities on the Axis 51 cm from Accelerator Grid of Original Source Compared to Estimates of Appendix 3	141
A.5.1	Effect of Model Potential Distribution on the Wake of a Segmented Sphere (Axial Traces)	147
A.5.2	Near Wake of a Floating Sphere	148
A.5.3	Far Wake of a Floating Sphere	149
A.5.4	Near Wake of a Slightly Negative Thin Disc-Shaped Screen	150
A.5.5	Far Wake of a Slightly Negative Thin Disc-Shaped Screen	151

List of Figures (Cont'd)

Fig. No.	Title	Page No.
A. 7. 1	Development of a One-Dimensional Step Function Density Disturbance (2b/h = 6)	162
A. 7. 2	Development of a One-Dimensional Step Function Density Disturbance (2b/h = 40)	163
A. 7. 3	Development of a Cylindrical Step Function Density Disturbance (2b/h = 6)	164
A. 7. 4	Development of a Cylindrical Step Function Density Disturbance (2b/h = 40).	165

LIST OF SYMBOLS

A	arbitrary constant
a	model radius perpendicular to flow
b	disturbance width for far wake theory
c	wave speed, $\sqrt{\frac{KT_e}{M_i}}$
E	electric field
E_s	electric field in sheath region
E_v	electric field in void region
e	charge of an electron
h	Debye length
h_0	freestream Debye length at model position
J	current to the probe
J_0	Bessel function
J_1	Bessel function
K	Boltzman's constant
k	transformed variable (see Chapter V. 1)
L	model length in streamwise direction
M_i	ion mass
N	normalized perturbation ion density, $N = \frac{N'}{N_{i0}} << 1$
N'	perturbation ion density
$\overline{N}$	transformed perturbation ion density (see Chapter V. 1)
N_f	fast ion density
N_i	ion density
N_{i0}	freestream ion density (theory) or freestream ion density at model position (experiment)

List of Symbols (Cont'd)

N_n	neutral density
n	electron density
n_e	electron density
n'	perturbation electron density, $\frac{n'}{n} \ll 1$
Q	collision cross section
Q_c	charge transfer cross section
Q_e	momentum transfer cross section
R	beam radius
R_e	electron Larmar radius
R_i	ion Larmar radius
r	radial probe position or radial coordinate
r'	$r-r_i$ (see Appendix 6)
r_i	initial radius of ion entering sheath region (Appendix 6)
r_p	probe radius
S	beam speed ratio, $S = \frac{U}{\sqrt{\frac{KT_e}{M_i}}}$
T_e	electron temperature
T_i	ion temperature
T_n	neutral temperature
t	time
U	beam velocity
U_Z	axial component of beam velocity
u_s	radial component of mean velocity of slow ions
V	radial velocity
v	radial perturbation velocity

List of Symbols (Cont'd)

v_0	amplitude of initial radial perturbation velocity ($v_0/c \ll 1$)
x	coordinate perpendicular to beam for strip model
x_{edge}	position at edge of deficit region in wake of strip model
Y_p	variable defined in Appendix 6
y	variable defined in Appendix 6
Z	axial coordinate measured from model position
Z_p	peak position
Z_0	position of effective origin of beam
z	radius from effective origin of source flow (Chapter III. 1)
α	body potential to beam energy ratio, $\alpha = -\frac{2e\,\varphi_M}{M_i\,U^2}$
α_1	first root of J_0, $\alpha_1 = 2.4048$
β	width of initial velocity disturbance (Chapter V)
β	variable defined in Appendix 6
β_0	variable defined in Appendix 6
ϵ	a small quantity, $\epsilon \ll 1$
ϵ_0	permittivity constant
θ	azimuthal coordinate (Fig. 2. 7)
λ	mean free path
λ_{i-i}	ion-ion mean free path
λ_{i-n}	ion-neutral mean free path
ξ	normalized coordinate, $\xi = x/h$
ρ	normalized coordinate, $\rho = r/h$
τ	normalized time, $\tau = \omega_{pi}\, t$

List of Symbols (Cont'd)

φ probe potential

φ_B potential through which beam ions are accelerated.

beam energy = $e\,\varphi_B$

φ_g ground potential relative to plasma potential

φ_M model potential

φ_P plasma potential relative to ground

ψ variable defined in Appendix 6, $\psi = \frac{dr}{dZ}$

ω $\left(\frac{k^2}{1+k^2}\right)^{\frac{1}{2}}$

ω_{p_i} ion plasma frequency $\omega_{p_i} = \left(\frac{N_{io}\, e^2}{M_i\, \epsilon_0}\right)^{\frac{1}{2}}$

I. INTRODUCTION

This study is an experimental and theoretical investigation of disturbances generated in the ionospheric plasma by artificial satellites, using a simulated, laboratory plasma environment. The motivation for the work stems from interest in microwave scattering from such disturbances, which is a potential diagnostic tool for satellite identification.[1,2] The satellite-plasma interaction is also of interest in the design and interpretation of ionospheric plasma property measurements carried out using on-board instruments. Finally, but perhaps most importantly, the flow of collision-free plasmas is a basic problem of plasma dynamics which justifies an examination in its own right.

The properties of the ionospheric plasma have been explored and described in great detail.[2,3] The characteristics relevant to this study are reviewed in Table 1.1. This investigation is concerned with the part of the ionosphere between 200 and 500 km above the Earth's surface. At these altitudes, neutral particles are mostly O and N_2 with densities of $O[10^9\ cm^{-3}]$. The charged particle density is $O[10^6\ cm^{-3}]$, heavy particle temperature is $O[1000^oK]$, while the electron temperature may range from the ion temperature up to roughly twice that value. The Earth's magnetic field is approximately 0.3 gauss, and typical orbital speeds are 8×10^4 m/sec. In this region the ion-ion and ion-neutral mean free paths are hundreds of meters, so that close collisions between particles can probably be ignored, except perhaps far downstream from the body. In case of large orbiting manned space platforms, however, collisions may

well play a significant role.

The ion gyro radii are several meters, while electron radii are only a few centimeters. Direct magnetic effects in the vicinity of the satellite are probably small, but they may be significant farther downstream in the wake, at distances comparable to the length traversed by an ion in the streamwise direction during one ion cyclotron period. The electrons are closely coupled to the field lines and may exert additional influence on the ions through space charge created electric fields. Magnetic effects are specifically excluded from the present investigation in the interest of concentrating on the case of pure electrostatic interaction.

Solar radiation gives rise to photoemission of electrons, depending upon the work function, geometry and other variables characterizing the satellite. These effects were neglected in this study, since no appreciable photoemission occurred in the experiments.

Below about 700 km, orbital speeds are much greater than the ion thermal speeds so that the ion flow around the satellite is hypersonic. On the other hand, the electron thermal speed is much larger than the satellite speed and therefore orbital bodies can be considered to be virtually at rest with respect to the electron fluid. The electron Debye length is of the order of a centimeter which is much smaller than most satellites. While the Debye length may be comparable to or smaller than antennae or booms attached to certain spacecraft, this case was not examined.

The dimensionless parameters governing this class of problems are well established. [2-4] The definitions and their values under ionospheric and laboratory conditions will be discussed below.

(a) The electron-ion temperature ratio T_e/T_i is roughly between one and two in the ionosphere and much larger than unity in the present experiments. This is the only parameter in the purely electrostatic problem which is not simulated well. The probable effects caused by temperature ratio variation will be discussed in Chapter V.

(b) A speed ratio is defined as the ratio of the relative speed between body and plasma to the ion acoustic wave speed: $S \equiv U/[\frac{K}{M_i}(T_e + T_i)]^{\frac{1}{2}}$. This parameter is O[10] in both cases, i. e., much larger than unity. In the experiment, $T_e/T_i \gg 1$, so that the wave speed is given by $(\frac{K}{M_i} T_e)^{\frac{1}{2}}$ to a good approximation. The speed ratio plays a role very similar to that of the Mach number in conventional gas dynamics.

(c) The intensity of the body-plasma interaction is measured by the ratio of body-plasma potential difference to the ion kinetic energy based on relative speed: $\alpha = (-\frac{2e\varphi_M}{M_i U^2})$, where φ_M is the body (model) potential relative to the plasma. Since φ_M is expected to be negative, $\alpha > 0$. Only conducting bodies were tested so that the potential was always constant over the surface. In flight, the net current to the satellite must clearly be zero, so that it assumes a moderate, floating potential, corresponding to $0 < \alpha \ll 1$. In the experiments, φ_M was controlled, allowing the exploration of the range $0 < \alpha < 0.7$, which clearly includes quite strong interactions.

(d) The geometry of the body is characterized in units of Debye length. Two parameters were used as a gross description of the body shape: L/h, the normalized streamwise body dimension and a/h, the normalized transverse dimension. In case of axial-symmetric bodies, a should be taken to be the largest body radius. As mentioned before, a/h and L/h are both large in most flight situations. For the bodies investigated, $a/h \gg 1$, while L/h varied from less than one to O[10], for reasons that will be made clear in the thesis.

(e) The presence of a magnetic field introduces the ratios of ion and electron gyro radii to the body radius: R_i/a, R_e/a, in addition to a specification of the field direction. Since simulation of magnetic effects was not attempted, these need not be discussed further.

(f) The ratios of all relevant mean free paths to the body radius are all much larger than unity for actual satellites. The shortest mean free path in the present experiment (ion-neutral charge exchange) was approximately 15 m, so that the collision-free nature of the flight was well simulated.

The various governing parameters and the inequalities obeyed by them in flight or in the laboratory are summarized in Table 1.2. The flight conditions given are appropriate for the 200-500 km altitude range.

It is clear from this discussion that the simulation is good, although not complete, since the possibly significant T_e/T_i ratio and the magnetic field effects are not reproduced. Many of the results

obtained are thus relevant to but not quantitatively characteristic of an actual ionospheric event. This is of no great concern, since the intent of this investigation was to gain a basic understanding of the mechanisms involved in this class of flow fields. This objective necessarily requires a separate examination of various factors in a way that involves the least possible amount of coupling among them. From this viewpoint, elimination of temperature ratio, magnetic field and photoemissive effects represents a simplification of the problem statement.

The experimental apparatus is a plasma wind tunnel in which the flow around stationary models can be examined. A plasma beam is generated by an electron bombardment ion engine which discharges into a vacuum chamber. This beam is composed of nearly mono-energetic argon ions and Maxwellian electrons. Most of the models used were brass discs of various diameters and thicknesses, although spheres and long strips were also tested for comparison. The wakes were probed with a spherical Langmuir probe.

The structure of the wakes of wide ($a/h \gg 1$) bodies has been explored qualitatively before. Fig. 1.1 is a schematic of such a wake for the idealized case of a parallel free stream, drawn on the basis of the available, concurring experimental evidence.

Ions which strike the body will be adsorbed (neutralized). If $\alpha > 0$, those ions which miss the body but pass through the Debye sheath region will be deflected toward the axis behind the model. If the model is axialsymmetric, a strong ion density peak will occur on the axis in the area where the ions are focused. In this region,

the density can be much greater than in the free stream. This large density disturbance decays farther downstream and spreads out in a wavelike fashion.

The wake is thus characterized by several regions. Immediately behind the model is a shadow region, from which the ions swept out by the model are missing. Downstream of this void is a region of high density which we call the peak region, downstream of which is the peak disturbance. Since ions are deflected toward the axis by the model, a rarefaction wave is formed, which propagates into the free stream at the "Mach" angle as in hypersonic gas dynamics. The domain bounded by this wave front on the outside and by the void and peak disturbance regions at small radii is characterized by reduced ion density and will be referred to as the defect or deficit region.

An alternate, somewhat looser subdivision of the entire wake pattern is to decompose it into near and far wakes, the dividing surface being a plane, perpendicular to the axis, somewhere in the vicinity of the peak.

The problem of plasma flow around satellites has been subjected to extensive theoretical,[1-17] observational[9, 18-20] and laboratory experimental[21-28] study. The related theoretical papers are far too numerous to be discussed here in detail. A good review of the literature until 1966 has been given by deLeeuw.[3] In general, the studies lean heavily towards numerical solutions of the Vlasov and Poisson's equations, concentrating mostly on the near wake region. From the recent literature, the work of Maslennikov and Sigov[17]

considers conditions reasonably representative of the present experiment. Their results show the shadow and peak regions, in qualitative agreement with observations of Skvortsov and Nosachev.[25]

Laboratory experimental studies to date have all been carried out using electrostatic ion accelerators of some type. They all produced conditions similar to the present experiment, although several workers used relatively high background pressures and the results must have been influenced by collisions between beam ions and background atoms. With minor variations, they all found the same general wake pattern, as shown on Fig. 1.1.

The most recent and comprehensive experimental investigation is that of Hester and Sonin.[27, 28] They presented the first detailed study of bodies small compared to the Debye length, including the far wake region. They were also the first to notice the wavelike behavior of the peak disturbance behind large axial symmetric bodies.

The contributions of the present work lie in several areas.

(a) The first attempts in this series of experiments were troubled by ion-atom charge exchange collisions. This fact led to an extensive investigation of the production of low energy ions by this mechanism as well as to their effects on both an undisturbed beam and the wakes of bodies. These effects are now reasonably well understood, and have been eliminated from all wake data reported here, except from those intended for the illustration of such effects. This investigation deviates from the main thrust of this thesis; nevertheless, it is of some value and is described

separately in Appendices 1 to 3.

(b) An important conclusion of this paper is that a simple two-fluid theory should provide a reasonably good description over most of the wake structure, excepting the region of the high ion flux peak. This conclusion is based on our experimental results; nevertheless it is expected to apply over a much wider range of parameters.

There are strong reasons why the two-fluid theory would not be expected to be true in the region of high ion flux. These reasons can probably be best explained in terms of the nature of the ion distribution function in the various wake regions.

In the free stream and the deficit regions the ions are cold, practically monoenergetic. In terms of velocity space, this means that the representative points are clustered closely around the point corresponding to the mean ion velocity. In the limit of zero ion temperature the trajectories of individual ions are identifiable with the streamlines of the ion fluid and the kinetic and fluid descriptions are, for all practical purposes, equivalent. The fluid model should be applicable in these areas.

The peak disturbance region is initiated by the interpenetration of the inward directed ion streams. In two dimensional flows, the representative points in velocity space congregate into two distinct groups, while in axial symmetric flows they cluster around a circle which lies perpendicular to the axial direction. Streamlines and trajectories are no longer identical and the details are no longer amenable to a fluid description.

It is not understood how this initial, grossly nonequilibrium configuration develops farther downstream. Since fluid models are not expected to hold if the distribution function is far from Maxwellian, one would not expect a moment description to be valid. It is therefore a surprising result, that the predictions of a fluid theory are reasonably close to the experimental results even in the peak disturbance region.

The reasons for this are not clear. One possible explanation may be the following: The distribution function that is expected to exist within the peak is suspected to be unstable. It is thus conceivable that an instability wipes out the initial distribution and causes the ions to relax to some near-Maxwellian distribution. This in turn could be described by a crude fluid model. This possibility was not investigated.

The applicability of the fluid model raises the hopes for successful analytical treatment of the problem within this framework.

(c) The ion flux peak behind the body is the most important feature of the near wake. Its location, width and magnitude largely determine the character of the far wake. In view of its importance, a detailed parametric study was carried out correlating the location and size of the peak with most parameters listed in this introduction. The results were found to agree reasonably well (within a factor of two or better) with a very crude theory. The theory was built around the supposition that the most important factor in determining the ion trajectories in the near wake is the electric field in the sheath

near to those parts of the body which are tangential to the ion stream (i. e., its contours as seen when looking downstream).

(d) Since the flow is hypersonic, the hypersonic analogy of continuum fluid mechanics was adopted to describe the far wake. In this analogy, the steady state, two-dimensional problem is transformed to a time dependent one-dimensional problem. The conditions presented by the near wake become the initial conditions of the transformed problem, the evolution of which is to be predicted.

The linearized version of the equations was solved by the Fourier transform technique for a variety of initial conditions, selected to approximate radial distributions measured shortly downstream of the peak. The solutions are wavelike in nature, and the details depend strongly on the shape of the initial ion density perturbation.

Due to some complexities present in the experiments but not built into the theory, the predictions were not exactly reproduced by the experiments. The relevant scales and trends were, however, in sufficiently good agreement to show the basic correctness of the theory.

The experimental apparatus and diagnostic techniques are described in Chapter II. Chapter III is devoted to the properties of the plasma beam generated by the apparatus. An unusual effect of the Earth's magnetic field on the electron temperature distribution in the beam is mentioned. The near wakes of wide models are discussed in Chapter IV, and the far wakes in Chapter V. Chapter VI

is concerned with the effects of charge exchange collisions on the wakes. Results and conclusions are summarized in Chapter VII and some suggestions for future work are presented.

II. APPARATUS AND PROCEDURES

The intent of this investigation was to produce a plasma beam which would simulate the ionosphere and to use this beam for the study of the charged particle wakes of satellites.

Ideally, a parallel, collisionless beam with no stray magnetic fields is desirable. At first, we attempted to achieve this end using a completely electrostatic source which employed no magnetic fields. This source had the disadvantage that in the pressure range within which it was able to function, a large number of low energy ions were produced by charge exchange collisions between the beam ions and the background atoms. To overcome this problem, a second generation ion engine was built, utilizing a small confining magnetic field which was capable of operating at considerably lower background pressures, thereby virtually eliminating low energy ions.

This chapter presents a description of this second generation source, along with the vacuum chamber in which it operates. The discussion includes the diagnostic equipment and methods, as well as the description of the models used. The original source was used only in the investigation of the effects of charge exchange collisions (see Chapter VI). It is described in Appendix I.

The facility consists of an ion source, a vacuum chamber and pumping equipment, a model suspension system, and a probe actuator. A schematic of the system is shown in Fig. 2.1. The source is completely enclosed in the vacuum chamber with electrical and cooling water feedthroughs on the chamber end wall. The models are suspended from a rod which goes through a port at the top of the chamber.

The probe actuator is manipulated from outside the chamber and has three degrees of freedom, so that the probe can be placed anywhere within about 13 cm of the chamber centerline. The pumping system is attached to ports in the bottom of the chamber. Since the beam is sensitive to the Earth's magnetic field, compensating coils are mounted outside the chamber. A photo of the facility is shown in Fig. 2.2. The various components of the facility will be discussed in more detail in the succeeding sections of this chapter.

II.1. The Ion Source

The source used in the wake investigations is an extremely simple electron bombardment ion engine designed with the help of the existing technology.[35-38]

A cross-sectional diagram of the source is shown on Fig. 2.3. It is similar to those used by Clayden and Hurdle [24] and Hester and Sonin.[27] Fig. 2.4 is a photograph of the engine with the front end partially removed. Argon is admitted at the rear end near the anode and is ionized by electrons emitted from the filament on the axis. The electrons are slowed in their migration toward the anode and thus kept in the source region longer by an axial magnetic field. This field is on the order of 20 gauss at the ion grid and increases in magnitude toward the rear of the source. At the model position the fringing field is negligible.

The plasma in the source tends to stay approximately at anode potential, and the ions formed are essentially thermal. Those ions which enter the sheath region next to the ion grid are accelerated toward the grid. The ions which go through the grid form the beam.

In order to maintain a stable beam, neutralizing electrons must be added to the ions issuing from the grid, which can be done in two ways. The conventional way is to immerse a hot electron emitting filament in the beam downstream of the grid. In this case the beam electrons will be close to Maxwellian at a temperature close to that of the hot filament. For a tungsten filament, this method gives a maximum electron temperature of about 1/4 volt. This mode of operation typically results in high speed ratios: $S \approx 28\text{-}30$.

A circuit diagram for the engine utilizing this method of neutralization is given in Fig. 2.5. The optional screen grid shown in Fig. 2.3 is used, and the ion grid can be biased as much as 600 volts negative with respect to the anode. The plasma potential can be adjusted by varying the ion grid bias with respect to ground (power supply #4 of Fig. 2.5) or by adjusting the neutralizer filament bias (power supply #6). This mode will be referred to as the high mode since it results in extremely high ion speed ratios or "Mach" numbers.

Since the ion speed ratios generally associated with satellites in the ionosphere are considerably lower than those achieved by the high mode, it is desirable to either lower the beam energy or to raise the electron temperature.

This can be accomplished by using high energy electrons, escaping from the source, for neutralization purposes. Electrons with kinetic energies in excess of the accelerating potential can clearly leave the interior of the source and experience shows that they indeed do if the conditions are appropriate, such as the ones shown on Fig. 2.6. In this mode of operation the ion grid is at the

same potential as the enclosing can, and the optional screen grid is removed. No external neutralizer filament is necessary. This configuration was capable of producing electrons with temperatures up to 4 volts and speed ratios as low as 7, which justifies the designation "low mode," to be used in the rest of this thesis. This mode of operation appears to be first described by Hester and Sonin.[27, 28] The source of Fig. 2.6 differs from theirs only in that one end of the cathode filament was connected to the can, while the other end could be either positive or negative with respect to the can. Since this results in the cathode filament being approximately the same voltage as the ion grid, the net gain of kinetic energy needed by the electrons to escape from the source is much less than the accelerating potential. The resulting electron distribution is quite close to Maxwellian (at least in the axial direction) at temperatures from one to four volts.

The electron temperature can be controlled by varying the internal source parameters such as the cathode current or the magnetic field strength. The chamber plasma potential can be varied by changing the grid or can bias.

In this mode the ion accelerating potential is automatically equal to the anode to cathode potential which can be as low as about 40 volts. Typical power supply settings for both the low and high modes are listed in Table 2.1. For the low mode, these settings generally resulted in a speed ratio of about 10.

Since the low mode more closely approximates conditions in the ionosphere, we generally run the source in this mode. Typically, the beam energy is about 80 eV and the electron temperature about

1.5 volts. At a background pressure of about 10^{-5} torr, the beam density at the model position is then about 10^{8} ions/cm^{3}.

Since the source orifice is 2.5 cm in diameter, and our pump is over 40 cm in diameter, a pressure difference of greater than two orders of magnitude can be maintained between the source and the chamber. This enables the source to operate stably down to 5×10^{-6} torr chamber background pressure. There is also a provision to bleed argon directly into the chamber without going through the source. Using this provision, conditions in the source (including pressure) can be kept almost constant, while the chamber background pressure is varied over almost two orders of magnitude up to 5×10^{-4} torr, allowing the investigation of the effects of high background pressure and charge exchange collisions.

II.2. Chamber and Vacuum System

The source described in the last section is housed completely in a stainless steel vacuum chamber 50 cm in diameter (Figs. 2.1, 2.2). The upstream end wall of the chamber contains all the source power and cooling water feedthroughs. The engine is mounted on this end wall and has no other connections with the chamber; thus it is easily accessible for inspection or alteration.

The chamber itself is divided into a source section and a test section. The source section is mounted on casters and can be easily moved to provide access to the test section. The test section has several ports to accomodate a variety of equipment. Besides the various model, probe and vacuum gauge ports, there are two windows for viewing the test apparatus, and three large ports in the bottom of

the chamber. Two of these are connected to the diffusion pump system, and the other is used for electrical feedthroughs.

The downstream end wall contains the feedthrough for the probe actuator. The driving mechanism for this actuator is mounted outside the chamber and attached to the end wall.

The pump system consists of an Edwards F1605 40 cm oil diffusion pump, a Freon refrigerated baffle, a 40 cm butterfly valve, and an Edwards HlSC1500, 2000 ℓ/min mechanical forepump. The system can nominally handle an argon flow rate of 12, 000 ℓ/sec at an operating pressure of 10^{-5} torr, and produces an ultimate pressure of 10^{-7} torr. The 15 cm pump shown in Fig. 2.1 was installed for the original system and was not generally used with the second generation source. The forepump of this system is utilized, however, in a procedure that allows fast opening and closing of the vacuum system, often needed to carry out minor modifications on the equipment enclosed. In this procedure, the 40 cm butterfly valve is used to isolate the large diffusion pump from the vacuum chamber. The pump can thus be kept hot while the chamber is opened to atmosphere. Using the forepump of the inoperative 15 cm system, the chamber can again be pumped down while the 40 cm diffusion pump is still hot. When the pressure is sufficiently low, the butterfly valve can be opened again. With this procedure, the source can be operated approximately 20 minutes after closing the chamber. The ultimate background pressure with the source argon turned off is usually low enough to take reliable data (10^{-6} torr) within an hour of sealing the system.

Pressures in the chamber are measured with a CVC GIC-110A

ionization gauge below 10^{-3} torr and with a McLeod gauge or a CVC thermocouple gauge above 10^{-3} torr.

The beam proved to be sensitive to the Earth's magnetic field, which was perpendicular to the chamber axis (see Chapter III. 2). To alleviate this problem, two pairs of compensating Helmholtz coils were added outside the chamber. The coils are capable of reducing the field in the test chamber from 0. 3 gauss to 0. 05 gauss, which is sufficient to eliminate the magnetic anomalies.

II. 3. Models

All models used in this investigation were mounted on a shaft approximately 23 cm from the accelerating grid of the source. The shaft was inserted through a port in the top of the vacuum chamber and could be moved up and down or rotated while the chamber was under vacuum. The models were all conducting bodies, and their surface potentials were controllable by using a D.C. power supply.

Most models used are bodies of revolution, which fit naturally into the axially symmetric beam. Since the speed ratios in these experiments are rather high, the shape of the models was thought to be of no great importance: all bodies were expected to sweep out ions from the plasma stream according to the frontal area. This consideration led to choosing discs as the principal shape to be investigated, even though they are clearly not realistic representations of existing satellites. The studies showed that the radial and axial dimensions of the body influence the wake in markedly different ways. These dimensions are very sharply defined for discs, so that in retrospect, the choice of discs proved to be a useful one.

Fig. 2.7 is a schematic of a "thick" disc and of the coordinate system used in discussing the discs. By "thick" disc, we mean one with length, or thickness, L, much greater than the Debye length. Typically the "thick" discs had L = 1.27 cm and a diameter of about 2.5 cm. The "thin" discs were much thinner than a Debye length, usually L = 0.013 cm.

All models were made of brass except where some insulation was necessary; in which case teflon or vacuum epoxy was used as an insulator.

The experiments with the discs indicated the need for other models, two of which were used. To determine the effects of axial symmetry, a "two-dimensional" model was needed for comparison, so the "thin" strip of Fig. 2.8 was constructed. For reasons to be explained later, a spherical model with a thin ring around its circumference tangent to the flow direction was also constructed. This ring could be biased separately from the rest of the model as shown in Fig. 2.9.

Wakes of all the models were studied for a broad range of body potentials. The sphere of Fig. 2.9 was examined with various combinations of different potentials. The results will be described in Chapters IV, V, and VI.

II. 4. Instrumentation

The principal tools of this study were various types of electrostatic probes. The probes were mounted either through a port at a fixed distance behind the model or on the three-degree-of-freedom probe actuator. The actuator was fitted with a phone plug socket so

that probes could be changed easily.

The actuator was designed for a cylindrical coordinate system and could move the probe from about 18 cm from the source axially to 70 cm from the source. The radial travel is approximately 13 cm and the probe can cover an arc of over 300°.

The probe used in the earlier studies was a simple guarded Langmuir probe (Fig. 2.10). For essentially all the wake studies, however, an unguarded spherical probe was used (Fig. 2.11). Various other Langmuir probes and a resonance probe were also utilized. A more detailed description of the Langmuir probes follows. The resonance probe studies were conducted by M. Sajben. A description of his resonance probe work can be found in Appendix 2.

II.4.1. The Langmuir Probe

The Langmuir probe is an extremely useful multipurpose probe. In this investigation, it was used for the measurement of ion flux both in the freestream and wake regions, and for the determination of electron temperature. The probes and associated circuitry are shown in Figs. 2.10 and 2.11. The guarded probe was used in the earlier work, and the unguarded spherical probe was used with the low pressure source. There is considerable literature[39, 40] on the use and construction of Langmuir probes, so we will not go into great detail here.

Since these probes are basically used as flux measuring devices, an important difference between the guarded and spherical probes must be mentioned. By its geometry, the guarded probe measures only one component of the flux at a time; i.e., the front

face measures only $N_i U_Z$. The spherical probe measures the total ion flux at a given point, $N_i |U|$. Thus in the near wake region close behind a model, the guarded probe may give a false impression of the total ion flux. More than a few model radii behind the body, however, the flow is almost axial, and little difference exists between the indications of the two probes.

The Langmuir probes were used in two different modes. To determine the speed ratio, S, one must first find the electron temperature. The probe can be used in one mode to accomplish this, or it can be used in a second mode to measure ion flux or ion density.

The Temperature Mode

In the first or temperature mode, the probe is placed in a fixed position, and the current collected is plotted against probe potential, resulting in the characteristic curve. Fig. 2.12 is a typical probe curve taken with the spherical probe. From this curve one can obtain the probe floating potential, the ion saturation current, the plasma potential, and the electron temperature.

From the probe characteristic, there are two ways to find the electron temperature. Both involve the assumption that the electrons are Maxwellian and that their density at any given point varies as $\exp(e\varphi/KT_e)$. The first method involves replotting the probe characteristic on semilog paper. This is the commonly used method described by Chen.[39] The second method is the tangent method described by Sonin[40] and shown in Fig. 2.12.

For simplicity, temperature will be given in volts (φ) instead of degrees $\frac{e\varphi}{K}$. The ion current, plasma potential, and floating

potential are found in the standard manner.[39, 40]

Ion Flux Mode

The second mode of operation of the Langmuir probe is used when measuring ion flux as a function of position as in wake measurements. In this mode, the probe potential is set to a sufficiently negative value to reject essentially all electrons, but not so low as to interfere with the beam. Typically, for a floating potential of +5 volts, the probe is set at -10 volts. The moseley plotter can plot ion flux versus any position coordinate (R, φ, Z). The position coordinates are fed into the plotter through a potentiometer-power supply system in which the potentiometer resistance is a function of probe position. These plots are found in abundance in later chapters.

In this mode, the current per area collected by the front collector of the probe in Fig. 2.10 is interpreted as the axial ion flux. This should be a good approximation for the highly hyperthermal ions in the free stream. For the spherical probe (Fig. 2.11), the flux is taken as the current divided by the area swept by the sphere. No correction is made for fringing effects of the probe field since these are small.

The ring shaped collector in Fig. 2.10 gives an indication of radial ion fluxes which arise partly because low energy ions are produced by charge exchange collisions and partly because fast ions may have some radial velocity.

The beam ion density can be calculated as the ratio of ion flux to beam ion velocity. The beam ion energy can be obtained from the difference between plasma and ion source anode potentials. The

velocity can then be found from the energy. This method of finding beam ion density may be slightly in error when the probe curves do not saturate, but the effects are not large and the exact values of density are not nearly so important as the relative values from one point to another. Since the ion density measurements are dependent on the ion velocity, the possibility exists that these measurements may be in error in the near wake region. The probe accurately measures flux, but in the wake region velocities may differ from free stream velocity, thus a cross sectional trace of the wake at a constant axial position will give a good picture of the relative fluxes but not necessarily of the densities.

The velocity of ions in the wake region is affected by their interaction with the model. From our experiments, it does not appear to be grossly in error to assume that this interaction results mainly in changes in direction. Since the flux variations are very large in the near wake and the speed variations small, the density trends can be found with reasonable accuracy by assuming a constant speed equal to the free stream speed throughout the wake.

In general the Langmuir probe is a useful instrument to establish trends. It can give an accurate representation of the relative magnitudes as a function of position of the quantities it is used to measure. Flux and density ratios are probably accurate to a few percent, while absolute magnitudes are more uncertain. Ion flux measurements are probably not accurate to more than ± 20%, and electron temperatures may be off by 50%. Electron temperature ratios, however, are probably accurate to ±15%.

III. THE PLASMA BEAM

III. 1. Properties of the Beam

The ion source is capable of generating an ion beam with energies from 50 to 100 eV in the low mode, and from 80 to 500 eV in the high mode. In the low mode, at the model position and at 10^{-5} torr, the beam density is about 10^{8} ions/cm^{3}, independently of energy in the low mode. In the high mode, it is less by about 50%, due to the blocking effect of the extra grid. For pressures lower than 10^{-5} torr, the low energy ion density is estimated to be lower than 5% of the total ion population. For higher pressures the slow ion density increases rapidly. A discussion of the effects of high background pressure, collisions, and slow ions on the beam is presented in Appendix 3.

In the low mode, electron temperatures can be varied from 1 to 5 volts, 1.5 volts being average. With a typical beam energy of 75 eV, an ion speed ratio of about 10 is normal. In the high mode, the electron temperature is approximately .2 volts; and the beam energy is usually set at 100 eV, resulting in a speed ratio of nearly 30. The electron temperature and plasma potential decrease slightly toward the downstream end and the walls of the chamber. The plasma potential is usually about 5 to 10 volts above ground at model position.

The source makes use of a confining magnetic field to constrain electrons. This fringing portion of this field decreases to the level of the Earth's field within a few centimeters of the grid. The Earth's field has a strength of about 1/3 gauss perpendicular to the beam direction, but with the compensating coils mentioned in Chapter II, the fields in the test section of the chamber can be reduced to less

than 0.05 gauss.

The beams have been found to approximate a flow from a point source. The ion flux decreases as $1/(Z-Z_0)^2$ from an effective origin, Z_0, upstream of the model (Z_0 is negative). Thus a plot of $1/\sqrt{J}$ as a function of Z along the chamber axis is approximately a straight line, where J is the probe current in the ion flux mode. This straight line can be extrapolated to zero to give the effective origin. Fig. 3.1 shows several of these plots for various values of beam energy in the low mode. It appears that the effective origins are close to the orifice but vary slightly with beam conditions. Typical beam profiles are shown in Fig. 3.2 for several values of Z. This figure is for a beam energy of 54 volts but is typical for all beam energies in the low mode.

The source flow nature of the beam can also be shown in another way. For a truly source-flow-like beam the current should decrease as $1/z^2$ along straight lines from the effective origin, where z is the distance from the origin. Fig. 3.1 showed that this was true for a particular line. Fig. 3.3 is a replot of the first four profiles of Fig. 3.2. On Fig. 3.3, J is normalized by multiplying by $\frac{r^2 + (Z-Z_0)^2}{Z_0^2}$. r is replaced by the angle measured from the axis; thus the normalized J is plotted against $\tan^{-1}\left(\frac{r}{Z-Z_0}\right)$. For a source-flow beam all the curves in Fig. 3.2 should collapse into one curve in Fig. 3.3. Using an effective origin of 8" the curves are seen to collapse quite well, indicating that the beam can indeed be characterized as a source flow. The deviation in the Z = 10 curve is due to the

sensitivity of the transformation to small variations in J at large Z values.

III.2. Effect of the Earth's Magnetic Field

In the early studies using this beam, the electron temperature was found to vary by as much as a factor of two as a function of angular position, while the electron density was reasonably independent of the azimuthal angle. This effect was eventually traced to the Earth's magnetic field and was reduced by the addition of compensating Helmholtz coils around the outside of the chamber. It is believed that the effect is due to the fact that the magnetic field deflects the low temperature electrons more than the high temperature ones as they escape from the source. This effect could have been missed completely if electron temperatures had been measured on only one chamber diagonal; i.e. if the probe had only been moved horizontally across the beam. It is possible that this effect may be present in other experiments of this type.

The temperature variation with the compensating coils turned off was generally confined to a wedge shaped region of about 100 degrees. The temperature would be nearly uniform outside of this region and within it would increase to as much as twice the outside temperature. The position of this wedge was rotated by about 60 degrees by reversing the polarity of the confining magnetic field of the source.

Fig. 3.4 is a plot of electron temperature as a function of azimuthal angle at about 25 cm from the source. The temperatures were taken at a radius of 5 cm with the compensating coils on and off.

In this case the beam energy was about 70 eV, and the conditions were typical of those used for taking data. In some cases, the variation of T_e was larger than that shown in Fig. 3.4, but the location of the high temperature region was generally between 350° and 90° if the confining magnetic field was not anti-parallel on the beam. A smaller temperature variation was also noted at 210°.

III.3. Repeatability

In this investigation, the power supply voltages and chamber pressures could be reproduced within a few percent. The resulting beams, however, were dependent on several other hard to control factors, mostly on the state of the surfaces of the various filaments. Beam properties such as electron temperature and ion flux would change by as much as 50% as the source heated up. After these initial transients, however, the beam properties could be kept constant within 5% for several hours.

As the cathode or neutralizer filaments gradually evaporated, small corrections had to be made to keep the electron emission constant. The time scale for making these corrections was much longer than that for taking data, so there was no problem in keeping the beam steady for any given set of conditions.

From day to day, beam conditions could be reproduced within about 10% if no modifications were made on the source. If, however, any filaments had been changed or the source had been cleaned of tungsten deposits, beam conditions could be expected to vary by as much as 20% from previous runs at the same power supply settings. However, by readjusting the settings and monitoring the beam with

the Langmuir probe, good repeatability could be obtained.

Wake repeatability is dependent not only on the beam but also on the model. The gross features of the wake are easily repeatable, but the structure in the region immediately behind the model is highly dependent on the model-probe alignment. Fig. 3.5 shows two sets of traces of the near wake of the same disc taken under approximately the same conditions. One set of traces was among the first obtained and the other was among the last. In between, the filaments were changed several times, and a few minor modifications were made. The beam structure and the gross wake features are seen to be quite similar, but in the $Z/a = 2$ traces, the peak at $r/a = 0$ is seen to be much higher in one case than in the other. This is due to the fact that the probe was not perfectly aligned with the model in the low peak case: a very small excentricity is sufficient to produce the variation shown.

Fig. 3.6 is a continuation of Fig. 3.5 for the far wake. Again, the gross features of the wake are repeatable, but the fine structure is better defined in one case than in the other. This difference may be due to a slight change in beam alignment with the chamber axis. The probe always moves on a line through the chamber axis while the beam and thus the wake in the far wake region may be slightly off center. The far wake fluxes were repeatable within 10% from day to day, provided the source was not modified.

One should remember that although the wake structure is repeatable and the ratios of measured quantities can be found within a few percent, the absolute values of the measured quantities may be

as much as 50% off. For the purposes of this thesis, however, such accuracy is acceptable since we are mainly interested in the ratios.

IV. INVESTIGATION OF THE NEAR WAKE

This chapter presents the results of our study of the near wake region for various conducting models. The investigation was limited to models which are negative with respect to the plasma. The wakes were studied both for models which were slightly negative and for models highly negative with respect to the plasma potential. The parameter $\alpha = -\varphi_M/\varphi_B$ gives one an idea of the extent to which a model is negatively biased. φ_M is the potential of the model with respect to the plasma potential, φ_P. φ_B is a measure of the kinetic energy of the beam and is the potential drop through which the beam ions were accelerated, i. e. the difference between the anode and the plasma potentials. Typically $\alpha = 0.05$ is considered small since an unbiased satellite will float at an α of this order. When a model is biased such that the potential drop through the sheath is of the order of the beam ion energy, the model can be expected to exert a large influence on the nearby ions, and thus $\alpha = 0[1]$ is considered large.

The models used are symmetric about a flow axis or about a plane parallel to the flow. They were spheres, discs and strips aligned perpendicular to the flow (see Chapter II-3). The discussion which follows assumes such symmetry. Any radial dimensions or coordinates mentioned are perpendicular to the flow direction and, in the case of the strip, are perpendicular to the long axis. The radial dimensions of all bodies were much larger than the Debye length; the thicknesses in the flow direction, however, varied from much smaller to much larger than the Debye length. The problem of small body size

to Debye length ratio is of interest for satellite antennas, but as far as the overall satellite wake is concerned, the main contribution comes from the large body and not its small appendages.

The experimental results presented in this chapter were obtained at a background pressure sufficiently low that charge exchange collisions and low energy ions were not a problem. Some results for higher pressures will be presented in Chapter VI. The results presented here are for cold ions ($T_i/T_e \ll 1$) and negligible magnetic field.

IV. 1. Description of the Near Wake

Fig. 4. 1 shows a cutaway view of a typical wake. The body is a thin conducting disc of diameter large compared to the Debye length, which is aligned perpendicular to the stream at $Z/a = 0$ (Fig. 2. 7). The model potential is slightly negative relative to the beam. The curves plot ion flux versus radius at various distances behind the model.

It is easy to see that the wake can be divided into the characteristic regions described in Chapter I. Immediately behind the body is a swept region from which the ions are almost completely excluded. Farther downstream along the centerline is a flux peak which is actually greater than the free stream flux. This peak gradually decays, giving rise to wavelike disturbances in the process, which spread out radially farther downstream. We define the part of the wake upstream of and including the peak as the "near" wake and the region downstream of the peak as the "far" wake. The reason for this division becomes clearer when one examines closer the

characteristics of the near and far wakes.

The early data suggested that the near wake structure was basically determined by the interaction of the ion stream with the sheath near those parts of the model where the stream velocity is tangent to the surface (Fig. 1.1). Judging from the inward movement of the "walls" of the shadow region, the innermost ion trajectories between the sheath and the observed peak on the axis appeared to be relatively straight.

Based on these early observations, a simple theoretical model was constructed concerning the structure of the near wake of a negatively charged body. In order to have a guideline for the presentation of the experimental results, this model will be described next. The experimental results will then be examined in light of this model.

For bodies of diameter or width large compared to the Debye length, the sheath spreads out only a small fraction of the body width from the body (Fig. 1.1). The ions arriving at the body at a large radius are deflected toward the axis very slightly. Those ions which pass through the sheath are deflected more strongly. The ions which just miss the model will continue toward the axis behind the body, accelerated inward still more by the potential gradient between the beam and the void behind the body. These first ions to reach the axis form the flux peak which is the predominant feature of the near wake. For axisymmetric bodies, there is a focusing effect, and the peak can be quite large.

Due to the very high ion Mach number, beam ions do not enter the shadow region. It is populated by electrons only, hence there is a net negative space charge and a potential gradient which will tend to deflect ions farther inward. In the case of highly negative bodies, the extent to which the electric field in the void contributed to the total ion deflection does not appear large. A theoretical estimate of the magnitude of this electric field, supporting this claim, is given in Appendix 4.

If this picture is correct, the parameters which determine the size, shape, and position of the flux peak are those which define the size of the body and those which determine the strength of the body-beam interaction. If the body is highly negative, the ions deflected by the sheath will acquire an inward directed kinetic energy comparable to the beam energy and the peak will be close to the body. If the body is less negative, the peak will be farther downstream. Thus, the ratio of body potential to beam energy, α, is an important parameter. Since the deflection of ions continues as long as the ions travel within the sheath, the streamwise length or thickness (L) of the edge will be important. A longer body will tend to deflect an ion more than a shorter one since the ion will be subject to the body's field longer. For the larger a/h values of this study, an individual ion will not notice the transverse curvature of the models; thus, all other parameters being the same, an individual ion would be deflected through the same angle by either a disc or a strip of the same thickness. The peak for a wide body will be downstream of that for a less wide body, though the deflection angle should be about the same if

the other parameters are. The electron temperature and thus the beam speed ratio, S, should be relatively unimportant in the near wake, at least for the large S values of these experiments ($S \sim 10$).

These assumptions are based on the conditions that the edges of the bodies are parallel to the stream direction and that the bodies are negative with respect to the plasma. If the model is held at plasma potential, a small peak may still form because energetic electrons will scatter into the swept region behind the body and generate a potential gradient which diverts the ion beam. This peak will be much weaker and farther downstream than in the case of a negative body. For other bodies such as spheres which have no definite edge parallel to the stream, some effective edge length can probably be defined since those portions of the sphere that are tangent to the beam are assumed to have the greatest effect on the wake.

It is possible to bias one part of a satellite with respect to another, and a satellite with a negatively biased ring tangent to the ion stream is feasible. This negative ring enables a satellite which is ordinarily at a moderate floating potential to behave as if it were highly negative. An arrangement of this sort could be used to actively manipulate the wake of a given satellite, if this is desired (Appendix 5). An examination of the cold ion wakes of highly negative bodies is thus not a purely academic question.

IV. 2. The Effects of Body Potential on the Near Wake

In this section the variation of the near wake of a thin disc as a function of body potential will be considered. Figs. 4. 2 and 4. 3 depict the wake of a slightly negative thin disc. As with all wakes

discussed in this chapter, the far wake figures are presented together with those of the corresponding near wake. However, discussion of the far wake portion will be postponed until Chapter V. A comprehensive list of the parameters of the various wakes, electron temperature, speed ratio, etc., can be found in Table 4.1.

There are several features which characterize the near wake of a thin disc (Fig. 4.2). Immediately behind the disc, the flux drops to zero. The sharp drop of ion flux at r/a = 1 on the top curve (Z/a=0) is not perfectly vertical only because the probe radius is finite ($r_p/a \sim 1/10$). Progressing downstream, the "walls" of this flux well move inward, acquiring a less steep slope in the process. Before the deflected ions reach the axis, a very small flux peak is noticeable on the centerline. This "peak" in the Z/a=2 curve may be due to the very small amount of low energy ions still present in the beam. At Z/a=6, the first deflected ions have reached the centerline. Because of the focusing effect of the axial symmetry, the peak is significantly greater than the free stream flux at the same axial position. More will be said about the significance of the peak structure when we discuss the far wake.

Increasing the magnitude of the disc charge has a dramatic effect on the near wake. Fig. 4.4 presents traces of ion flux versus distance along the axis behind the model for various values of the body potential to beam energy ratio, α. The flux labeled by F. S. on the ordinate indicates the free stream flux at the model position. As the negative bias of the disc is increased, the peak moves forward, and the focusing is greatly increased. The flux peak for the $\alpha = .66$

case is about 4 times the free stream flux at the model position. Ions which originally passed through the body sheath farther away from the body continue to reach the centerline for several model radii downstream.

Figs. 4.5 and 4.6 depict the radial traverses for the $\alpha = .66$ case. The first trace (immediately behind the model) in Fig. 4.5 indicates the large effect that a high value at α has on the wake. This trace shows a very noticeable effect outside of the shadow region, ($r<a$), which was not present in Fig. 4.2. This indicates that the model exerts some upstream influence; i.e., the sheath is fairly thick, and some ions are deflected before they reach the disc. Presumably, the ions that are missing outside the shadow region at $Z/a = 0$ have already been deflected into the disc.

The strong deflection focuses the ions on the axis within two radii of the disc. The $Z/a = 2$ case in Fig. 4.5 shows that this focusing can be extremely sharp. The width of the peak is approximately the same as the probe diameter, indicating a sharpness in excess of the resolution in the diagnostics. The measured flux is approximately 7 times the free stream flux at $Z/a = 2$, while the actual peak must be even more. A slight change in the alignment of the disc with respect to the probe will reduce the peak flux by a factor of 2 or 3. This sensitivity suggests a very precise method of aligning a satellite with its flight path utilizing a small disc in front of the satellite.

Most of the effects of body potential on the wake shown by the disc are present in wakes of other bodies as well. The extreme

magnitude of the peak for large values of α is a result of the axial symmetry and should not be expected for irregular bodies.

IV. 3. Effect of the Body Shape and Size

The main body features which determine wake shape are the degree of symmetry of the body, the width (a/h) and the streamwise length (L/h). If the model is not symmetric about a flow axis, the ions will not be focused on the centerline, and the peak structure will not be so well defined.

The case of a thin strip, aligned perpendicular to the axis is a good case in point (Fig. 2.8). The strip is symmetric about a vertical axis. Thus, the ions should be focused on a plane behind the strip, not on a line. This focusing, in effect, is really just an addition of two beams and not of an infinite number as in the case of the disc. If the assumption that the deflection of an ion is determined mostly by the interaction with the body sheath is correct (at least for highly negative bodies), then strips and discs of the same width and thickness should generate peaks the same distance downstream under the same conditions. However, the strip peak should be much weaker than that of the disc.

Fig. 4.7 clearly demonstrates these effects. Flux is plotted along the centerline behind the models. The peaks for the disc are 8 to 10 times larger than the strip peaks, yet the positions are the same for both the highly negative and the slightly negative cases. The fact that the slightly negative peaks coincide indicates that the effects of the shadow region as well as the edge effects are similar for the two models.

Figs. 4.8 and 4.9 are transverse (x/a) plots of the ion flux behind the above strip for various distances downstream. (See Fig. 2.8 for definition of axes.) The strip was highly negative, and the beam conditions were similar to those of Figs. 4.5 and 4.6. The absence of axial symmetry in this wake is evident from the relationship of the peak to the rest of the wake. In Figs. 4.5 and 4.6, the peak is the predominant feature near the body serving as an initial condition for the far wake. In Fig. 4.8, the wake upstream of the peak is similar to the disc case, but the peak itself is weak and small compared to the deficit in which it is centered. This tiny peak is soon "swallowed" by the deficit, and the predominant initial condition for the far wake is a "hole" or ion deficit rather than a flux peak.

It should be noted here that Hester and Sonin[27] have found the peak to be dominant for small cylinders ($a/h \ll 1$), which are also two-dimensional and somewhat comparable to strips. Thus, at least for the two-dimensional cases of rods or strips transverse to the beam, there is a width above which the defect, rather than the peak, is the dominant initial condition for the far wake. This type of critical width may also exist for axial symmetric bodies. The models tested in the new beam ranged from 20 to 40 Debye lengths in diameter, and the peaks dominated. Hester has also presented some data for very wide spheres ($a/h = 40$) where the peak remained predominant.[28] However, it is possible that no one has yet tested a body sufficiently large to exceed the critical a/h so the question is still open.

The relationship of the peak to the far wake structure will be discussed in somewhat more detail in Chapter V.

The effects of changing disc diameter are rather straightforward. Some of the data from the first generation beam (not presented here) indicated that the peak position moved back linearly with an increase in model radius.

The effect of changing model thickness is also as expected. Once a model is thinner than a Debye length, making it even thinner makes no difference. The sheath determines the wake structure and is no different for a model 1/10 or 1/100 of a Debye length. Making a thick model ($L/h > 1$) thicker does change the sheath. Figs. 4.10, 4.11, and 4.12 indicate the effect on the wake of a thick model. The model is a disc 2.5 cm in diameter by 1.27 cm thick. L/h is about 13 at model position. Axial distances are measured from the downstream side of the model (Fig. 2.7). As demonstrated by Fig. 4.10, an ion will remain in the sheath region longer for a long model; thus it will be deflected inward more, and the peak will be upstream of that for a thinner model. Figs. 4.11 and 4.12 show radial traces for the highly negative thick disc. Except for the peak position, the features are identical to those of the thin disc.

The wakes of some other models not discussed here are shown in Appendix 5.

IV.4. Effect of Electron Temperature

It was mentioned earlier that the peak position should not be dependent on electron temperature. This expectation is borne out by Fig. 4.7 which shows the wakes of a strip and a disc in beams of nearly identical energies, but at electron temperatures differing by a factor of approximately two. The peak positions are seen to be the

same. It is probably generally true that the electron temperature does not affect the near wake structure, as long as $T_e/T_i \gg 1$ and α is not very small. If the body is floating (α small) then the electric field of the shadow region is not negligible, and some temperature effects may exist.

IV. 5. A Crude Theory to Predict Peak Position

Assuming that the electric fields in the sheath near the edge of a model cause much larger ion momentum changes than the fields either ahead of or behind the body, we have developed a very crude theory which predicts the approximate position of the ion flux peaks behind large discs or strips.

Fig. 4.13 illustrates the simplified conditions on which the theory is based. The sheath is assumed to be thin compared to both the radius and the thickness (L) so that most of the radial acceleration of the ions takes place in a thin layer within a few Debye lengths of the body. Ions arriving farther away are not greatly influenced by the body, and those approaching too close are absorbed on the surface. Ignoring the existence of axial fields near the corners, a purely radial electric field is postulated for $-L < Z < 0$. The exponential decay for the sheath is chosen purely for convenience. The ions are assumed to maintain a constant axial velocity throughout the interaction with the model. Having postulated the electric fields, the ion trajectories can be easily calculated, including the one which just clears the disc or strip and intercepts the axis at $Z = Z_p$. Since the fast ion flux is zero along the axis up to this point, Z_p is identified as the location of the ion current peak. The details of the calculation

are presented in Appendix VII. The resulting equation for the peak position is as follows:

$$Z_p/a = L/h \left[Y_p \mathrm{Tan}(Y_p/2)\right]^{-1}. \tag{4.1}$$

where Y_p is given implicitly by:

$$Y_p = (L/h)\sqrt{\alpha}\ \mathrm{Cos}(Y_p/2) \tag{4.2}$$

The general trends given by Eq. (4.1) are shown in Fig. 4.14. The experimental curves are compared with data obtained from both the first and second generation beams using discs of several sizes at several values of α. The theoretical results, crude as the theory is, are in rough agreement with the data for thick bodies. Agreement cannot be expected for thin bodies since the axial extent of strong electric fields is roughly L + 2h and not L as assumed here. It follows from the model, however, that in the limit of small L/h, the dependence of Z_p/a on L/h should be weak, as indeed is shown by the data. The theory could probably be stretched to include thin bodies by defining an effective thickness, but it is hardly worth the effort. It should be noted that the theory overestimates Z_p for small values of α. A probable reason for this behavior is that in this case the ion deflection due to gradients in the void region is comparable to the deflection caused by the sheath region (Appendix 4). The resultant Z_p is less than the prediction, which neglects the effects of the void region.

The importance of this theory lies not in its accuracy, but in its ability to predict nearly all trends shown by the data, and thereby

strongly supporting the validity of the physical model on which it is based.

V. THE FAR WAKE

The experiments provided ample evidence that the electrostatic potential is very nearly constant downstream of the peak, i. e. in the far wake region. Since the flow is collisionfree, simple energy considerations dictate that the absolute value of the velocity of any ion be approximately constant. The ion temperature is very close to zero, so that the same applies to the mean velocity of the ions. The result is that the deviation of the ion mean velocity from a uniform freestream value is primarily in the direction perpendicular to the freestream velocity. If the perpendicular variation is $O(\epsilon)$, then the streamwise variation is $O(\epsilon^2)$.

The same situation exists in hypersonic continuum flows, where it has been shown (34) that this ordering of the perturbation velocities leads to an analogy between steady two-dimensional and unsteady, one-dimensional flow. An observer moving with the freestream velocity will see an unsteady flow that is principally a function of the transverse coordinate, streamwise variations being negligible. Axial distance from the body corresponds to time and the growth of the wake is replaced by a temporal evolution of some initial density and velocity distribution. These initial conditions in our case are generated by the near wake mechanisms, to which this analogy does not apply. The initial conditions, therefore, must be looked upon as specified in the statement of the time dependent problem. In the present study, they have been chosen to simulate the radial distributions of density and velocity, as measured shortly downstream of the peak region.

The description adopted here is a two-fluid model, describing the ions and electrons separately. It is clear that all details concerning velocity distributions are lost. In particular the two-humped structure of the ion distribution function in the peak region is not reflected in any way, even though such a distribution must exist owing to the inter-penetration of two distinct ion streams at that location.

As it turns out, the two fluid model gives a qualitatively correct description of the far wake features. This may be construed to indicate that the ions are somehow relaxing to a single-humped velocity distribution. The details of such a process were not investigated. The subject clearly deserves further study, since it constitutes the perhaps least understood feature of the entire wake pattern: the transition from a near wake flow, characterized by individual ion trajectories, to a far wake which can be apparently well described by a fluid model.

As will be shown in Sect. V. 1, the governing equations that result from the fluid model imply that the far wake is wavelike in nature. This means that most of the factors which affect the near wake will affect the far wake only through the initial conditions that they present. The body parameters, for example, determine the shape of the initial conditions and have no further effect on the flow field downstream. The experimental examination of the far wake will therefore be confined to the effects of various initial conditions and of collective parameters which affect the wave properties such as electron temperature, ion temperature, and ion density.

The theoretical studies will concentrate similarly on the effects of various initial conditions. The ion density and electron temperature are normalized out of the problem through the Debye length and the ion plasma frequency. We have not studied the effects of ion temperature directly, but the effects can be inferred from the results of other authors who dealt with similar problems.

Since the theory gives some insight into the results of the experiments, we will first develop the theory for both the one-dimensional (time dependent) case of the strip and the cylindrical case of the disc wakes. The development of the wake for initial conditions similar to those of the experiments will be examined. The experimental results will then be presented in light of the theory.

For the near wake, distances were scaled with the body size. For the far wake, one would expect that the representative scaling factor is the Debye length or some width characteristic of the initial condition, such as the width of the ion flux peak. In the theory, we will indeed scale with the Debye length, but the original scaling (model size) will be retained for convenience when discussing the experiments.

V. 1. A Theory for the Far Wake

V. 1. 1. Development of the Theory

In this section we are going to develop a linearized theory for the time dependent development of an initial disturbance in a plasma. The plasma consists of cold ions ($T_i = 0$) and hot electrons. The electrons will be assumed to possess a Maxwellian velocity distribution and negligible mass. The theory will be developed for both the

one-dimensional and axial symmetric cases along the lines suggested by L. Lees[33] and used by Jack Hill.[32] Since the one-dimensional case is slightly more simple, it will be examined first. The development of the cylindrical case is similar and will follow with less detail. We will start with the following equations which are consistent with the above assumptions:

Continuity: $$\frac{\partial N_i}{\partial t} + \frac{\partial}{\partial x}(N_i V) = 0 \quad , \tag{5.1}$$

Momentum: $$N_i \frac{\partial V}{\partial t} + N_i V \frac{\partial V}{\partial x} = \frac{N_i e}{M_i} E \quad , \tag{5.2}$$

Poisson: $$\frac{\partial E}{\partial x} = \frac{e}{\epsilon_0}(N_i - n) \tag{5.3}$$

Maxwellian electrons $$n = N_{i0} \exp\left(\frac{e\varphi}{KT_e}\right) \quad , \tag{5.4}$$

$$E = -\frac{\partial \varphi}{\partial x} \quad . \tag{5.5}$$

N_i is the ion density, n is the electron density, and V is the ion velocity in the x direction normal to the axis. The remaining variables are defined on page xiii. The definitions are consistent with those used for the experimental studies.

Assuming small perturbations, and a uniform unperturbed potential, φ_0, of zero, the variables can be written as:

$$N_i = N_{i0} + N' \qquad n = N_{i0} + n' \qquad V = v$$

$$= N_{i0} + N_{i0}\left(\frac{e\varphi}{KT_e}\right)$$

If we substitute these variables into the above equations, utilize appropriate derivatives of Eqs. 5.4 and 5.5, and drop the products

of perturbed quantities, we are left with:

$$\frac{\partial N'}{\partial t} + N_{i0} \frac{\partial v}{\partial x} = 0 \quad , \tag{5.6}$$

$$N_{i0} \frac{\partial v}{\partial t} = - \frac{KT_e}{M_i} \frac{\partial n'}{\partial x} \quad , \tag{5.7}$$

and

$$(N'-n') = - \frac{\epsilon_0}{N_{i0}} \frac{KT_e}{e^2} \frac{\partial^2 n'}{\partial x^2} \quad . \tag{5.8}$$

Eliminating v between Eq. 5.6 and Eq. 5.7 gives

$$\frac{\partial^2 N'}{\partial t^2} - \frac{KT_e}{M_i} \frac{\partial^2 n'}{\partial x^2} = 0 \quad . \tag{5.9}$$

We can now see that the natural scaling factors for the far wake are the Debye length, h, and the ion plasma frequency, ω_{pi}. If we define: $\xi = x/h$, where $h = \sqrt{\frac{KT_e \epsilon_0}{N_{i0} e^2}}$

and $\tau = \omega_{pi} t$, where $\omega_{pi} = \sqrt{\frac{N_{i0} e^2}{M_i \epsilon_0}}$

Eqs. 5.8 and 5.9 then become

$$(N'-n') = - \frac{\partial^2 n'}{\partial \xi^2} \quad , \tag{5.10}$$

and

$$\frac{\partial^2 N'}{\partial \tau^2} = \frac{\partial^2 n'}{\partial \xi^2} \quad . \tag{5.11}$$

Substituting Eq. 5.11 into Eq. 5.10, operating on the result with $\frac{\partial^2}{\partial \xi^2}$, and substituting Eq. 5.11 again, one finds

$$\frac{\partial^2 N'}{\partial \tau^2} - \frac{\partial^2 N'}{\partial \xi^2} - \frac{\partial^4 N'}{\partial \xi^2 \partial \tau^2} = 0 \quad . \tag{5.12}$$

For convenience, define $N = \frac{N'}{N_{i0}}$, and obtain the equation for small disturbances in a plasma of this sort as:

$$\frac{\partial^2 N}{\partial \tau^2} - \frac{\partial^2 N}{\partial \xi^2} - \frac{\partial^4 N}{\partial \tau^2 \partial \xi^2} = 0 \qquad (5.13)$$

Eq. 5.13 can be solved by using Fourier transforms. The transformed density is given by:

$$\bar{N}(k, \tau) = \frac{1}{\sqrt{2\pi}} \int_{-\infty}^{\infty} e^{-ik\xi} N(\xi, \tau)\, d\xi \quad . \qquad (5.14)$$

If this transform is applied to Eq. 5.13, it gives

$$\frac{\partial^2 \bar{N}}{\partial \tau^2} + \frac{k^2}{1+k^2} \bar{N} = 0 \quad . \qquad (5.15)$$

The solution of Eq. 5.15 is

$$\bar{N}(k, \tau) = \bar{N}(k, 0)\, \mathrm{Cos}(\omega\tau) + \frac{1}{\omega} \frac{\partial \bar{N}(k, 0)}{\partial \tau} \mathrm{Sin}(\omega\tau) \quad , \qquad (5.16)$$

where $\omega = \sqrt{\frac{k^2}{1+k^2}}$.

Using Eq. 5.6 and the definition of the transform; the density derivative in Eq. 5.16 can be written as a function of the initial velocity distribution:

$$\frac{1}{\omega} \frac{\partial \bar{N}(k, 0)}{\partial \tau} = -\frac{1}{\omega} \frac{1}{\sqrt{2\pi}} \int_{-\infty}^{\infty} e^{-ik\xi} \frac{1}{c} \frac{\partial v(\xi, 0)}{\partial \xi} d\xi \qquad (5.17)$$

where $c = \sqrt{\frac{K T_e}{M_i}}$. Inverting the transform, the solution for the perturbation density is:

$$N(\xi, \tau) = \frac{1}{\sqrt{2\pi}} \int_{-\infty}^{\infty} \bar{N}(k, 0) \mathrm{Cos}(\omega\tau) e^{ik\xi} dk + \frac{1}{\sqrt{2\pi}} \int_{-\infty}^{\infty} \frac{1}{\omega} \frac{\partial \bar{N}(k, 0)}{\partial \tau} \mathrm{Sin}(\omega\tau) e^{ik\xi} dk \qquad (5.18)$$

Thus the solution can be found for any initial density and velocity distribution. If the initial conditions possess a simple enough transform, then Eq. 5.18 can be integrated relatively easily on the computer. The details for several types of initial conditions for both the one-dimensional and cylindrical cases are carried out in Appendix 7. We have concentrated on initial conditions which simulate those seen experimentally, but several others are also examined. We will look at some of the results after deriving the cylindrical equations.

Writing Eqs. 5.1 through 5.5 in cylindrical coordinates as a function of r and t only and then following almost the same procedures as before, we end up with:

$$\boxed{\frac{\partial^2}{\partial \tau^2}\left[\frac{1}{\rho}\frac{\partial}{\partial \rho}\left(\rho \frac{\partial N}{\partial \rho}\right)\right] + \frac{1}{\rho}\frac{\partial}{\partial \rho}\left[\rho \frac{\partial N}{\partial \rho}\right] - \frac{\partial^2 N}{\partial \tau^2} = 0} \quad , \qquad (5.19)$$

where $\rho = r/h$, and other quantities are defined as before. Here, r is equivalent to x in the one-dimensional equations. In this case, the solution is found using Bessel J_0 transforms defined by:

$$\overline{N}(k, \tau) = \int_0^\infty N(\rho, \tau) J_0(k\rho)\, \rho\, d\rho \quad . \qquad (5.20)$$

Transforming Eq. 5.19, the result is an equation identical to Eq. 5.15 with the solution given as:

$$\overline{N}(k, \tau) = \overline{N}(k, 0)\mathrm{Cos}(\omega\tau) + \frac{\partial \overline{N}(k, 0)}{\partial \tau}\,\frac{1}{\omega}\,\mathrm{Sin}(\omega\tau) \quad . \qquad (5.21)$$

Inverting the transform gives:

$$N(\rho, \tau) = \int_0^\infty \bar{N}(k, 0) J_0(k\rho) k \operatorname{Cos}(\omega\tau) dk + \int_0^\infty \frac{1}{\omega} \frac{\partial \bar{N}(k, 0)}{\partial \tau} \operatorname{Sin}(\omega\tau) k J_0(k\rho) dk \quad \text{where } \omega^2 = \frac{k}{1+k^2} . \tag{5.22}$$

The initial velocity distribution enters through the continuity equation as before:

$$\frac{\partial N}{\partial \tau} = - \frac{(v/c)}{\rho} - \frac{\partial (v/c)}{\partial \rho}$$

to give:

$$\frac{\partial \bar{N}(k, 0)}{\partial \tau} = \int_0^\infty \frac{v(\rho, 0)}{c} J_0(k\rho) d\rho + \int_0^\infty \frac{1}{c} \frac{\partial v(\rho, 0)}{\partial \rho} J_0(k\rho) \rho d\rho \tag{5.23}$$

V. 1. 2. Application of the Theory

Given any small initial density or velocity distribution, the behavior of this type of plasma as a function of time can now be predicted. In practice, however, the solutions for initial density disturbances are easier to obtain than those for initial velocity disturbances. In both Eq. 5. 18 and Eq. 5. 22, the first integral is dependent upon the initial density distribution only. The second integral in both equations is dependent on $\frac{\partial \bar{N}(k, 0)}{\partial \tau}$. From the continuity equation, one can show that $\frac{\partial \bar{N}(k, 0)}{\partial \tau}$ can be written in terms of the initial velocity distribution. Thus the first integral of both equations is dependent only on the initial density and the second integral only on the initial velocity distribution. Since the two integrals are independent and additive, the behavior of density perturbations and velocity disturbances may be studied independently.

For the 1-D case, there is some justification for ignoring the initial velocity distribution and concentrating only on the density disturbance generated by the ion deficit. The experiments have shown that the peak region has little effect on the far wake. From Figs. 4.8 and 4.9, it appears that the two streams which form the peak merely cross without much interaction and then continue outwards, eventually to be overshadowed by the mainstream at the edge of the shadow region. Farther downstream, the x velocities are due essentially to the beam spreading and probably have no effect on the details other than widening the deficit slightly.

In the disc case, radially inward velocities must have some effect because of the extremely high ion densities along the axis that they create. The experimental results (Section V.2) indicate that the inward directed ions interact with one another and probably remain in the vicinity of the axis. If this were not the case, the use of average velocities in this theory would not be valid because the problem would be one of an infinite number of interpenetrating streams. At present, the mechanism by which the inward directed streams interact is not understood.

In this chapter, we will present results for the development of initial density disturbances which simulate those seen in the experiments. The effects of an inward directed initial velocity disturbance will also be examined for the one-dimensional case and the results extrapolated to the cylindrical case.

V. 1. 3. The One-Dimensional (Strip) Case

Let us look at an initial ion deficit, described by the following cosine distribution:

$$\frac{N'(\xi, 0)}{N_{i0}} = -A \cos \frac{\pi}{2} \frac{\xi}{b} \qquad 0 \le |\xi| \le b$$
$$= 0 \qquad b < |\xi| \tag{5.24}$$

where b is given in Debye lengths, and A is taken to be 1 for convenience. Actually, the theory is only valid for $A << 1$; but the solution is linear, and changing A will merely change the solution by the same factor. Fig. 5. 1 shows the solution as a function of the normalized time, τ, for several values of τ. Since the solution is symmetric about $\xi = 0$, only the $\xi > 0$ half is shown. The curves represent only the perturbation densities about N_{i0}, accounting for the negative densities shown in the figures. It should be noted that since the equations are linear, the solutions given here for various initial conditions can be added or subtracted to give new solutions. The negative of the above deficit solution is the solution for a wide density peak.

Fig. 5. 1 shows the evolution of a disturbance that is large compared to the Debye length (b = 20). One can see that the theory predicts no fine structure. The deficit merely splits, and two solitary waves, each about the same length as the original deficit, propagate out at the wave speed.

Though the disturbances of width on the order of a few Debye lengths were unimportant in the experimental strip wakes, it is interesting to consider the predictions of the theory for narrow initial density distributions. Figs. 5. 2 and 5. 3 show the development of

disturbances described again by the cosine function of Eq. 5.24, taking b 3 and 1 respectively. One can see that for initial distributions closer to the Debye length, considerably more detail develops. The disturbance again splits, but now dispersive wave trains propagate outward. The leading wave propagates at the wave speed, but the succeeding ones are slower. Again the size of the waves is of the same order as the original disturbance. It is also noteworthy that as the original disturbance (b) gets smaller, the leading wave becomes less important and the bulk of the structure shifts toward $\xi = 0$. In the b = 20 case, the only waves of any importance are the leading waves. In the b = 3 case (Fig. 5.2), a wave train develops, but the leading waves are still the largest. In the b = 1 case (Fig. 5.3), however, the leading waves become weaker with time, and the newly formed part of the train near $\xi = 0$ appears more important. At $\xi = 0$ one should see density oscillations at about the ion plasma frequency for the small b case. This result agrees with the observations of Hester and Sonin[27] for the wakes of very small cylinders.

The reason for this type of behavior becomes clearer if one looks at the original disturbance. The density distribution at $\tau = 0$ contains the full spectrum of Fourier components. Each component is added with a certain weighting factor to give the require distribution. For the b = 20 case, the original disturbance is made up mostly of long wavelength components and the contribution of the short wavelength part of the spectrum is small. For this type of dispersive wave, the long wavelength components propagate faster than the short ones. Thus in the b = 20 case, the long wavelength

component, which is most of the total, propagates outward leaving very little of the short wave component to follow. In the b = 1 case, the long wave part is small, yet it still moves fast and makes up the wavefront. The short wave component propagates very slowly, thus most of the disturbance remains near the origin, and the leading wave is almost negligible.

V. 1. 4. The Cylindrical (Disc) Case

In the cylindrical case, the counterpart of the cosine initial distribution is the Bessel function distribution given by:

$$\begin{aligned} \frac{N'(\xi, 0)}{N_{i0}} &= A\, J_0(\alpha_1 \rho/b) && r \le b \\ &= 0 && r > b \end{aligned} \qquad (5.25)$$

where α_1 is the first root of $J_0(\rho)$, and A is again taken as unity. The results are similar to those of the one-dimensional case with a few expected differences due to the axial symmetry.

For wide disturbances (b = 20) as in Fig. 5. 4, a smooth cylindrical wave spreads out with very little fine structure behind it. Due to the axial symmetry the wave decays as it spreads. The long wavelengths characteristic of the b = 20 waves indicate that in the case of the disc wakes, the deficit should have little effect on the fine structure due to the peak, except for a possible effect on the overall density levels near the origin.

Again, as the initial disturbance gets narrower, the importance of the wavefront diminishes. In the b = 3 case of Fig. 5. 5, the wavefront still propagates at the wave speed; but by $\tau = 10\pi$, it is almost indistinguishable. Oscillations at the origin which produce waves of

about the same wave length as the original disturbance are still in evidence.

V. 1. 5. Effect of the Initial Velocity Distribution

Though we were unable to examine easily the effects of an initial velocity distribution in the cylindrical case due to computer time limitations, we were able to study some simple distributions for the one-dimensional case. For two streams with relative velocities below the ion acoustic speed, there will be an interaction, and a definite effect is noticeable in the linearized case we have worked with. The experimental velocity distribution (Section V. 2), not including that due to the beam divergence, was simulated with:

$$\begin{aligned} \frac{v}{c}(\xi, 0) &= -\frac{v_0}{c}\,\mathrm{Sin}\left(\pi\frac{\xi}{\beta}\right) && |\xi| \le \beta \\ &= 0 && |\xi| > \beta \end{aligned} \tag{5.26}$$

Using b = b, $\beta = 25$, and $v_0/c = \frac{1}{2}$, the results shown in Fig. 5.6 are obtained. The results are as one would expect. The inward velocity causes a sharp increase in the density near $\xi = 0$ for small times. The velocity distribution also steepens the wavefront and forms a deficit at larger values of ξ. At later times, the added peak caused by the inward velocity decays, and the end effect is to raise the density level of the outward propagating wave train slightly and to steepen the wavefront. It does not seem unreasonable to extrapolate this result to the cylindrical case and to guess that the effects will be similar, and that the density increase at $\xi = 0$ for small times will be larger due to the axial symmetry.

V. 1. 6. Effects of Non-Zero Ion Temperature

No independent investigation of ion temperature effects was made in the framework of this study. However, a considerable amount of information is available on this subject from the literature. Closely related theoretical work was done by R. J. Mason at Bell Laboratories on the structure of ion-acoustic fronts in collisionless plasmas.[29, 30] His acoustic waves are directly comparable to the solutions given by our far wake theory, and his results are similar to ours and to Jack Hill's.[32] He has taken into account the electron to ion temperature ratio, T_e/T_i, and has found that for T_e/T_i as low as 5, almost all the fine structure in his waves is damped out in a very short time. This result probably means that much of the fine structure seen in the theoretical wake structures would not exist if we had assumed $T_e/T_i = 0(1)$, as is the case in the space envoronment.

V. 1. 7. Transformation to Steady State

In order to compare the theory with the experiment, we must replace τ in the theory with the corresponding distance, behind the initial disturbance. This process is complicated by the density variation with distance. Ordinarily the relation between τ and distance would be given by:

$$\tau = \omega_{pi} t = \omega_{pi}(Z-Z_p)/U \quad , \qquad (5.27)$$

where U is the beam velocity and Z_p is the experimental peak (or other initial condition) position. Assuming the beam to be a perfect source

flow, the ion density varies as the inverse square of the distance from the origin of the beam. Thus:

$$\omega_{pi} = \sqrt{\frac{e^2 N_{i0}}{\epsilon_0 M_i}} \frac{|Z_0|}{Z+|Z_0|} \quad , \tag{5.28}$$

where $|Z_0|$ is the distance from the apparent source to the model. The subscript zero indicates experimental values at the model position, $Z = 0$. The relationship of τ to Z is postulated to be given by: $d\tau = \omega_{pi}(Z)\frac{dZ}{U}$. Integrating:

$$\tau = \int_0^t \omega_{pi}\, dt = \int_{Z_p}^{Z} \left(\frac{e^2 N_{i0}}{\epsilon_0 M_i}\right)^{\frac{1}{2}} \frac{|Z_0|}{Z+|Z_0|}\, dZ/U \tag{5.29}$$

$$\text{or} \qquad \tau = \omega_{pi0} \frac{|Z_0|}{U} \operatorname{Ln} \frac{Z+|Z_0|}{Z_p+|Z_0|} = \frac{|Z_0|}{h_0 S} \operatorname{Ln} \frac{Z+|Z_0|}{Z_p+|Z_0|} \quad ,$$

where Z_p is the experimental peak (or other initial condition) position. Thus:

$$Z/a = \frac{Z_p+|Z_0|}{a} \exp\left(\frac{\tau h_0 S}{|Z_0|}\right) - \frac{|Z_0|}{a} \quad , \tag{5.30}$$

For large Z (the far wake region) the density does not vary much across the wake, and h can be assumed independent of r; thus ρ is converted to r/a by:

$$\frac{r}{a} = \frac{\rho h}{a} \tag{5.31}$$

where h is the local Debye length given by:

$$h = h_0 \left(\frac{Z+|Z_0|}{|Z_0|}\right) \tag{5.32}$$

V.2. Experimental Study of the Far Wake

In this section, the experimental results will be given for

various initial or boundary conditions as presented by the near wake. The effects of the collective plasma properties (T_e, S, etc.) will be examined, and the experimental results will be related to the theory wherever possible. As in Chapter IV, the models used are discs and strips. The wakes of some other models are presented in Appendix 5.

V.2.1. Effects of Electron Temperature and Ion Density

If the experimental far wakes are truly wave phenomena, the observed characteristic lengths and times should scale with the collective parameters of the plasma. Electron temperature and ion density are expected to affect the structure of the far wake through the relevant time and length scaling factors they define. The theory predicts that the problem can be transformed to a time dependent one and that the experimental wake structures for identical normalized initial conditions should be the same at a given normalized time after the initial disturbance. This transformation is dependent on the beam speed and the square root of the ion density. If the beam velocity is held constant, a factor of 4 decrease in free stream ion density will decrease the normalized time, τ, equivalent to a distance, Z, by a factor of 2.

The electron temperature comes into the problem through the Debye length. If for a given peak shape, the electron temperature is lowered by a factor of 4, and the ion density remains constant, then the peak is expected to double its width in transformed, normalized coordinates.

The experiments are complicated by the divergence of the beam and the varying Debye length over the span of the far wake, but

the data are clear enough for the general trends to be established and compared with the theoretical model.

Fig. 5.7 shows the far wake of a thin disc in a geam generated using the high mode of the source. The beam velocity is only 15% higher than that in Fig. 4.6, but the freestream ion density is almost a factor of 4 lower. The electron temperature in Fig. 5.7 is 1/6 that in Fig. 4.6, making the speed ratio 31 as opposed to 11 but keeping the Debye lengths within 20% Table 5.1 compares the parameters of Fig. 5.7 with those of Fig. 4.6.

The curves for the high speed ratio case were taken at the same axial stations as those of Fig. 4.6, yet at the Z/a = 30 station, the S = 31 peak is still well formed while the S = 11 peak has split and started propagating outward.

This behavior is not surprising in light of the theoretical results. In terms of scaled variables, both of the initial peaks are about the same size and would in theory be expected to behave similarly as a function of time, τ. This is indeed the case. Transforming to time dependent coordinates as shown in Section V.1.7, the Z/a = 30 position of Fig. 4.6 is equivalent to 3 plasma periods ($\tau = 6\pi$) after the initial peak (Z/a = 6), while the Z/a = 30 case of Fig. 5.7 corresponds to only 1.6 plasma periods ($\tau = 3.2\pi$).

From Table 5.1, the Z/a = 30 curve of Fig. 5.7 should really be comparable to Z/a of about 17 on Fig. 4.6. The resemblance here is closer, though the S = 31 curve lacks the detail of the S = 11 curves. Nevertheless, the comparison does show that the theory is relevant to the problem at hand.

Some differences between the S = 31 and S = 11 curves must be expected due to the different natures of the sources, beams and initial conditions, but it should be noted that the lack of detail in the S = 31 curves may be due to ion temperature. If one assumes that the ion temperature is about the temperature of the operating source, say 400°K, and the electron temperature is measured at .2V(2200°K) then T_i/T_e is 18%. This is within the range where ion temperature damping can be expected.

V.2.2. Dependence of Far Wake on Initial Conditions

In order to understand the evolution of the far wake, one must first know the upstream boundary or initial conditions presented by the near wake. It has been noted previously that the far wake is wave-like in nature,[27, 28] but the waves which result from the peak disturbance have been poorly understood. The confusion is due in some part to a poor understanding of the upstream conditions and of the medium into which the waves propagate.

Since the beam energy is approximately constant over the far wake, the flux measured by our probe corresponds to ion density. During this discussion we will refer to measurements of ion density. These are really the flux measurements previously discussed.

In this investigation, two basic types of upstream conditions have been generated. The one studied most has been the axial symmetric wake dominated by a density peak. The other is the wake of a strip, dominated by the density deficit or shadow region, but including a small density peak on the axis. The Z/a = 6 curve on Fig. 4.2 can be taken as typical of the axial symmetric initial conditions.

The strip initial condition is the $Z/a = 2$ curve of Fig. 4.8.

Both of the above initial conditions result from the same sort of body-stream interaction, yet in the axial symmetric case, the peak is dominant. This is a strong indication that symmetry is important and should be considered in the study of the far wake. It should also be noticed that in both cases, the actual interface between the wake region and the free stream is at the outer edge of the ion deficit. Thus any waves formed as a result of the peak will propagate into a region already disturbed by the ion deficit.

The upstream density distribution is straightforward and can be obtained directly from Figs. 4.2 and 4.8. The radial velocity distribution, $v(r, Z)$ or $v(x, Z)$, which represents the initial velocities in the analogous time dependent problem, is harder to find. Fig. 5.8 shows the radial velocities for the two flux distributions selected as sample initial conditions, and for two curves downstream of the initial conditions. The velocity curves were obtained by a crude integration of the continuity equation. For the axial symmetric case, continuity gives:

$$rN_i(r)v(r) = -\int_0^r r \frac{\partial(N_i U)}{\partial Z}\, dr$$

The $\frac{\partial(N_i U)}{\partial Z}$ term for a given r at $Z/a = 6$ was taken to be:

$$\frac{N_i U(r,\ Z/a = 6) - N_i U(r,\ Z/a = 4)}{2a} ,$$

thus $$\frac{v(r, Z/a)}{c} = \left(-\frac{1}{r}\int_0^r r \frac{\partial(N_i U)}{\partial Z}\, dr\right) \frac{S}{N_i U(r, Z/a)} .$$

For the strip case we get similarly:

$$\frac{v(x, Z/a)}{c} = \left(- \int_0^x \frac{\partial (N_i U)}{\partial Z} dx \right) \frac{S}{N_i U(x, Z/a)} \quad .$$

One should notice that in both cases, there is an appreciable inward directed velocity in the disturbed region. Moving outward, this velocity decreases and then shifts to an outward velocity, eventually reaching the free stream condition given by the diverging beam.

Let us examine the development of the wake farther downstream (or at a later time, depending on the point of view). In the axial symmetric case of Figs. 4.2 and 4.3 the edge of the deficit spreads out, theoretically at the wave speed relative to the diverging beam. The exact speed is hard to define, because as a result of the axial symmetry, the deficit quickly becomes small and the edge ill-defined. The peak, on the other hand, appears to be reinforced because of the inward velocity in the center region and the focusing effect of axial symmetry. The peak eventually splits and a disturbance moves outward. It has been noted by Hester and Sonin that the leading edge of the peak disturbance did not necessarily propagate at the wave speed relative to the diverging free stream. As shown in Fig. 5.8, this disturbance does not propagate into the free stream but into a previously disturbed region with a velocity distribution which may effect the disturbance.

From Figs. 4.6 and 4.12 one can see that changing the height of the peak slightly varies the fine structure of the peak disturbance, but basically the large peak decays into a series of small ripples. In the cases observed, we have not seen more than two ripples, but the results of Section V.1 suggest that more would develop if we went

farther downstream. The wave length of the observed ripples is of the order of half the peak width, about 5 to 10 Debye lengths.

It is interesting at this point to look at the theoretical predictions for the conditions of Fig. 4.6. Fig. 5.9 shows the result for a simulated peak with b = 10. No initial velocity distribution is included. The curves are marked both in terms of τ and ρ and with Z/a and r/a. The values of Z/a and r/a are found for the conditions of Figs. 4.5 and 4.6. The $\tau = 0$ curve is associated with the Z/a = 6 curve of Fig. 4.6. The density scales on Fig. 5.9 should be related to the free stream density at the given Z/a.

Comparing Fig. 5.9 to Fig. 4.6, it is easy to see that the theoretical densities near r/a = 0 are much too low. This discrepancy is an indication of the non-linearity of the experimental situation (ΔN large) and of the importance of the initial velocity distribution. The linear theory does, however, appear to be valuable for predicting the qualitative nature of the wave structure resulting from the peak, i.e., the spreading of the disturbances and the amount of fine structure to expect.

The amount of structure seen in the experiments is in qualitative agreement with the theory, and the fact that only two oscillations are observed in the Z/a = 30 curve of Fig. 4.6 is due to our inability to probe very far downstream. The theory indicates that what we have called the far wake is really only the beginning of it. We have only been able to probe about the equivalent of three plasma periods ($\tau = 6\pi$) of the peak disturbance region. In the absence of ion temperature and a decaying beam, much more structure should be

present farther downstream.

Fig. 5.9 also predicts that with no initial velocity perturbation, the wave lengths of the leading waves resulting from large disturbances should be on the order of the original disturbance size. The observed oscillations are smaller, and this difference may also be due to the initial velocity disturbance or to nonlinearity resulting from the large magnitude of the peak.

We have experimented with other axial symmetric models which have produced peaks slightly different from those of the discs. The results, shown in Appendix 5, are similar to those of the discs, but the fine structure of the far wake is changed slightly due to the changes in initial conditions.

The far wake of the strip is quite different from that of the axial symmetric models. Without axial symmetry, the size of the deficit is not so rapidly reduced,and the defect edge remains distinct far downstream. Since the edge of the deficit is propagating into the free stream, it should, in theory, move outward at a speed given by the wave speed plus the outward component of the beam speed in a coordinate system moving with the axial component of the beam speed. The slash at $x/a = 3.1$ on the $Z/a = 4$ curve of Fig. 4.8 indicates the edge of the deficit at $Z/a = 4$. The circles on the succeeding curves of Fig. 4.9 indicate the position to which the edge should have progressed using the above speeds. In calculating the theoretical edge, the beam was assumed to have a source flow structure, although in fact it slightly deviates from source flow. This effect is slight, however, and the wave front prediction (the circles)

should not be much in error. The position of the circle on the $Z/a = 6$ curve was calculated using the following approximate formula:

$$\frac{x_{edge}}{a}(Z/a=6) = \frac{x_{edge}}{a}(Z/a=4) + 2a\left[\frac{x_{edge}}{Z+|Z_0|}(Z/a=4) + \frac{1}{S}\right]$$

where the quantity in brackets is approximate for small angles. The rest of the edge positions were calculated similarly. As one can see, the agreement with the theoretical edge is quite close.

In the disc case, the very high ion density of the peak gives rise to the possibility that the ions in the peak region interact by some mechanism and lose their inward directed motion. By continuity considerations, this results in the continued importance of the peak farther downstream.

In the strip case, the peak formed by the two converging ion streams is apparently not sufficiently large for the ions to interact much with one another. The $Z/a = 4$ curve on Fig. 5.8 indicates that immediately after the peak, the average radial (x) velocity of the ions near the center of the wake is outward as opposed to inward in the disc case. This indicates that the two ion streams cross through each other with little interaction and are soon lost in the "walls" of the ion defect, leaving the deficit as the main characteristic of the far wake.

In this case, there was no wave structure associated with the peak. It is possible, though, that a wave pattern might develop with a wave length on the order of the deficit size. The one-dimensional theory predicts that for large deficits the defect splits, and two waves of half the magnitude and of the same wave length as the original

disturbance spread out. For a disturbance of the width of that shown in Fig. 4. 9 ($\sim$ 60h), the splitting takes a normalized time of about $\tau = 7\pi$. With our apparatus this is slightly farther downstream than we could probe. The Z/a = 30 curve of Fig. 4. 9 might possibly show this structure if the beam density were not too low for proper resolution.

VI. EFFECT OF BACKGROUND PRESSURE ON THE SIMULATION OF SATELLITE WAKES

It was mentioned in Chapter I that charge exchange collisions generate an appreciable number of low energy ions if the background pressure is too high. In the beginning of this study, it was not at all clear how low the neutral background pressure has to be to make the slow ion effect negligible. This question has been raised by several workers in the past.[24, 26, 27] In order to determine the importance of slow ions and the effect they may have had on earlier data, the dependence of the wake structure on background pressure was explored experimentally.

VI. 1. Effects of Background Pressure on the Near Wake Structure

Keeping the pressure and other source parameters constant, we examined the wake of a thin, ($L/h \ll 1$), 2.5 cm diameter disc at various values of test section background pressure by bleeding argon directly into the test section. Appendix 3 demonstrates that high background pressure causes a high density of slow ions. The effect of these slow ions on the wake is shown in Figs. 6.1, 6.2, 6.3, and 6.4. Fig. 6.1 shows the near wake of a thin, highly negative disc for various pressures. The traces are the usual plots of ion flux versus radius for various distances behind the model. The gross features of this near wake are affected very little by the variation of background pressure from 10^{-5} to 10^{-4} torr. The fine details of the wake structure, on the other hand, are almost totally smoothed out by slow ions at the high pressures.

Fig. 6.2 will be discussed in the section on far wakes. Figs. 6.3 and 6.4 are traces of ion flux along the axis behind the same disc. Current is plotted versus distance behind the body for various pressures and for two values of body potential.

From Fig. 6.3, one can see that for highly negative values of body potential, the slow ions make little difference in the position of the flux peak. The peak moves downstream about 10% with a factor of ten pressure rise. The wake also fills in slightly in front of the peak, indicating the presence of slow ions in the swept region. Close to the body, there may be more slow ions present that the probe measures. The body is more negative than the probe and would tend to draw the slow ions away from the probe.

Slow ions in the near wake will reduce the negative space charge and the electric field in the void with it, causing the peak to move downstream. As evidenced by Fig. 6.3, this effect is slight for highly negative bodies, and the body sheath is primarily responsible for the near wake structure. Thus, observations of the near wakes of highly negative bodies at high pressures are probably valid for low pressures as well.

For slightly negative bodies, the slow ion and collision effects are much more pronounced. Peaks are generally farther downstream in this case. Since the body is near plasma potential, the sheath effects are not as strong. Any potential gradients in the swept region have proportionally more effect on the nearby ion stream. Thus, changes in the swept region near the body should have a much larger effect on peak position and structure than would be the case for

highly negative bodies.

Fig. 6.4 dramatically bears out this reasoning. For the 10^{-5} torr case, the near wake of the slightly charged disc has the characteristic ion shadow near the disc and the ion peak following farther downstream. The curve for 10^{-5} torr lacks the indications of slow ions, as do similar curves taken at pressures as low as 5×10^{-6} torr (not shown here). For the original beam, described in Appendix 1, we have estimated the ratio of slow to fast ions at 10^{-5} torr to be less than 1 to 20, while at 10^{-4} torr the ratio climbs to 2 to 1 (Appendix 3). For the narrower second generation beam used here, the ratios should be less than half of those for the wide beam.

An increase in pressure to 5×10^{-5} torr raises the slow ion to fast ion ratio (N_s/N_f) to about $\frac{1}{2}$ (Appendix 3). Large numbers of slow ions are scattered into the near wake close to the disc, partially filling in the shadow region. Potential gradients in the swept region are reduced, the focusing of the beam ions is lessened, and the peak weakens and moves downstream.

Further increase in the background pressure to 10^{-4} torr raises N_s/N_f to about 1, and the peak structure is all but destroyed. The near wake is completely dominated by slow ions, and only a hint of a peak is noticeable at $Z/a \sim 11$ as opposed to $Z/a \sim 5$ for the 10^{-5} torr case.

From this examination of the effects of pressure on the near wakes, we can see that slow ions are very important in the wakes of bodies at or near the plasma potential. They do not, however, influence greatly the near wake of highly negative bodies.

It is known that an ion to electron temperature ratio (T_i/T_e) as high as 15% will severely damp waves in a plasma.[29, 30] In the ionosphere, T_i/T_e is of the order of 1, and damping of the fine structure of satellite wakes should be expected, especially in the far wake. The slow ions in our experiments at higher pressures have an effect analogous to that of ion temperature since they represent a "broadening" of the ion distribution function. It might be possible to take account of them by defining some effective ion temperature. A high percentage of slow ions at the higher pressures would correspond to high values of T_i/T_e.

It should be recognized that ion temperature damping is a purely collision-free phenomenon, whereas the slow ions are formed by close collisions between ions and atoms. However, since all the ion mean free paths are much greater than the body radius, collisions may be neglected per se, and only their result, that there is an average ion temperature greater than zero, need be taken into account. In any case, the data at high pressures are expected to give some insight into the effect of ion temperature.

VI. 2. Effects of Background Pressure and Slow Ions on the Far Wake

As mentioned in Chapter VI. 1, an appreciable number of charge exchange collisions will take place between the beam ions and the background atoms if the vacuum chamber background pressure is too high. These collisions form slow ions which change the ion distribution function from a single delta function into a more spreadout, bimodal shape and thus interact with the wake in a way which approximates the effects of ion temperature.

Figs. 6.1 and 6.2 best illustrate the effects of these slow ions on the far wake. The initial conditions for all three cases shown on Fig. 6.2 are approximately the same. All have fairly large peaks, although the deficit next to the peak in the 10^{-4} torr case is somewhat filled in by slow ions. The ion speed ratio, S, the electron temperature, and Debye lengths are approximately the same for each case; thus, any given distance behind the model corresponds to the same time after the initial condition for all three cases.

From Fig. 6.2, the effect of the slow ions on the far wake is clearly a damping of the wavelike disturbances which are present if $T_i/T_e \cong 0$. In the 10^{-5} torr case, the peak splits, and a distinct wave structure propagates radially outward. As the pressure is increased, the peak merely decays, and the fine structure is wiped out. In Fig. 6.2, the $Z/a = 30$ curve of the 10^{-4} torr case exhibits no fine structure, as if the peak did not exist at all. We surmise that the effect would be similar for a collisionless beam with T_i of the order of T_e. This result is in agreement with the predictions of R. J. Mason (Chapter V. 1. 6) on the effects of ion temperature.

VII. CONCLUSION

In this investigation the flow of a "hypersonic" plasma past various large models has been studied. The experimental conditions approximately simulate those experienced by satellites about a meter in diameter between 200 and 500 km above the Earth.

The structure of the wakes of models in this type of flow has been shown before in a qualitative fashion. The characteristic features of the wake such as the void region, the peak region, and the wavelike peak disturbance, have been observed in the past, but the parameters affecting this structure have not been well understood.

In this investigation, the essentially different nature of the near and far wakes has been demonstrated, and the parameters governing the structure of each have been identified. A crude theoretical model has been advanced which predicts certain features of the near wake and gives some insight into the experimental results. The hypersonic analogy was used for the first time in the theoretical study of the far wake, and the results of the near wake study were used to define the initial conditions for the time dependent problem.

The structure of the near wake is described using the body potential and the size of the body as characteristic scales. The sheath region near the body is a region of relatively large electric fields which result in significant deflections of individual ion trajectories. The electric field in the sheath at the edge of the body controls the axial extent of the near wake region in the case of large body potentials. The electric field associated with the ion-free shadow region behind the body becomes of comparable importance for small

(floating) body potentials only.

The degree of symmetry of the model has also been found to be an extremely important factor in the formation of the wake features. For axial symmetric bodies, the peak disturbance is found to dominate the far wake, while for strip models, the peak disturbance is insignificant compared to the ion deficit.

When appropriately scaled and transformed to the analogous time dependent problem, the structure of the far wake appears to be dependent on the collective properties of the plasma and on the initial conditions presented by the near wake. The far field is shaped chiefly by the propagation of dispersive waves. Distances are scaled with the Debye length and times with the ion plasma frequency. The beam velocity enters through the transformation, and the other factors affecting the near wake enter only through the initial conditions presented for the far field.

Certain details of the fine structure of the experimental wakes were not accurately predicted by the theory, but this appears to be a result of the simplifications and linearizations necessary to obtain a solution. The experimental results, however, confirmed the general trends predicted by the theory for both the cases of the strip and the axial symmetric models.

Previously, the effects of charge exchange collisions and the resulting low energy ions have been ignored or assumed non-existant in this type of experimental investigation. An important contribution of this study has been the analysis of the effects of collisions and low energy ions on the proper simulation of satellite wakes in the

ionospheric plasma by exploring the effects of chamber background pressure. The analogy between the effects of low energy ions and ion temperature has also been noted.

The understanding of satellite wakes is still far from complete. The effects of a magnetic field on the wake structure have still not been determined. In the ionosphere, the electrons are closely coupled to the field lines, and magnetic effects may be important. The structure we have observed experimentally may well be modified by electrical interactions between the ions and the constrained electrons.

The effects of finite ion to electron temperature ratio are still not well understood. An experimental investigation of T_i/T_e is difficult since it is hard to produce either hot ions or cold electrons so that the ratio may be raised. A theoretical study, however, is not at all unreasonable.

In addition to the study of the effects of magnetic fields and finite T_i/T_e, more study of the peak region behind axial symmetric models is needed. It is suggested that there may be an instability mechanism which destroys the inward directed motion of the ions in the vicinity of the flux peak. It is this mechanism which enables one to examine the far wake from a continuum point of view, since it randomizes the velocity differences between the ion streams and develops a single, nearly Maxwellian ion distribution function downstream of the peak. This instability mechanism is not understood at present, but presumably is analogous to the much investigated ion counterstreaming instabilities.

This study has been limited to models much smaller than the ion-ion or ion-neutral mean free path. For extremely large satellites or space stations in the lower part of the ionosphere, collision effects may take on more importance. Note that this problem is different from the ion-neutral collisions examined in the present study where the neutral mean velocity with respect to the body was approximately zero. In the real case, ions and neutrals possess a common, large mean velocity the simulation of which would require a completely new technique.

In future studies, the experimental simulation can be improved by using a source with a larger orifice providing a more uniform beam. The simulation can be even further improved when investigating the effects of a parallel magnetic field because the field can be used to shape the ion flow and produce a more parallel beam.

Since one reason for the study of satellite wakes is to get a better understanding of radar returns from satellites, a comparison of the experimental and theoretical results with actual radar returns would be valuable. Unfortunately, information on actual radar returns is in short supply in the open literature.

TABLE 1.1

Approximate Conditions in the Ionosphere and Lab

	Altitude						
	100 Km	200 Km	300 Km	500 Km	700 Km	1000 Km	Lab
Body Dimension (m)	1-10						0.02
Satellite or Beam velocity (m/sec)	8×10^3						$(15\text{-}40)10^3$
Electron Temp. (^oK)	230	650	1000	1800	2000	3000	2000 - 50,000
Ion or Electron Density (m^{-3})	$(2\text{-}100)10^9$	$(3\text{-}50)10^{10}$	$(1\text{-}200)10^{11}$	$(4\text{-}10)10^{11}$	$(2\text{-}5)10^{11}$	10^{11}	10^{13}-10^{14}
Debye Length (cm)	1	0.2 - 1	0.1-0.7	0.3-0.6	0.4-0.7	1	$\sim 10^{-1}$
Electron Thermal Speed) (m/s)	$(9.4)10^4$	$(1.5)10^5$	$(1.0)10^5$	$(2.5)10^5$	$(2.9)10^5$	$(3.4)10^5$	$(3)10^5$-$(1.5)10^6$
Ion Thermal Speed (m/s)	$(4)10^2$	$(7)10^2$	$(9)10^2$	$(1.4)10^3$	$(1.6)10^3$	$(2.4)10^3$	$(5)10^2$
Charged Particle Mean Free Path (m)	$(5)10^1$	$(6)10^1$	$(7)10^1$	$(4)10^2$	10^3	$(8)10^3$	15
Neutral Mean Free Path (m)	10^{-1}	$(5)10^1$	10^3	$(6)10^4$	$(5)10^5$	$(8)10^6$	5
Neutral Density (m^{-3})	10^{11}	10^{16}	10^{15}	10^{14}	10^{13}	10^{12}	3×10^{17}

TABLE 1.2

Dimensionless Parameters

Parameter	Flight (300 Km)	Simulation
$S = U/\sqrt{K(T_e+T_i/M_i}$	$\gg 1$	$\gg 1$
$\alpha = (-2\, e\varphi_M/M_i U^2)$	$\ll 1$	< 1
a/h (body radius)	$\gg 1$	$\gg 1,\ > 1$
L/h (body length)	$\gg 1$	$> 1,\ < 1$
Ion Larmar Radius (R_i/a)	> 1	$\gg 1$
Electron Larmar Radius (R_e/a)	< 1	$\gg 1$
λ_{i-i}/a	> 1	$\gg 1$
λ_{i-n}/a	$\gg 1$	$\gg 1$
T_i/T_e	0(1)	$\ll 1,\ < 1$

TABLE 2.1

Power Supply Settings for High and Low Mode

	Low Mode		High Mode	
	Volts	Amps	Volts	Amps
Nominal Beam Energy	80V		100V	
Cathode Filament Supply (1)	9.7	20.1	9	18
Magnet Coil Supply (2)	1.6	2.9	2	3.5
Anode Supply (3)	80	3.1	80	3.1
Ion Grid Bias (4)	5		5	
Ion Grid Supply (5)			100	
Neutralizer Bias Supply (6)			0	
Neutralizer Filament (7)			4	20

TABLE 4.1

Experimental Conditions

(All Voltages with Respect to Plasma Potential)

Fig.	Model Type	Model Size	Background Pressure	φ_g	φ_B	φ_M	$S=\sqrt{\frac{2\varphi_B}{KT_e/e}}$	$\frac{KT_e}{e}$	α	a/h(0)
		2a, L-cm	torr	volts	volts					
4.1	Thin Disc	2.54, .013	10^{-5}	-9	71	-9	12	1	.13	21
4.2	" "	" "	"	"	"	"	"	"	"	"
4.3	" "	" "	"	"	"	"	"	"	"	"
4.4	" "	" "	"	-8	72	-8	11	1.2	.11	16
	" "	" "	"	"	"	-28	"	"	.39	"
	" "	" "	"	"	"	-38	"	"	.54	"
	" "	" "	"	"	"	-48	"	"	.66	"
4.5	" "	" "	"	"	"	"	"	"	"	16.5
4.6	" "	" "	"	"	"	"	"	"	"	"
4.7	" "	" "	"	"	"	-48, -8	"	"	.67, .11	17
	Thin Strip	"	"	-10	70	-50, -10	7.1	2.5	.71, .14	10
4.8	" "	" "	"	"	"	-50	"	"	.71	"
4.9	" "	" "	"	"	"	"	"	"	"	"

TABLE 4.1 (Cont'd)

Fig.	Model Type	Model Size	Background Pressure	φ_g	φ_B	φ_M	$S=\sqrt{\frac{2\varphi_B}{KT_e/e}}$	$\frac{KT_e}{e}$	α	a/h(0)
		2a, L-cm	torr	volts	volts					
4.10	Thin Disc	2.54, 0.13	10^{-5}	-8	72	-48	11	1.2	.67	16
	" "	" "	"	"	"	-8	"	"	.11	"
	Thick Disc	2.54, 1.27	"	"	"	-48	9	1.7	.67	13
	" "	" "	"	"	"	-8	"	"	.11	"
4.11	" "	" "	"	"	"	-48	"	"	.67	"
4.12	" "	" "	"	"	"	"	"	"	"	"
5.7	Thin Disc	2.54, 0.13	"	-2	98	-52	31	.20	.53	21
6.1	" "	" "	"	-8	72	-48	10	1.4	.66	"
	" "	" "	5×10^{-5}	"	"	"	"	"	"	"
	" "	" "	10^{-4}	"	"	"	"	"	"	"
6.2	" "	" "	10^{-5}	"	"	"	"	"	"	"
	" "	" "	5×10^{-5}	"	"	"	"	"	"	"
	" "	" "	10^{-4}	"	"	"	"	"	"	"
6.3	" "	" "	10^{-5}	"	"	"	11	1.2	"	"
	" "	" "	5×10^{-5}	"	"	"	"	"	"	"
	" "	" "	10^{-4}	"	"	"	"	"	"	"
6.4	" "	" "	10^{-5}	"	"	-8	"	"	.11	"
	" "	" "	5×10^{-5}	"	"	"	"	"	"	"
	" "	" "	10^{-4}	"	"	"	"	"	"	"

TABLE 5.1

Comparison of Conditions for Figs. 4.6 and 5.7

	Fig. 4.6	Fig. 5.7
Model	Thin Disc	Thin Disc
Background Pressure	10^{-5} torr	10^{-5} torr
φ_B	72V	98V
φ_M	-48V	-52V
S	11	31
$\frac{KT_e}{e}$	1.2	0.2 (High Mode)
α	0.66	0.53
Z_0	22 cm	34.5 cm
h(Z=0)	0.075 cm	0.06 cm
Peak Position, Z_P/a	6	6

TABLE 5.1 (Cont'd)

Scaled Time (τ) For Various Distances After Peak

Z/a	Fig. 4.6 τ	Fig. 5.7 τ
6	0 (0)	0
10	4.22 (1.34π)	2.08 (0.66π)
14	7.81 (2.58π)	4.01 (1.28π)
20	12.4 (3.94π)	6.49 (2.06π)
30	18.7 (5.95π)	10.1 (3.20π)

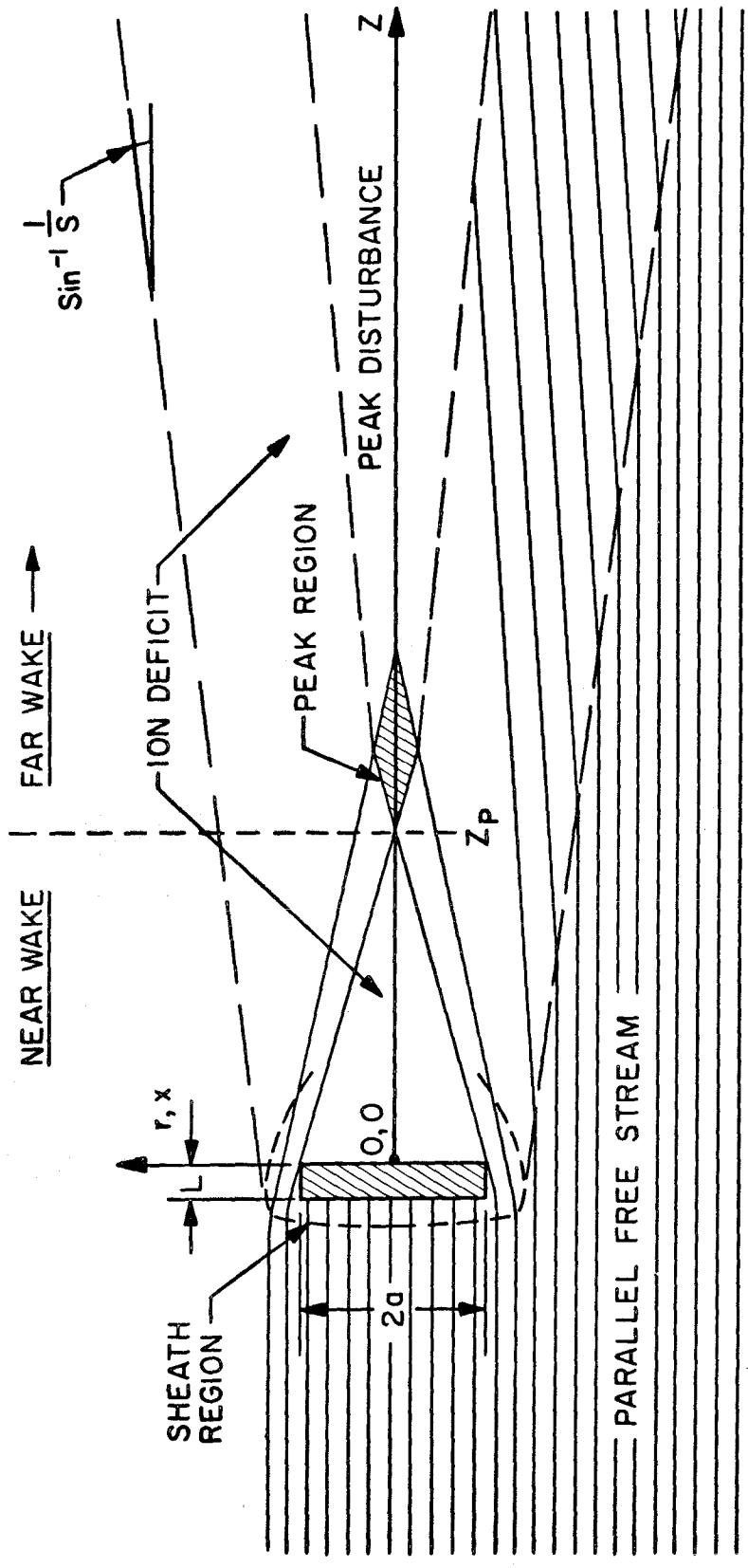

Figure 1.1 Schematic of the Wake of a Wide Body.

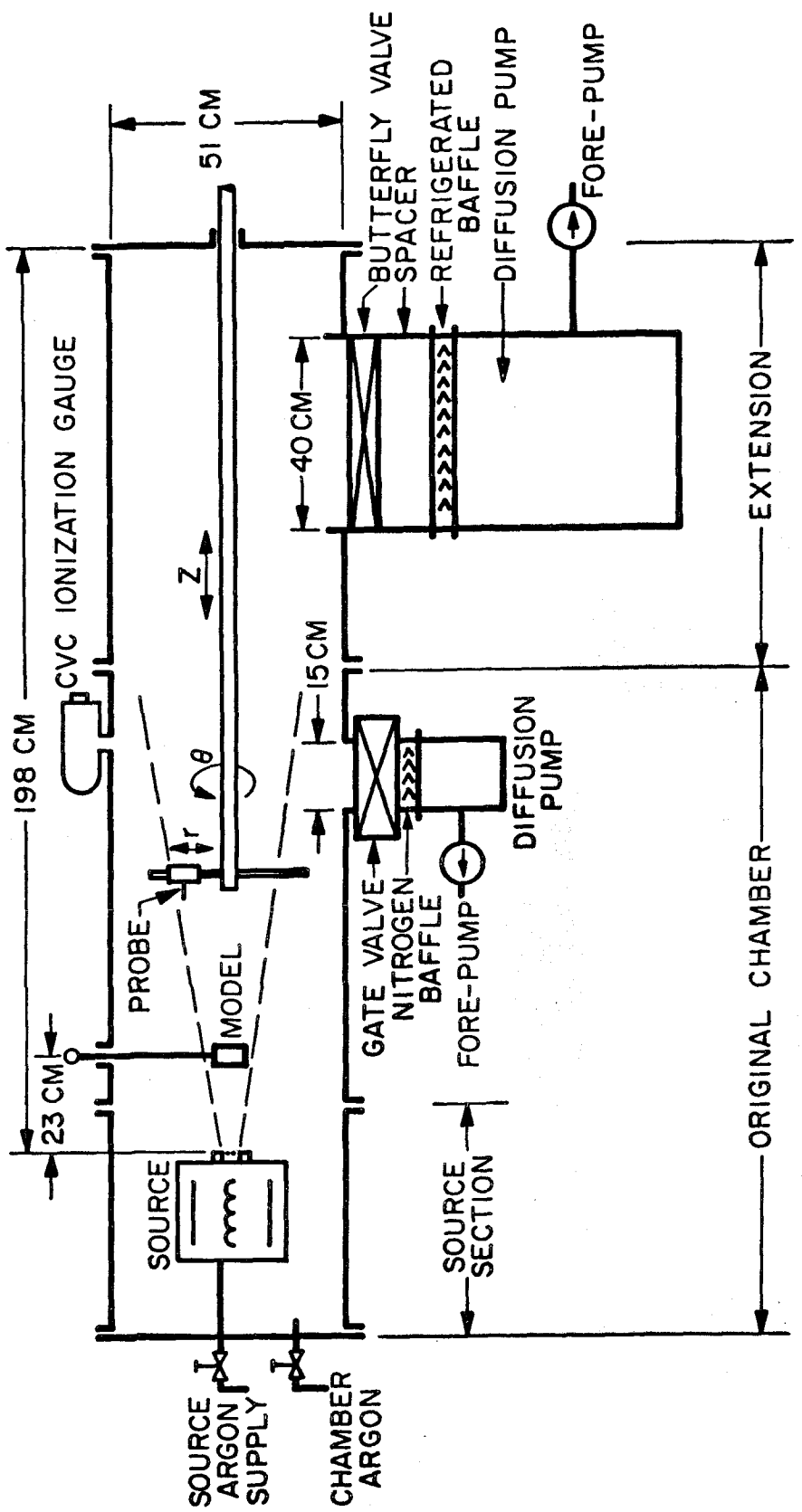

Figure 2.1 Plasma Beam Source and Chamber.

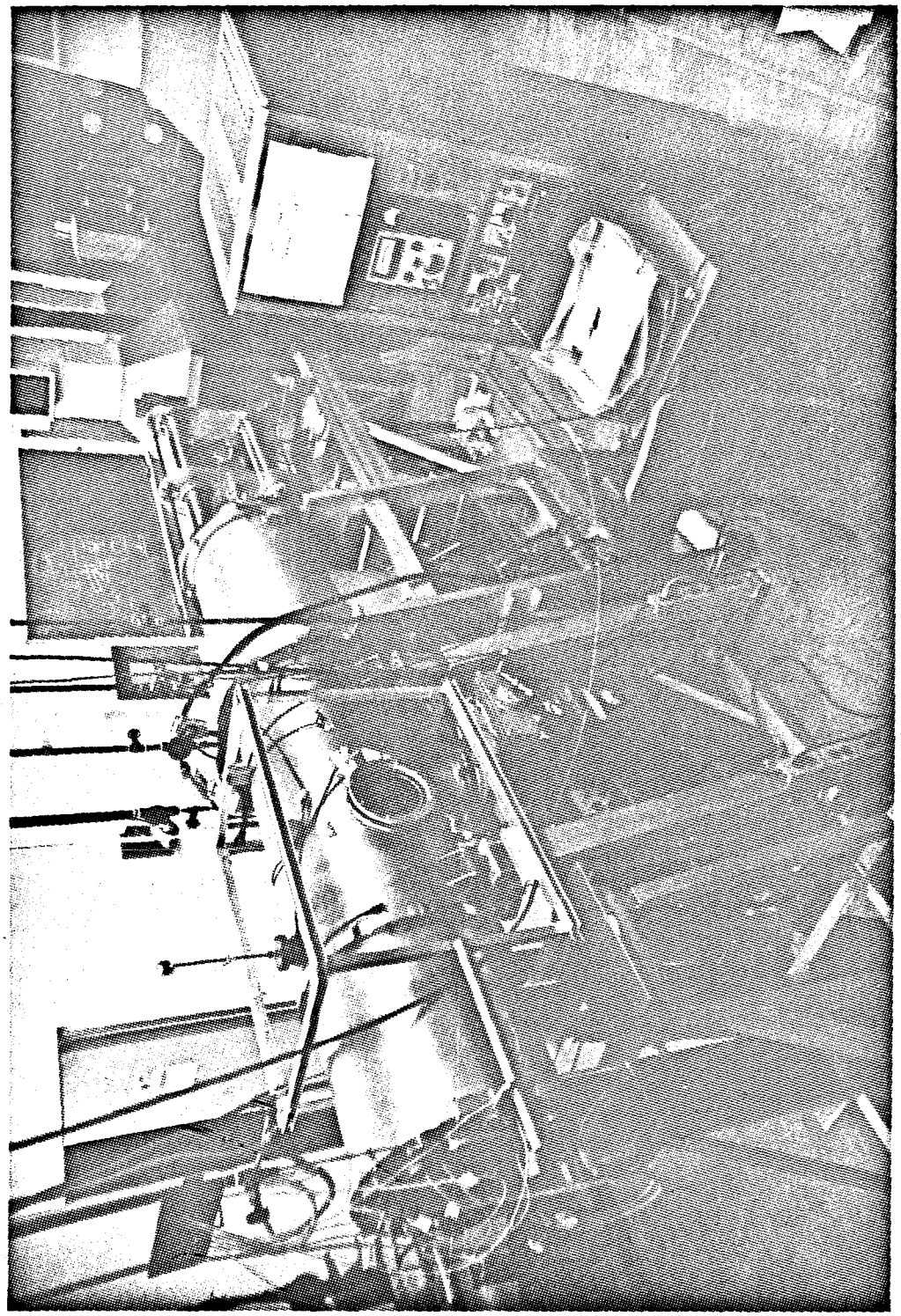

Figure 2.2 Photo of Facility

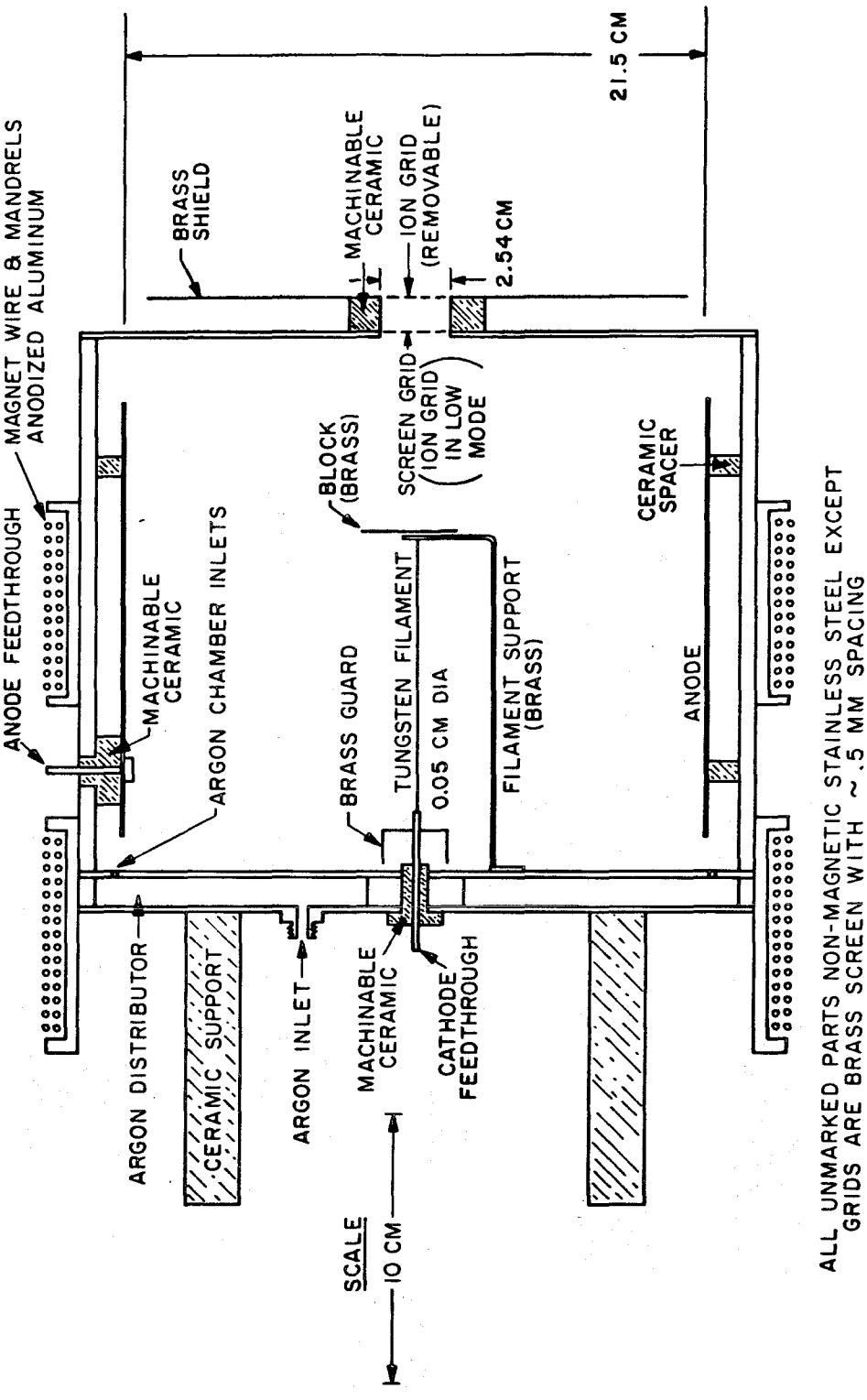

Figure 2.3 Schematic of Source.

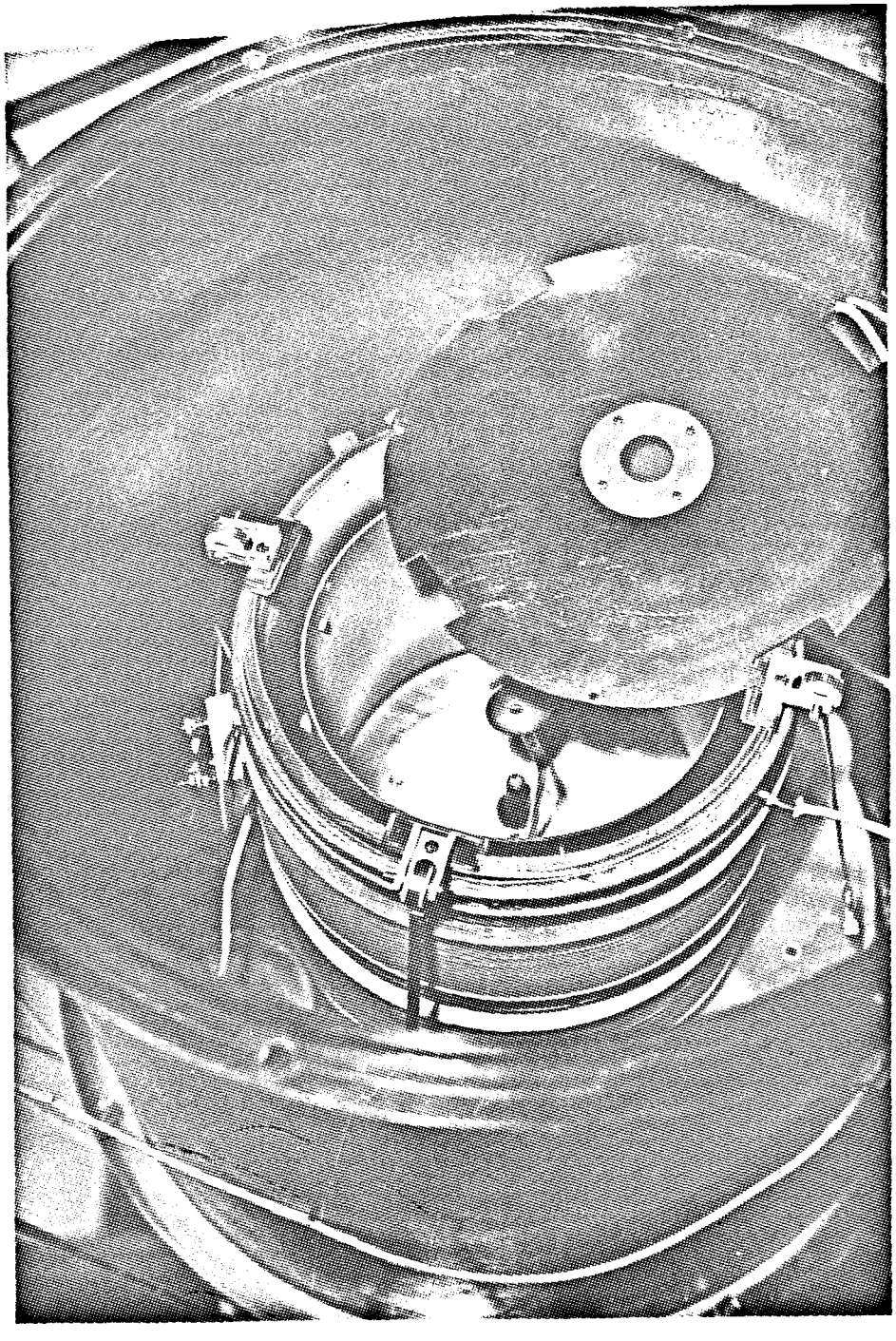

Figure 2.4 Photograph of Source.

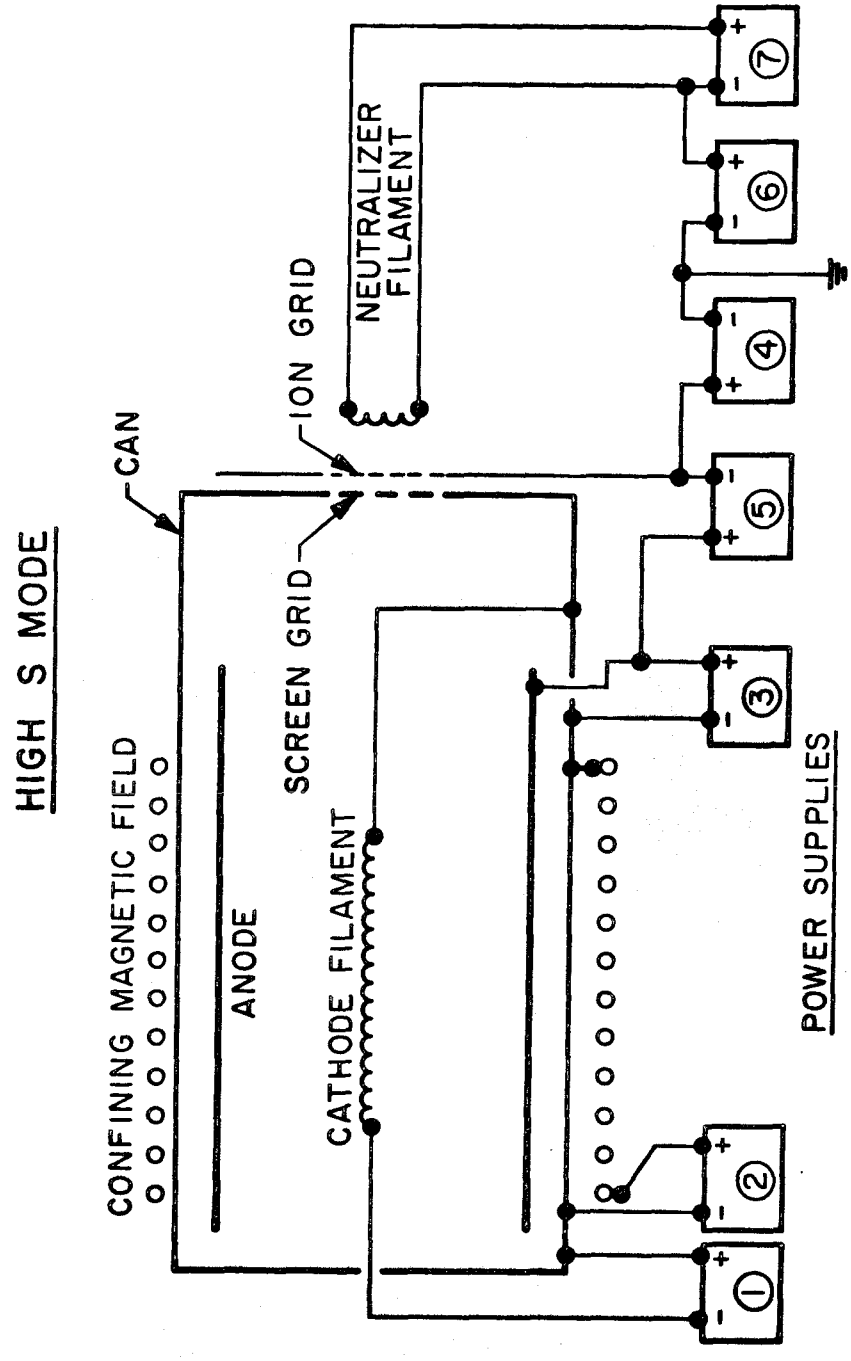

Figure 2.5 High Mode Circuit.

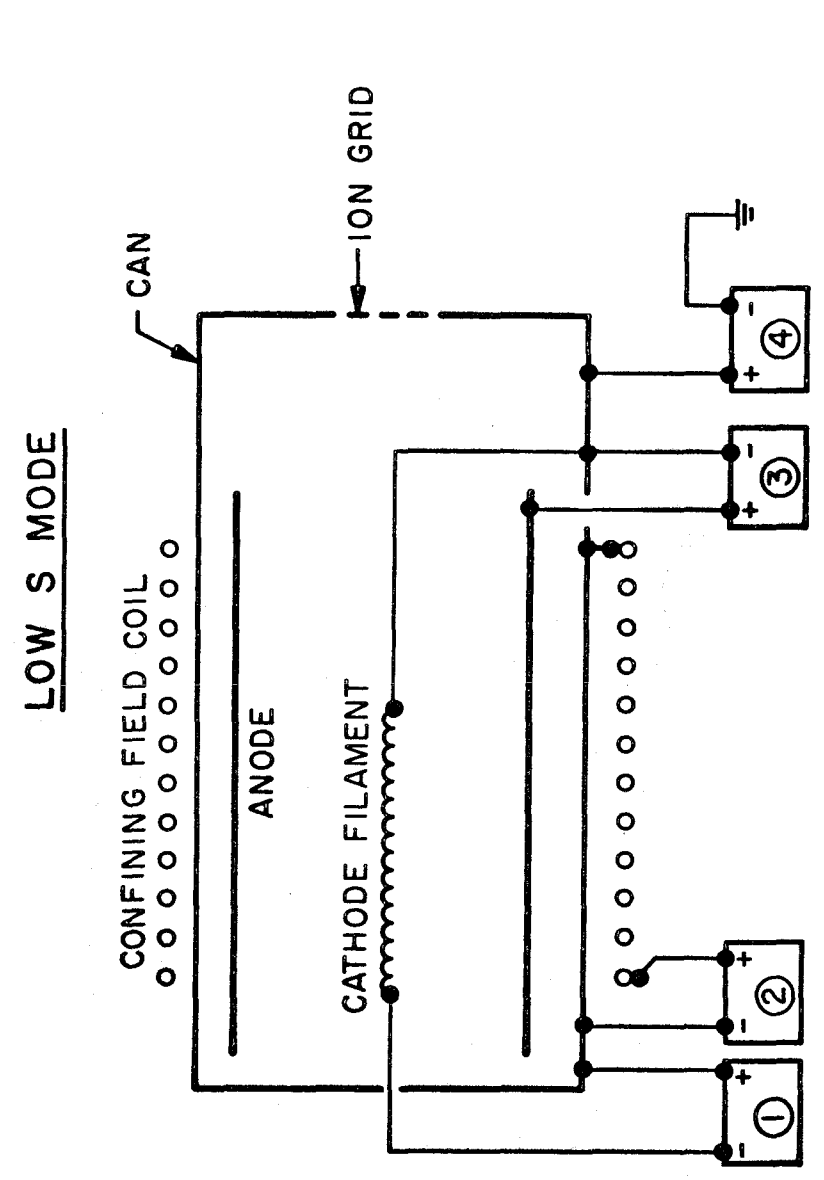

Figure 2.6 Low Mode Circuit.

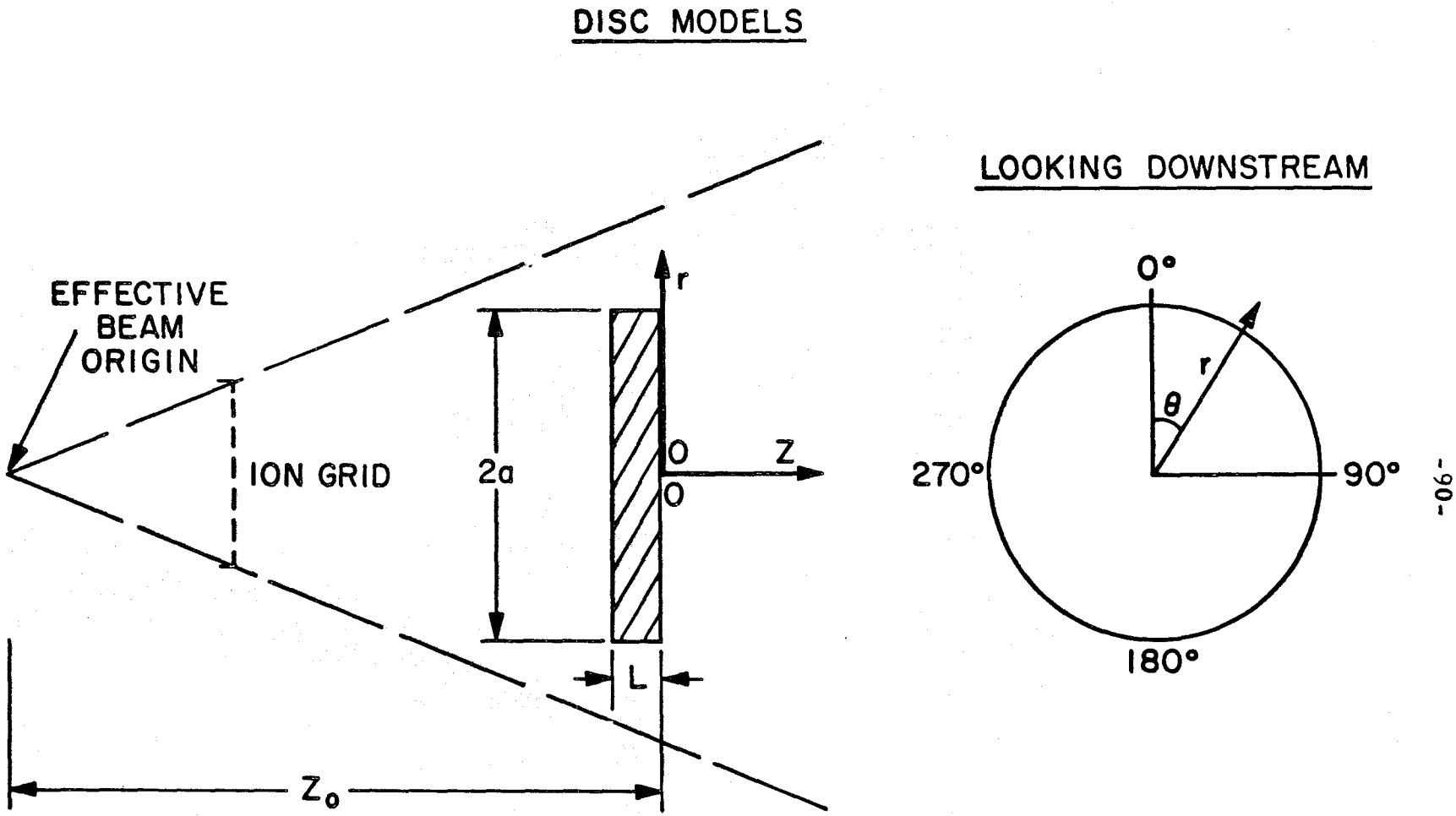

Figure 2.7 Disc Model and Coordinate System.

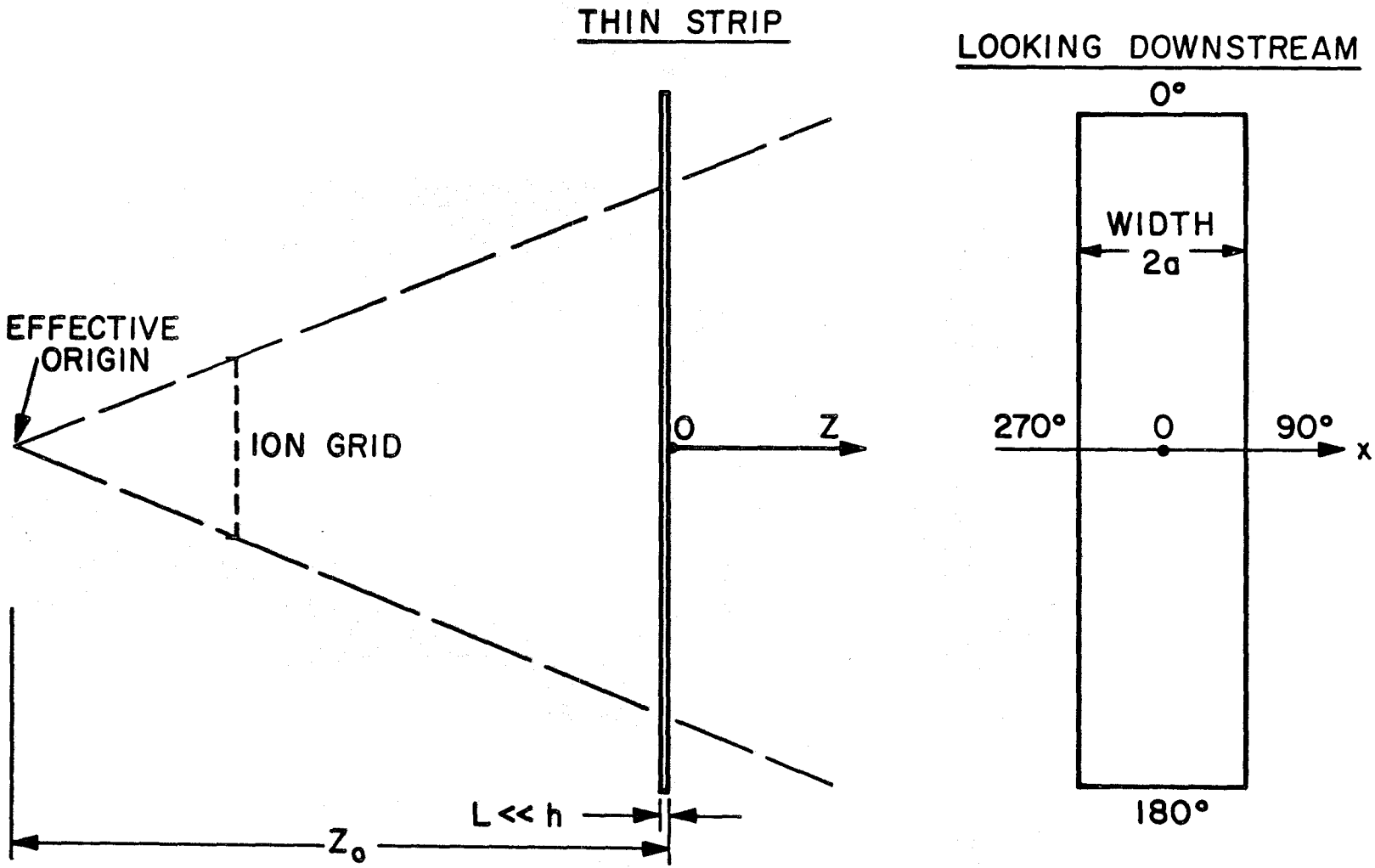

Figure 2.8 Strip Model and Coordinate System.

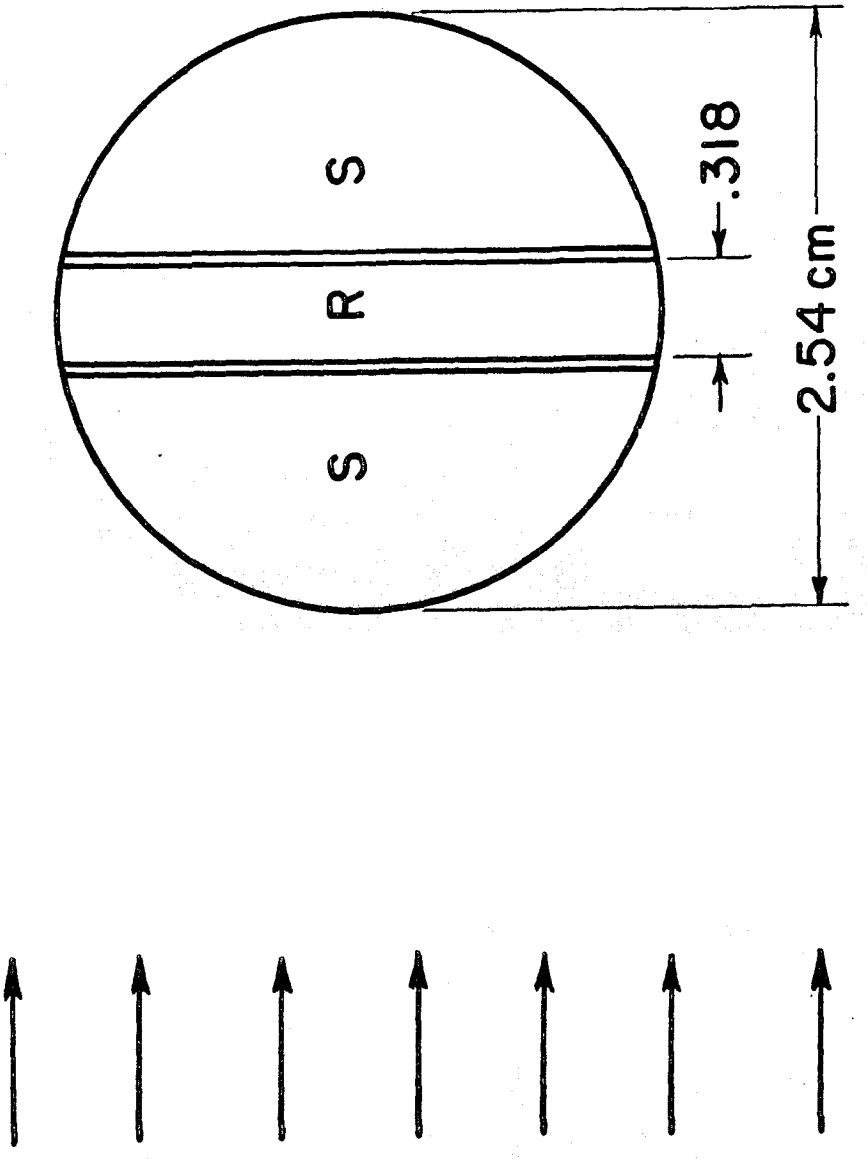

Figure 2.9 Spherical Model. Center Section Can be Biased Separately.

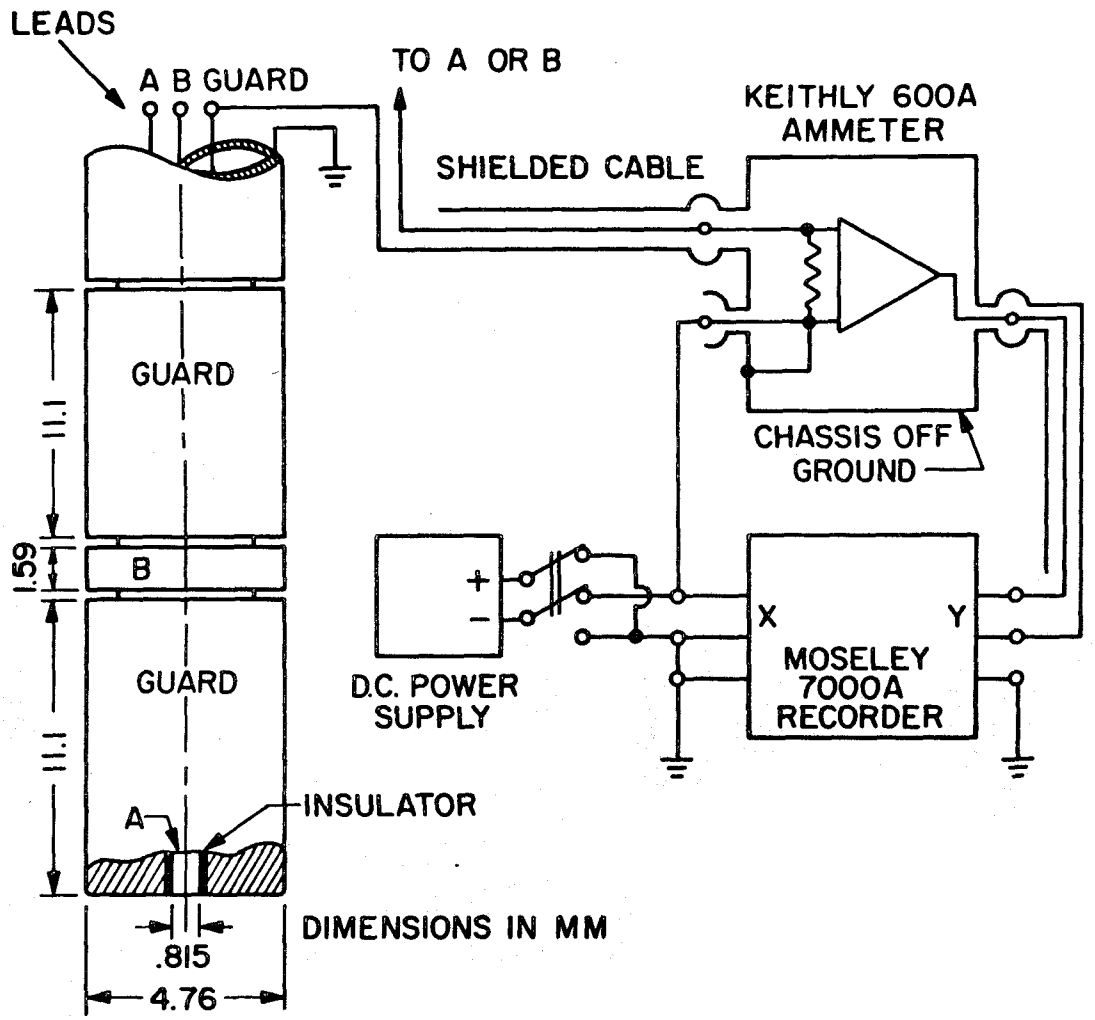

Figure 2.10 Guarded Langmuir Probe and Associated Circuit.

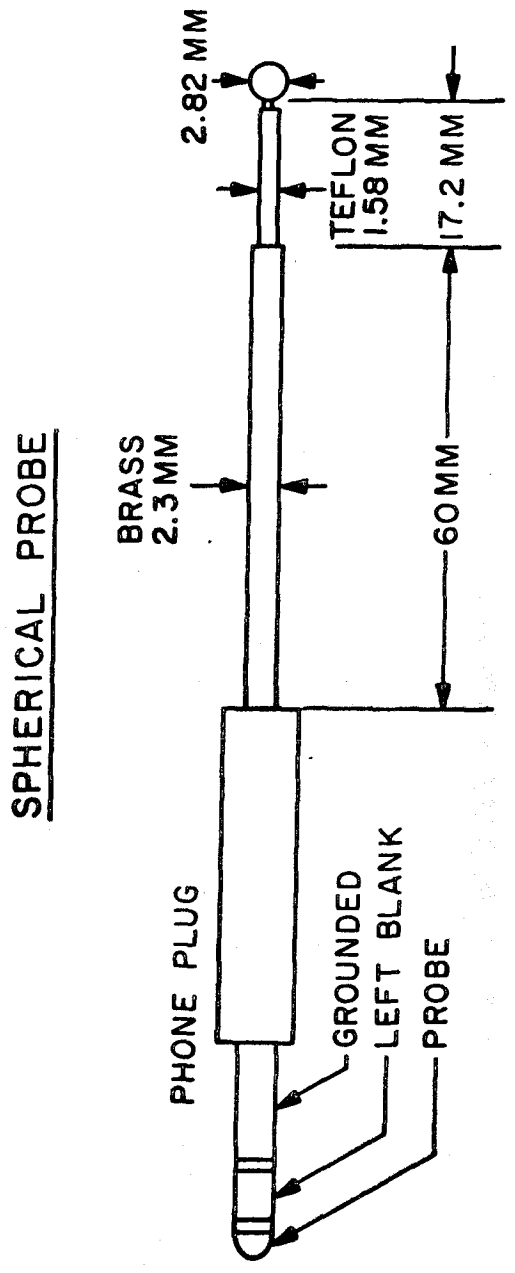

Figure 2.11 Spherical Langmuir Probe.

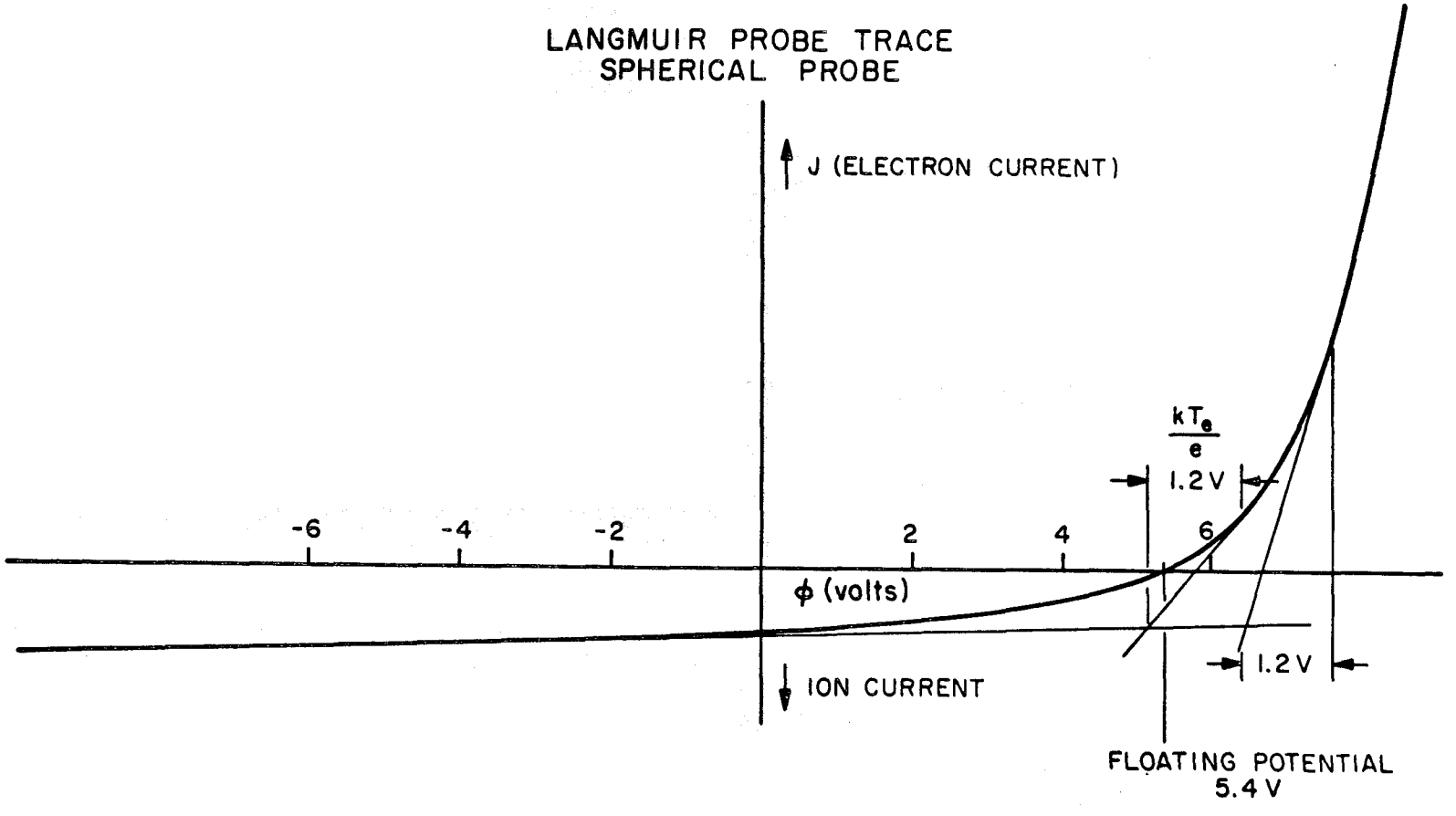

Figure 2.12 Langmuir Probe Curve Indicating Graphical Determination of Electron Temperature.

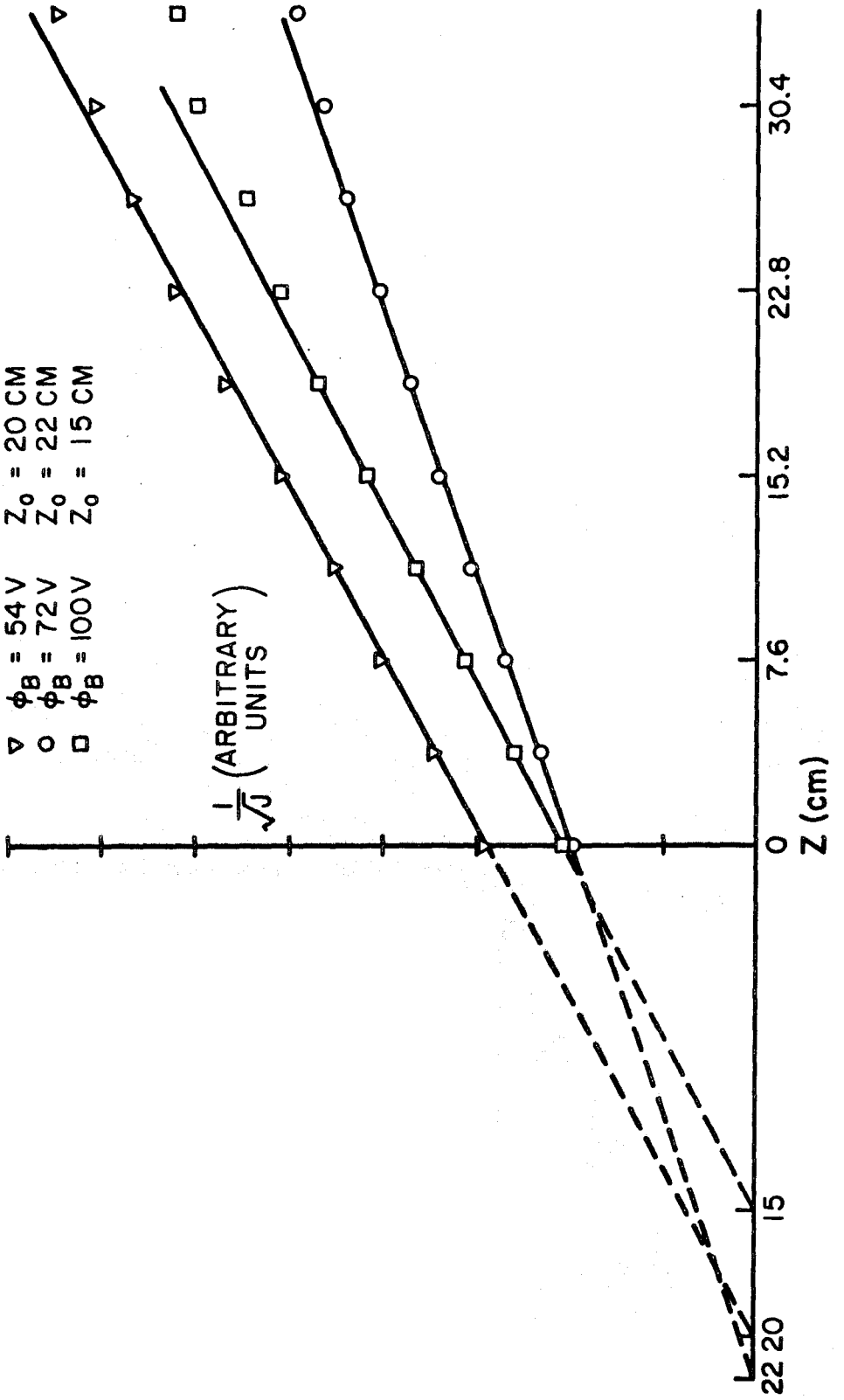

Figure 3.1 Determination of Effective Origin of Source Flow Like Beams for Low Mode

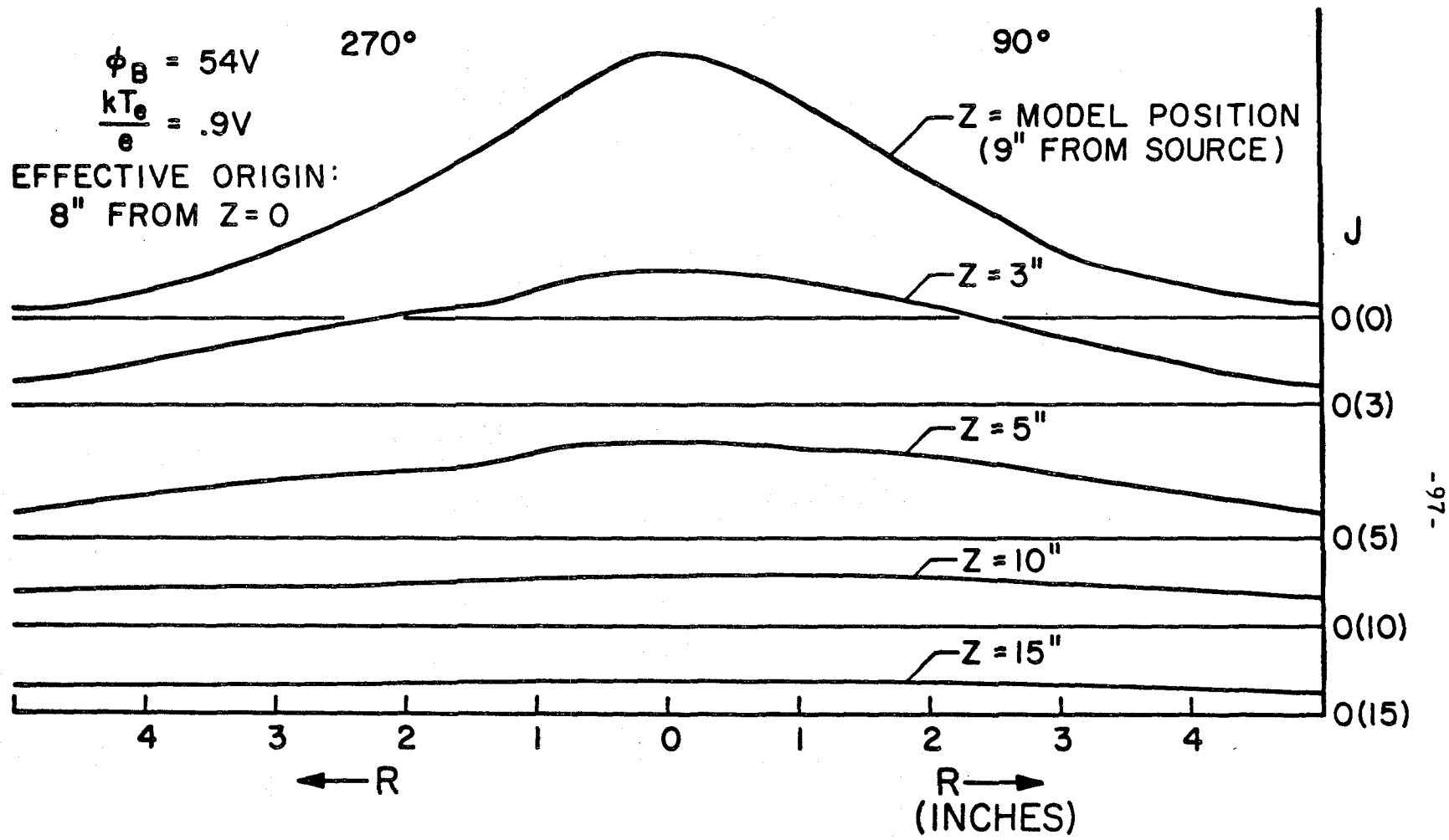

Figure 3.2 Cross Section of a 54V Beam for Various Distances from Source. Z = 0 is 8'' from Effective Origin, 9'' from Source Grid.

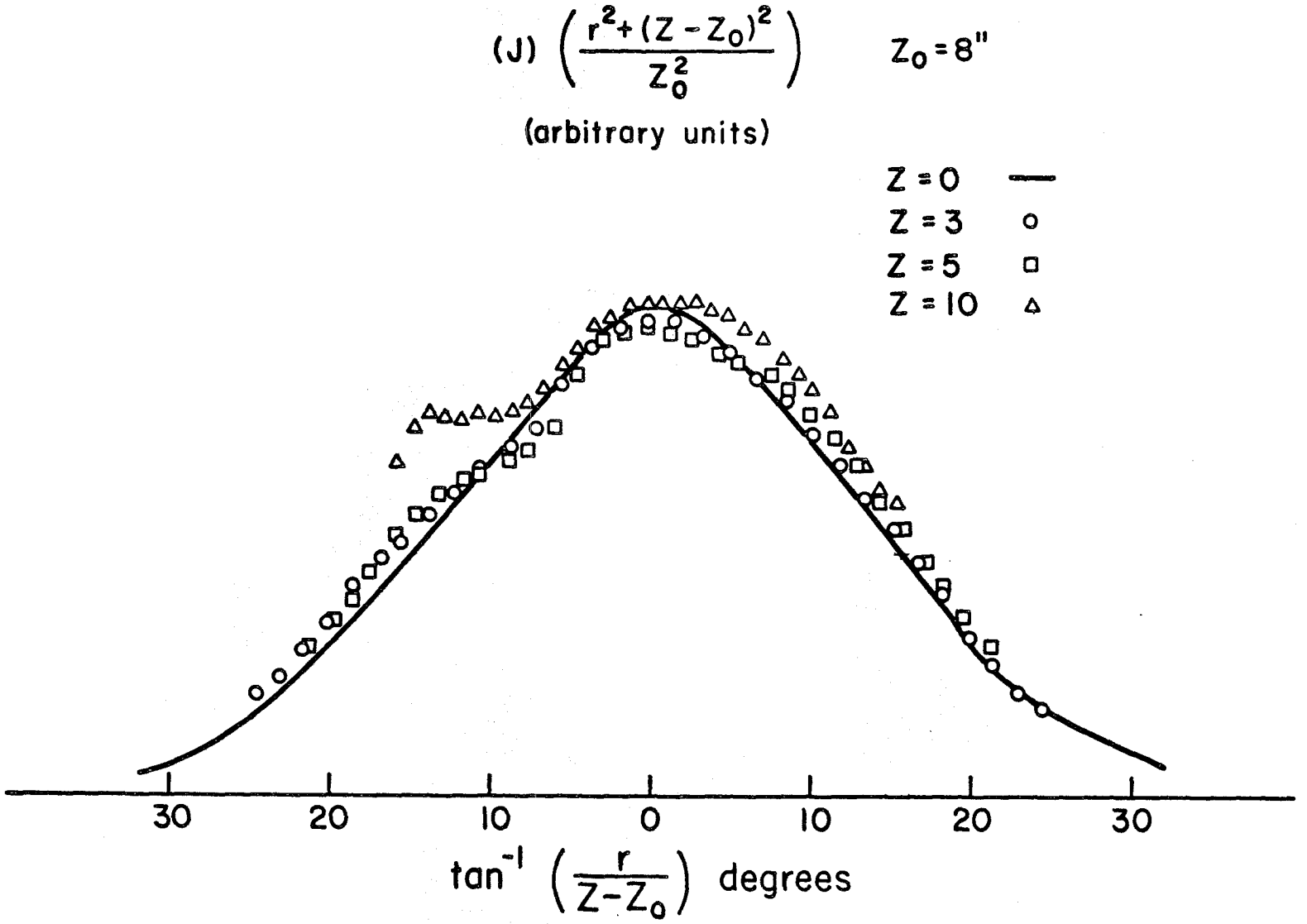

Figure 3. 3 Replot of Figure 3. 2 to Show Source Flow Nature of Beam.

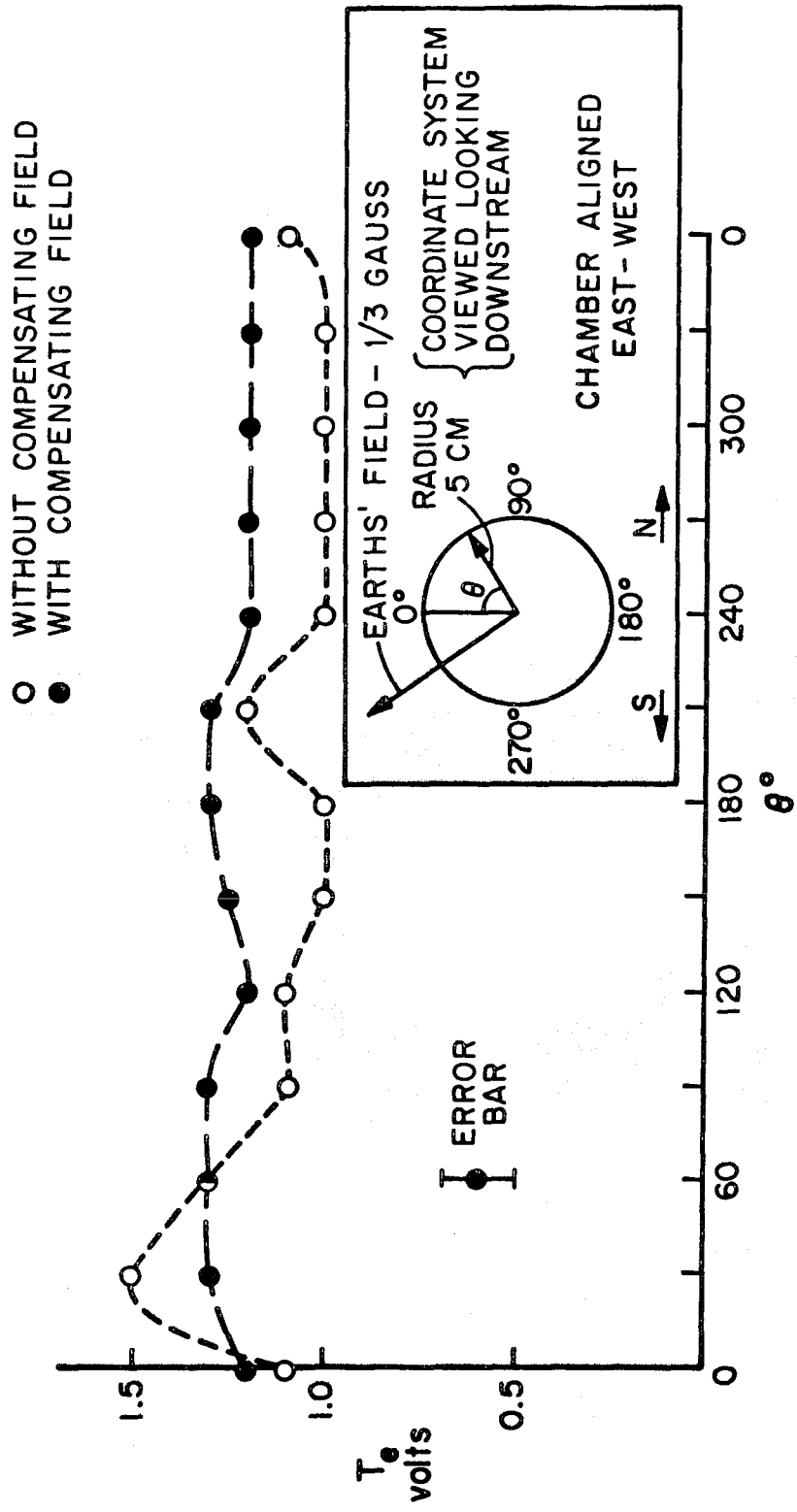

Figure 3.4 Effect of the Earth's Magnetic Field on Electron Temperature.

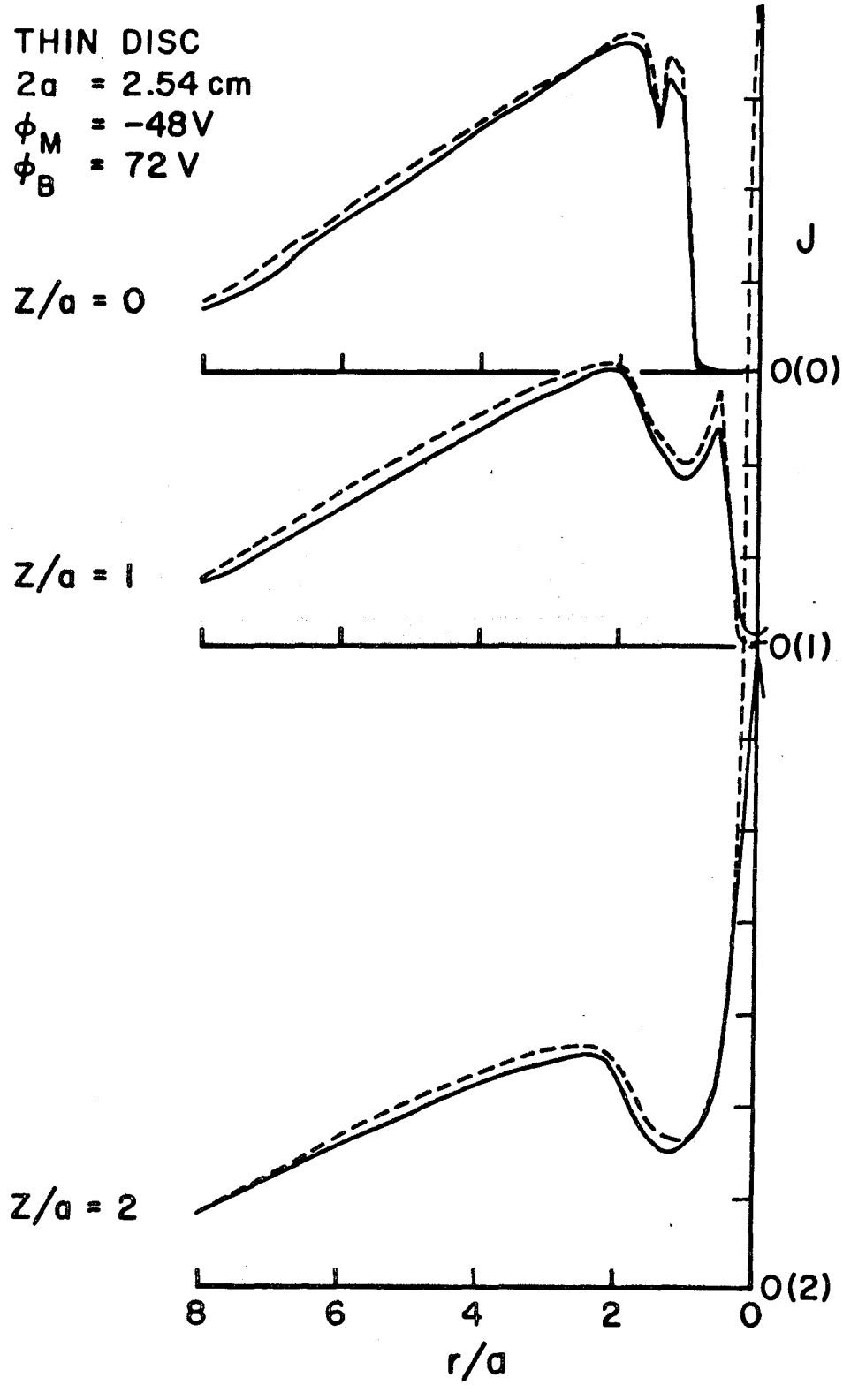

Figure 3.5 Comparison of Two Disc Wakes Taken Under Approximately the Same Conditions at Different Times.

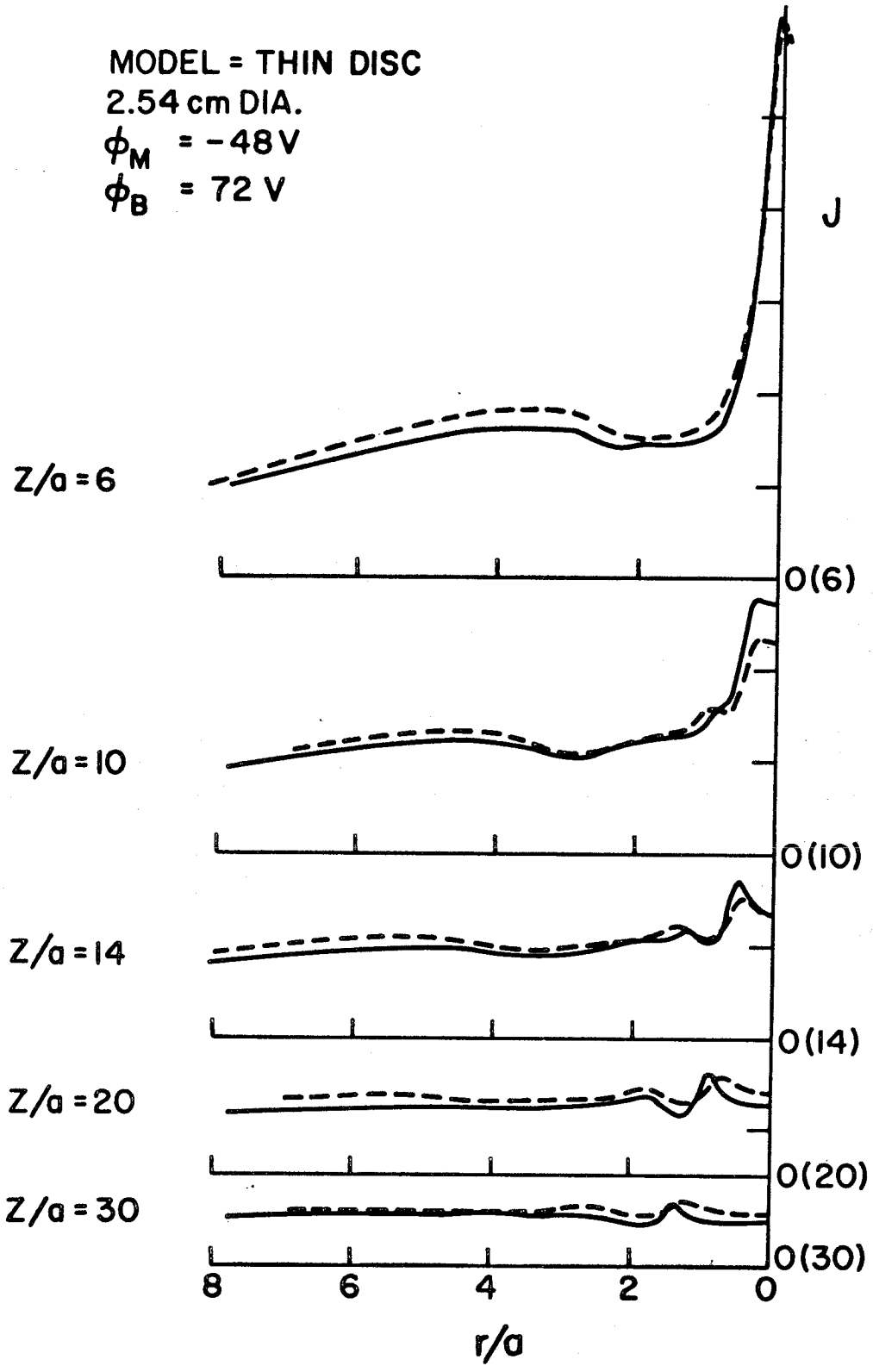

Figure 3.6 Continuation of Figure 3.5.

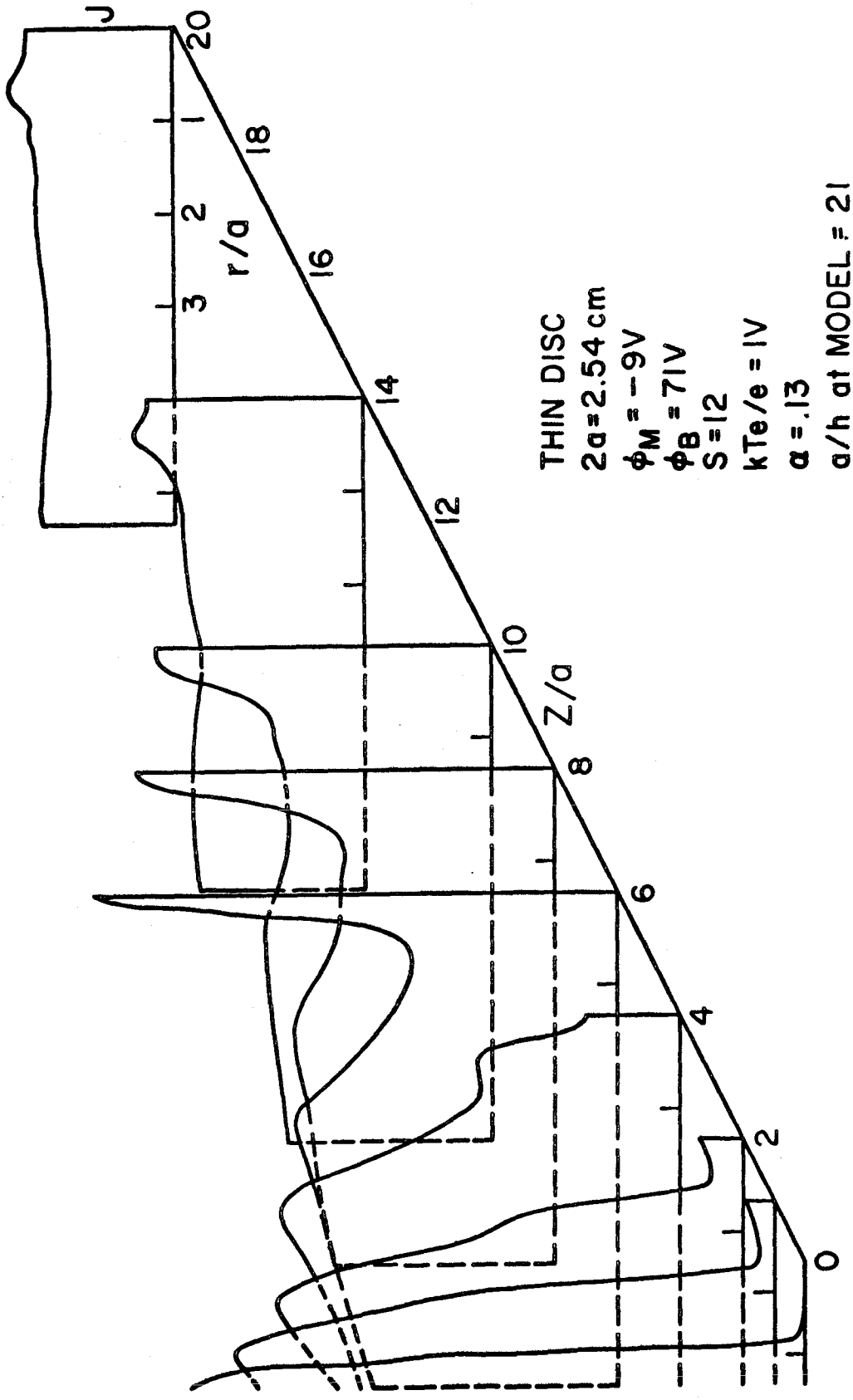

Figure 4.1 Cross Section of a Typical Wake.

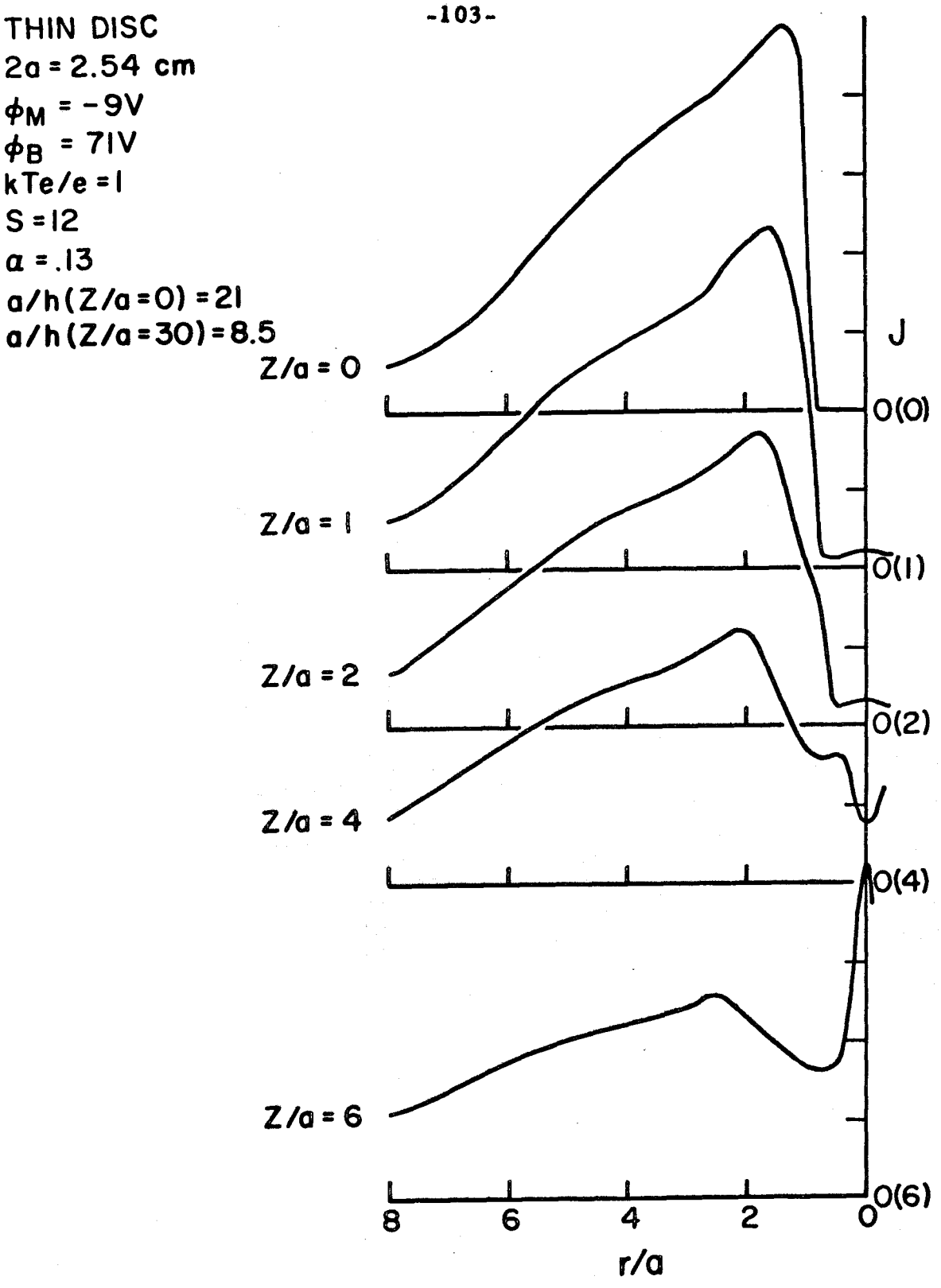

Figure 4.2 Near Wake of a Slightly Negative Thin Disc.

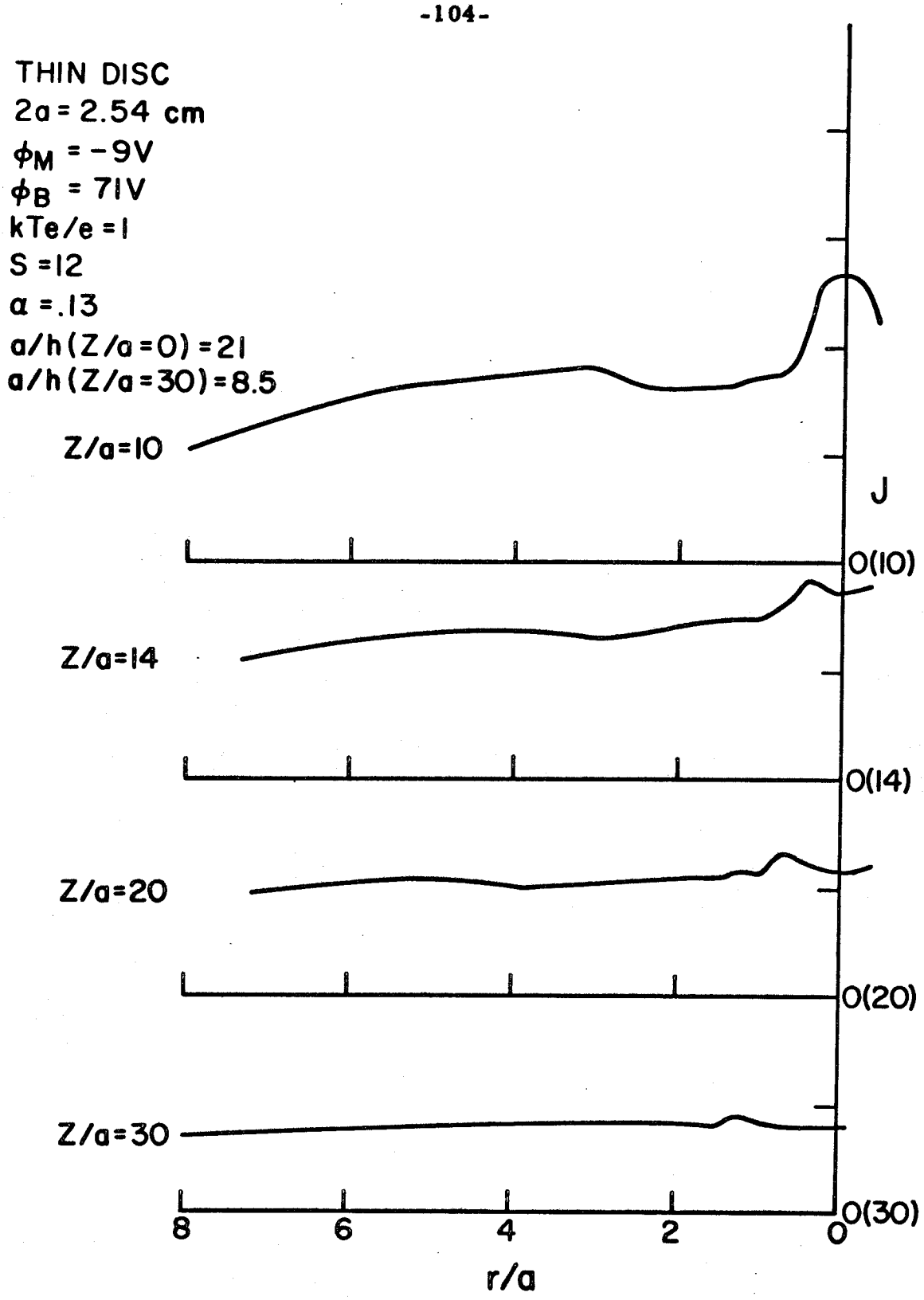

Figure 4.3 Far Wake of a Slightly Negative Thin Disc.

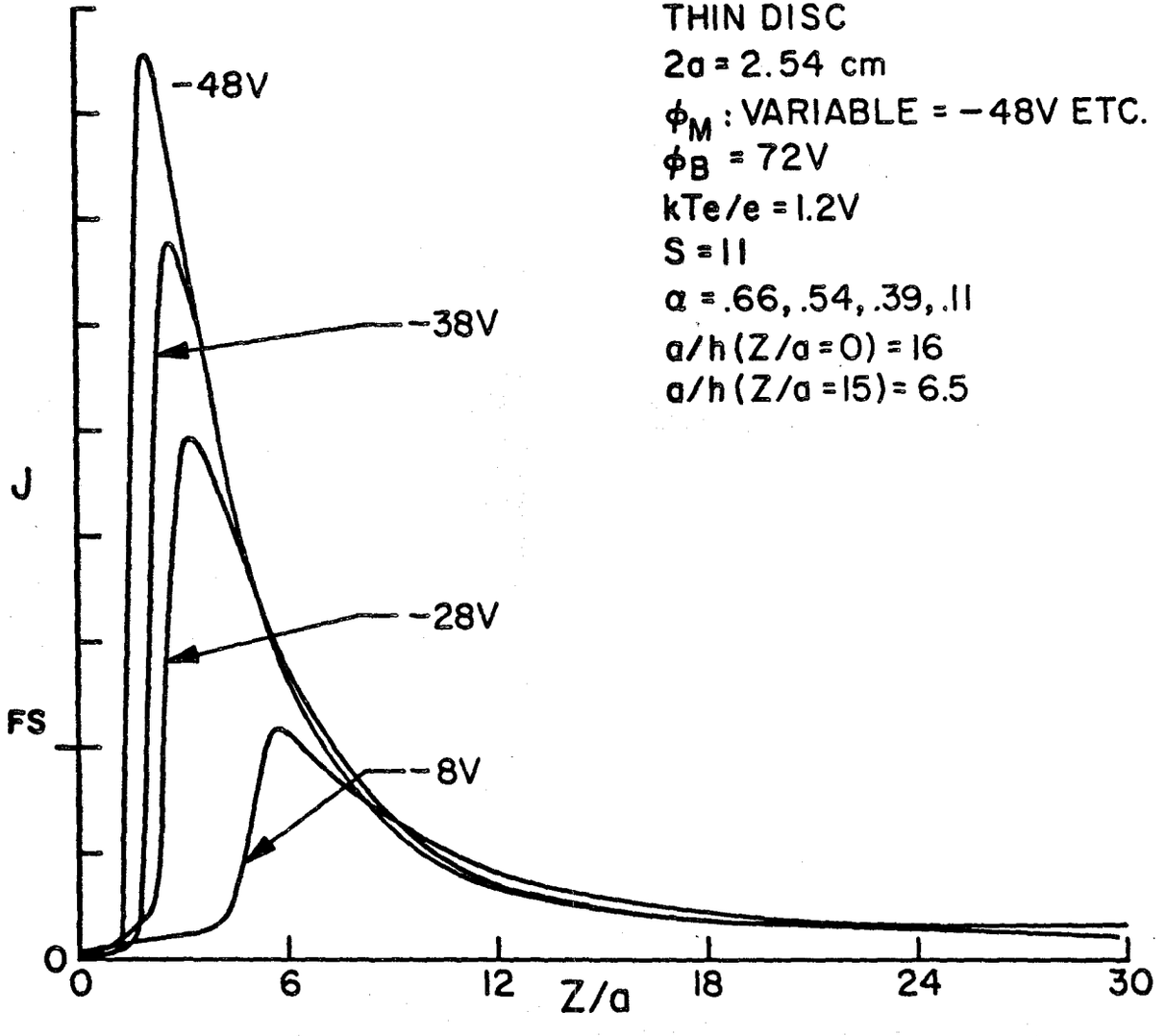

Figure 4.4 Effect of Model Potential on the Wake of a Thin Disc (Axial Traces).

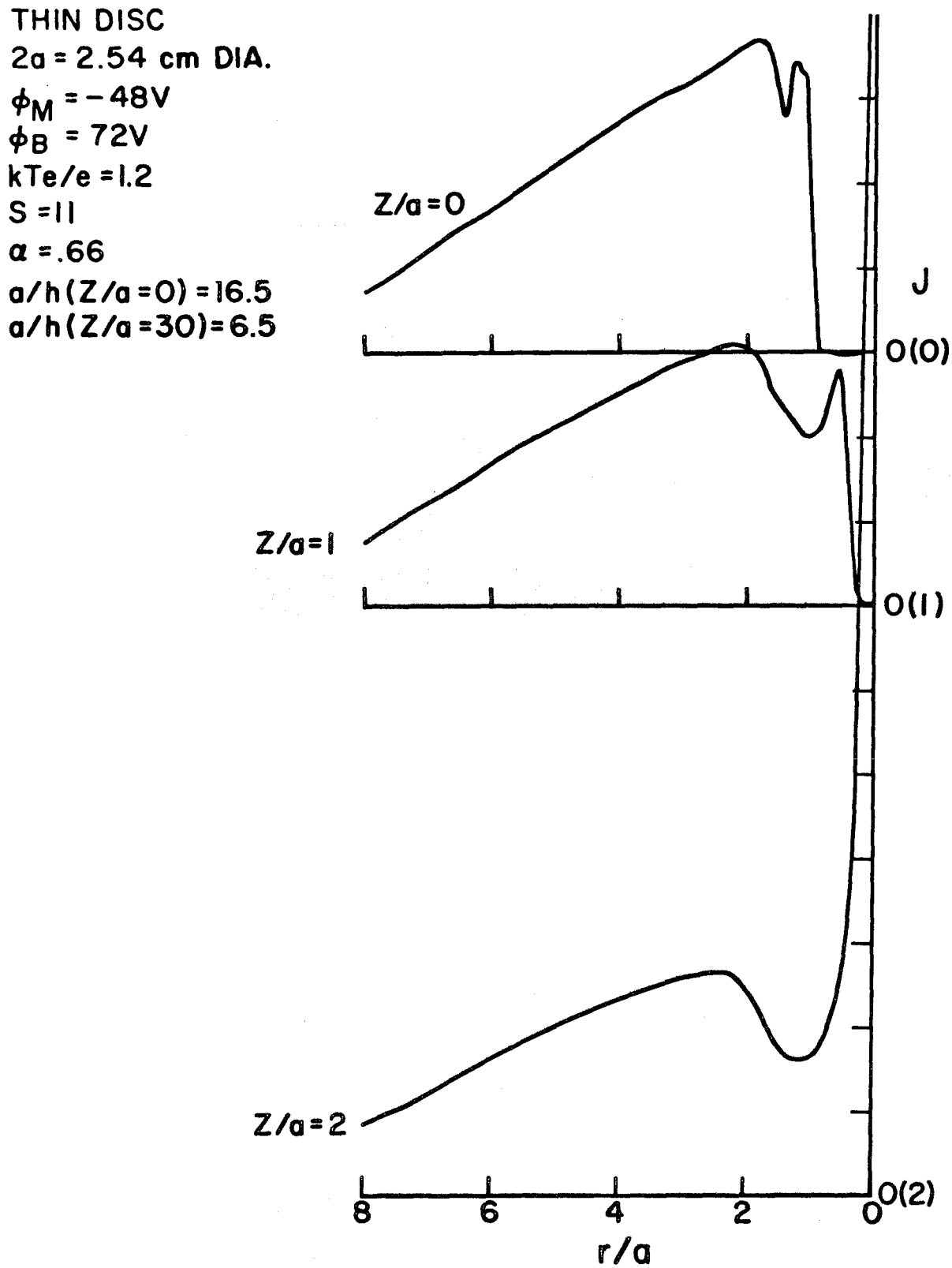

Figure 4.5 Near Wake of a Highly Negative Thin Disc.

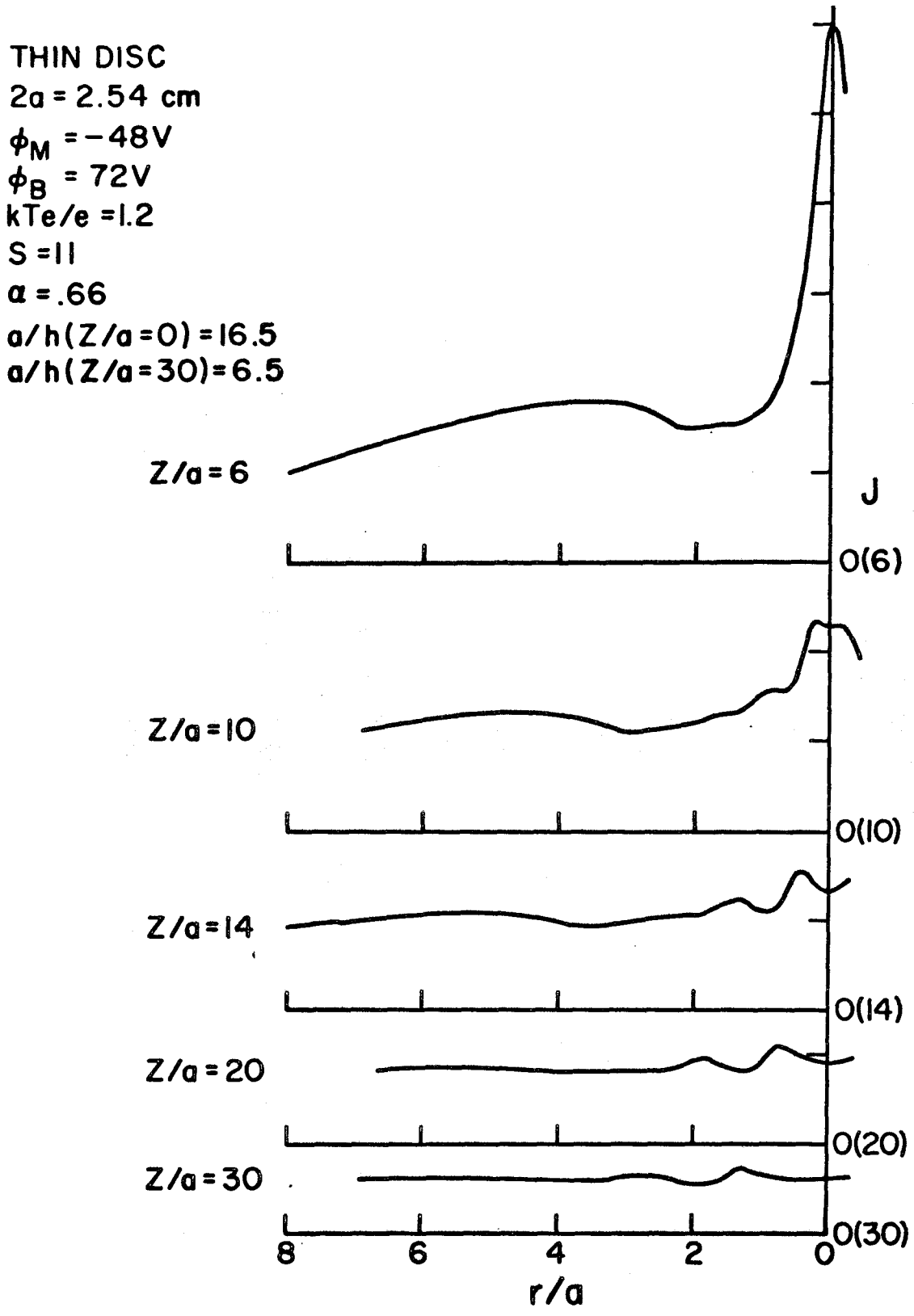

Figure 4.6 Far Wake of a Highly Negative Thin Disc.

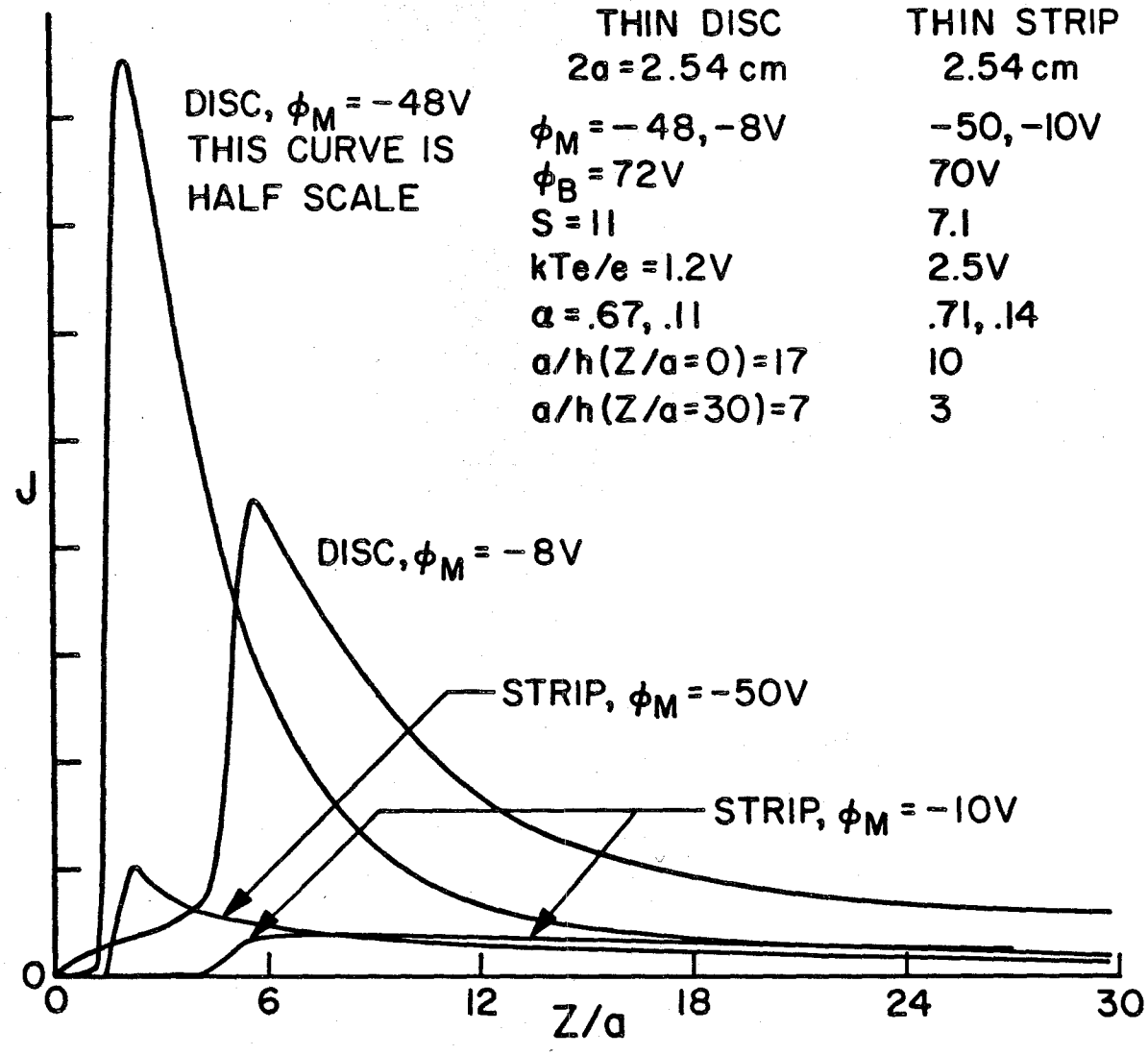

Figure 4.7 Comparison of Thin Disc and Strip Axial Traces.

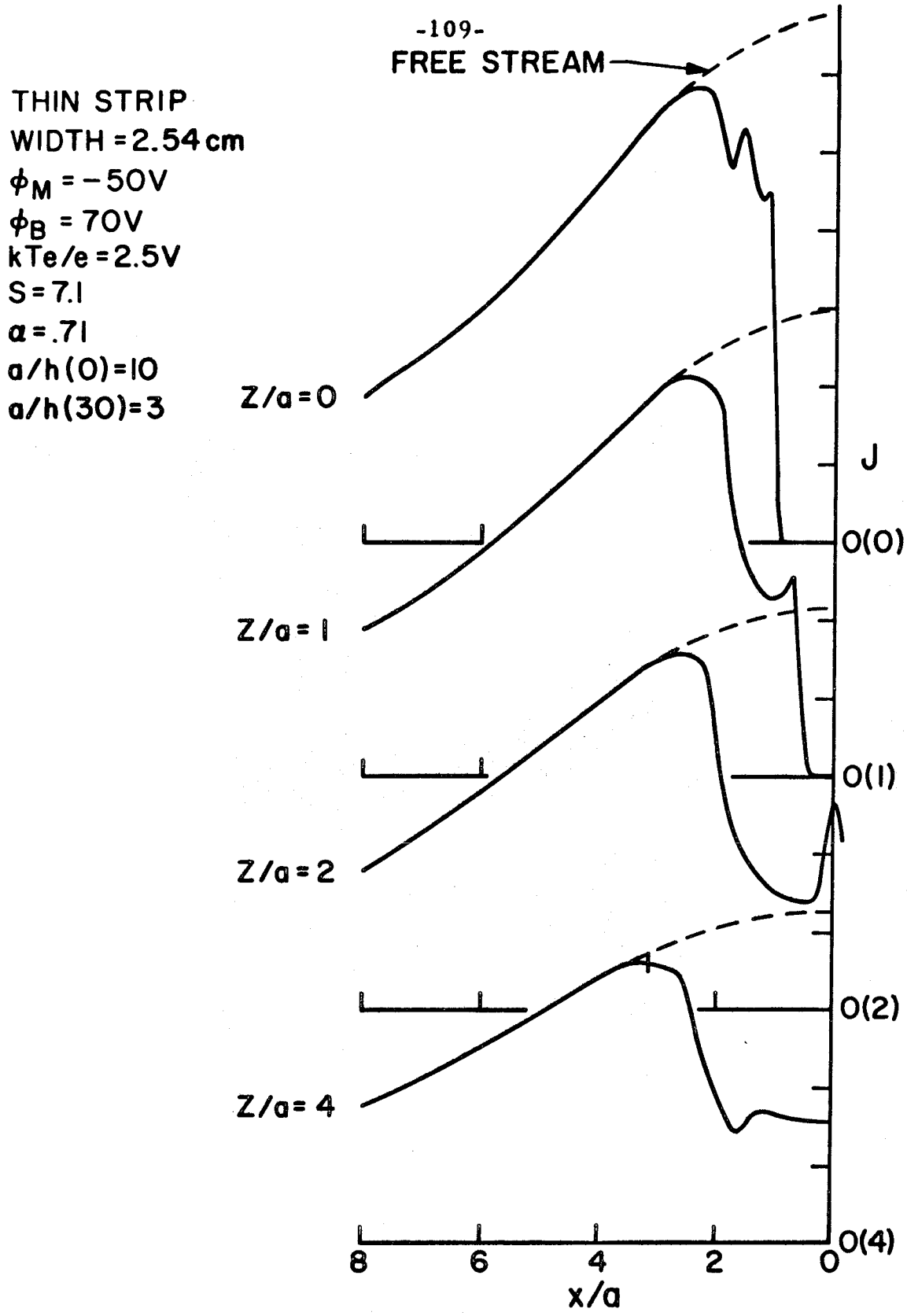

Figure 4.8 Near Wake of a Highly Negative Thin Strip.

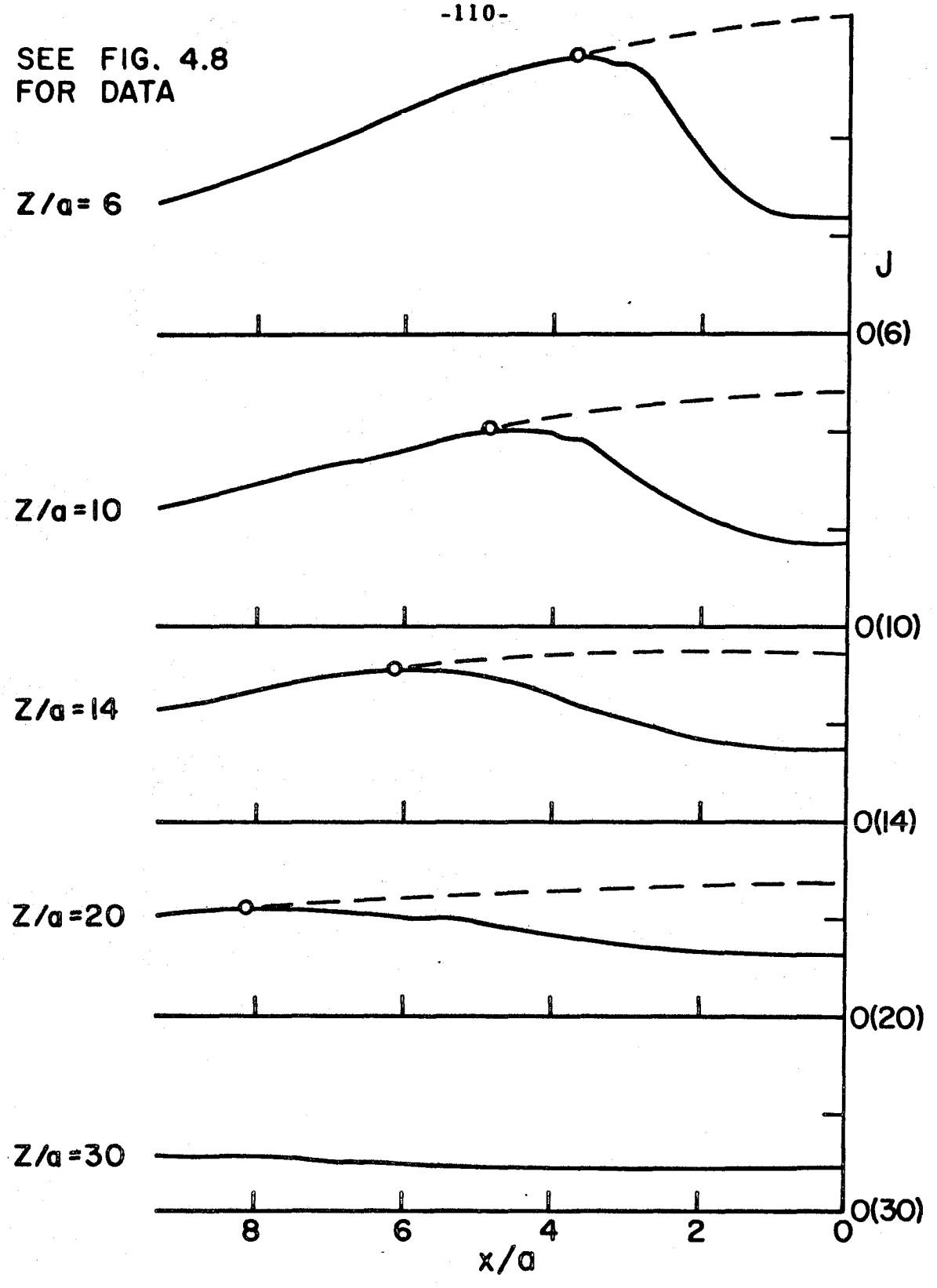

Figure 4. 9 Far Wake of a Highly Negative Thin Strip.

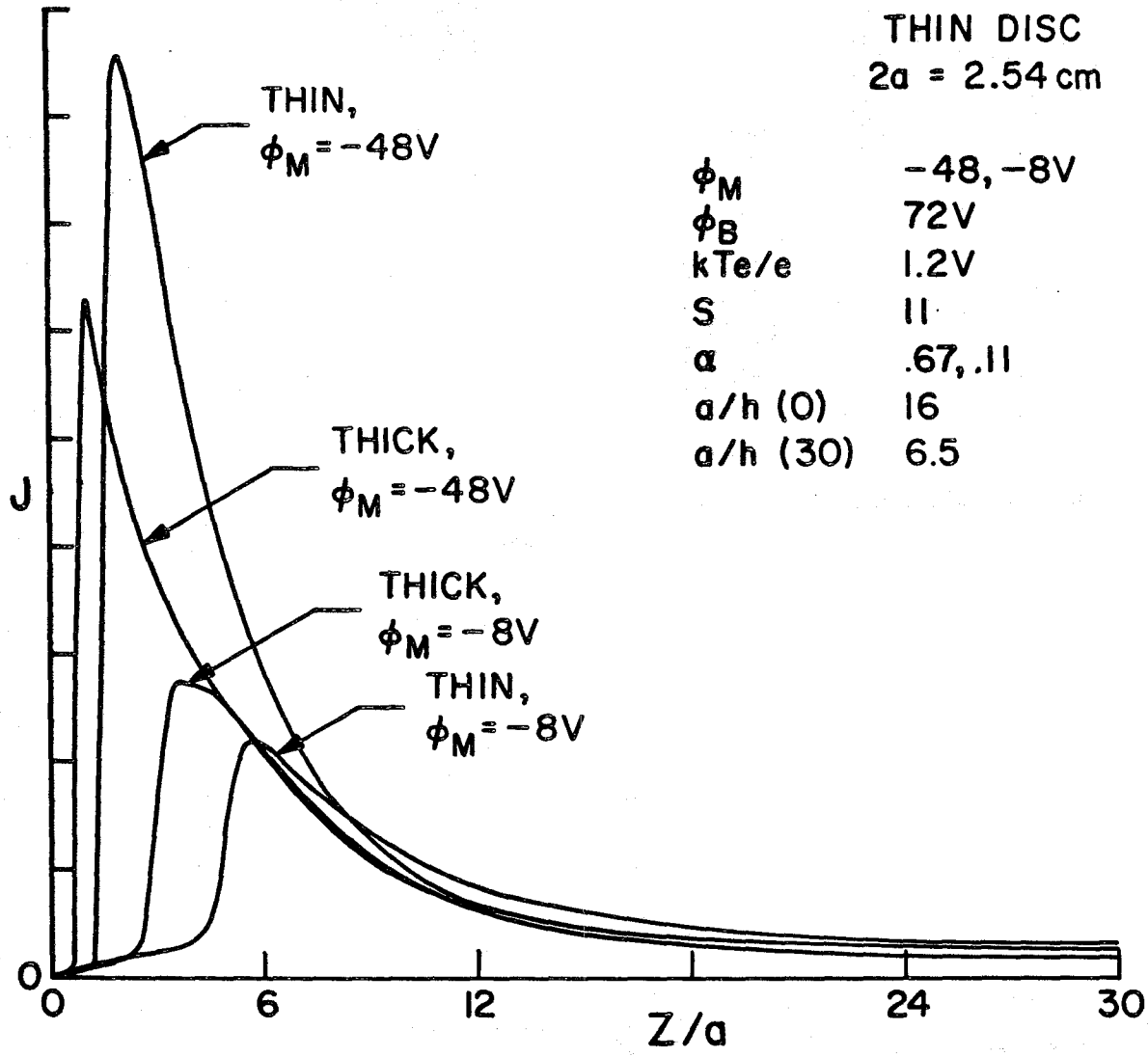

	THIN DISC 2a = 2.54 cm	THICK DISC 2a = 2.54 cm 1.27 cm THICK
ϕ_M	−48, −8V	−48, −8V
ϕ_B	72V	72V
kTe/e	1.2V	1.7V
S	11	9
α	.67, .11	.67, .11
a/h (0)	16	13
a/h (30)	6.5	4.5

Figure 4.10 Comparison of Thick and Thin Disc Axial Traces.

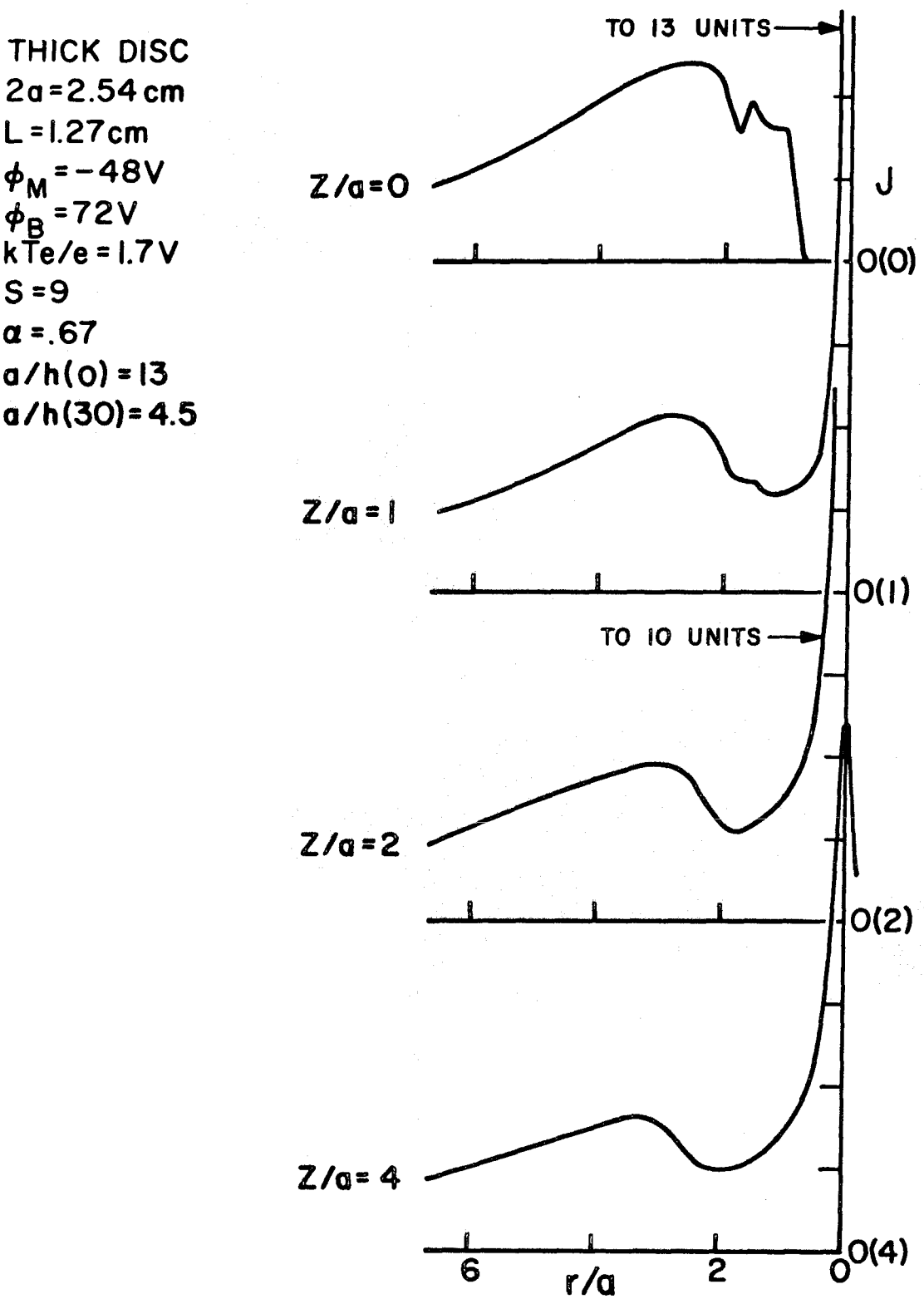

Figure 4.11 Near Wake of a Highly Negative Thick Disc.

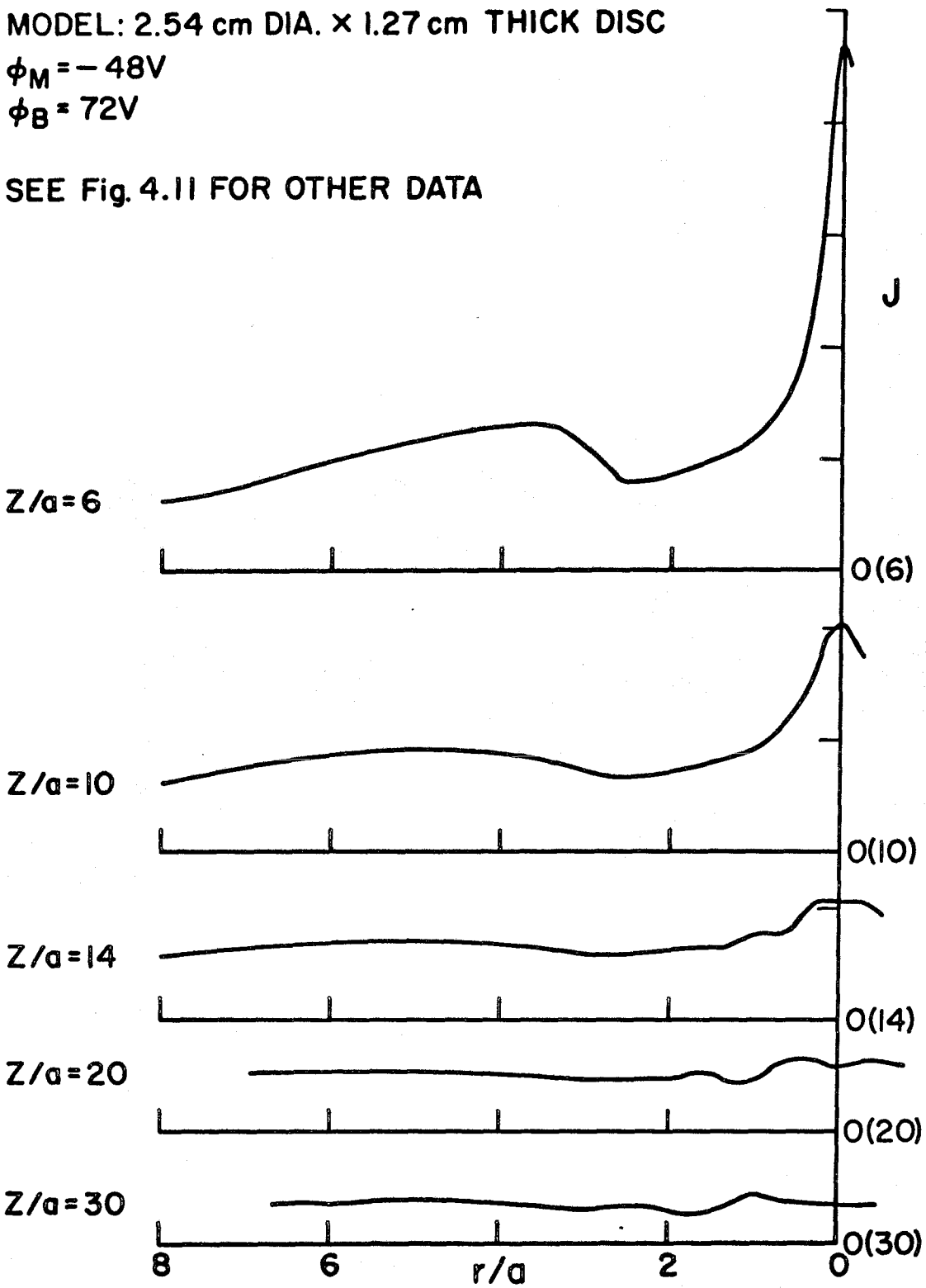

Figure 4.12 Far Wake of a Highly Negative Thick Disc.

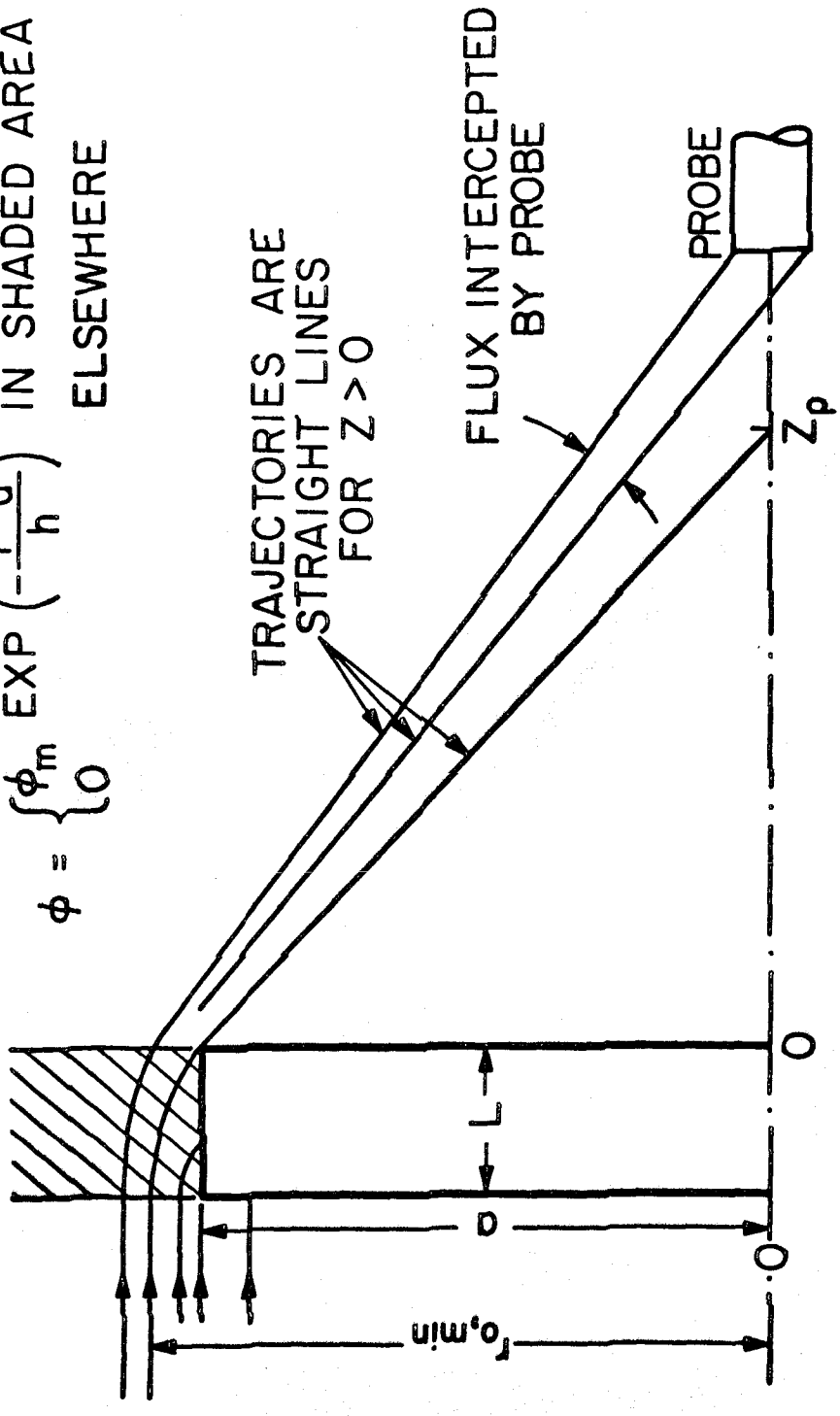

Figure 4.13 Schematic of Ion Trajectories in the Near Wake as Assumed for Theory.

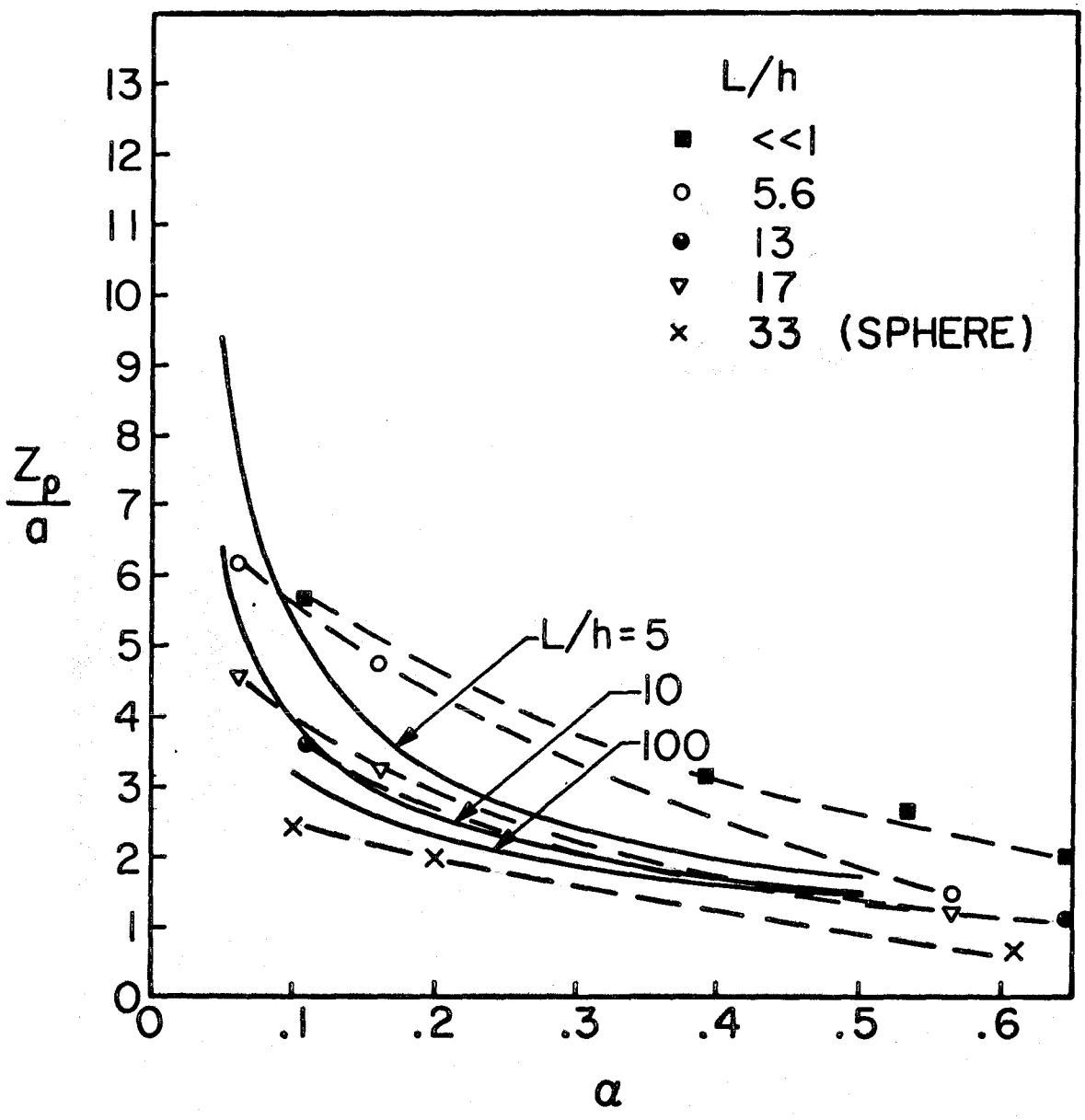

Figure 4.14 Comparison of Theoretical and Actual Peak Positions.

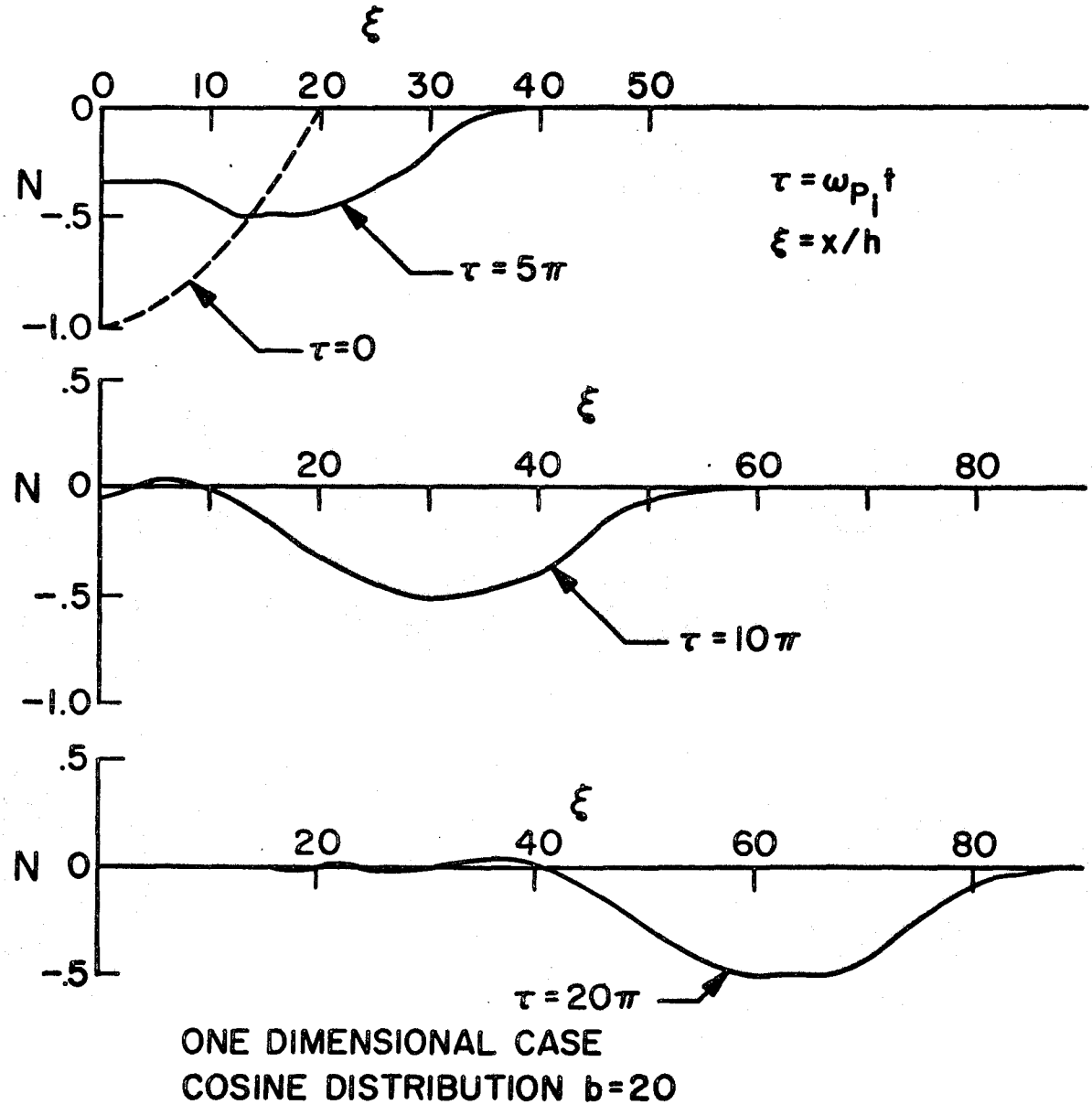

Figure 5.1 Theoretical Development with Time of Wide One-Dimensional Disturbance (2b/h = 40).

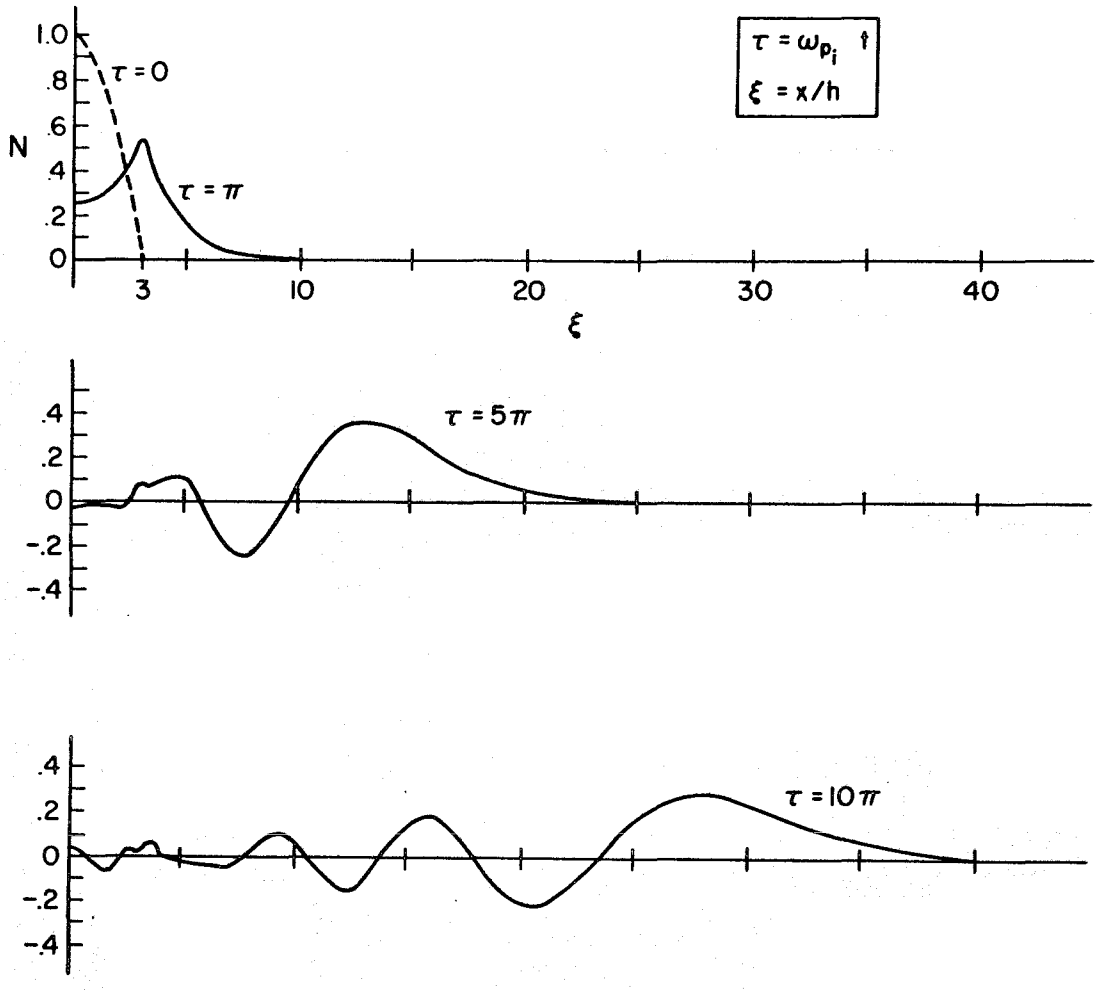

ONE DIMENSIONAL CASE
COSINE INITIAL DISTRIBUTION (b = 3)

Figure 5.2 Development of a One-Dimensional Disturbance (2b/h = 6).

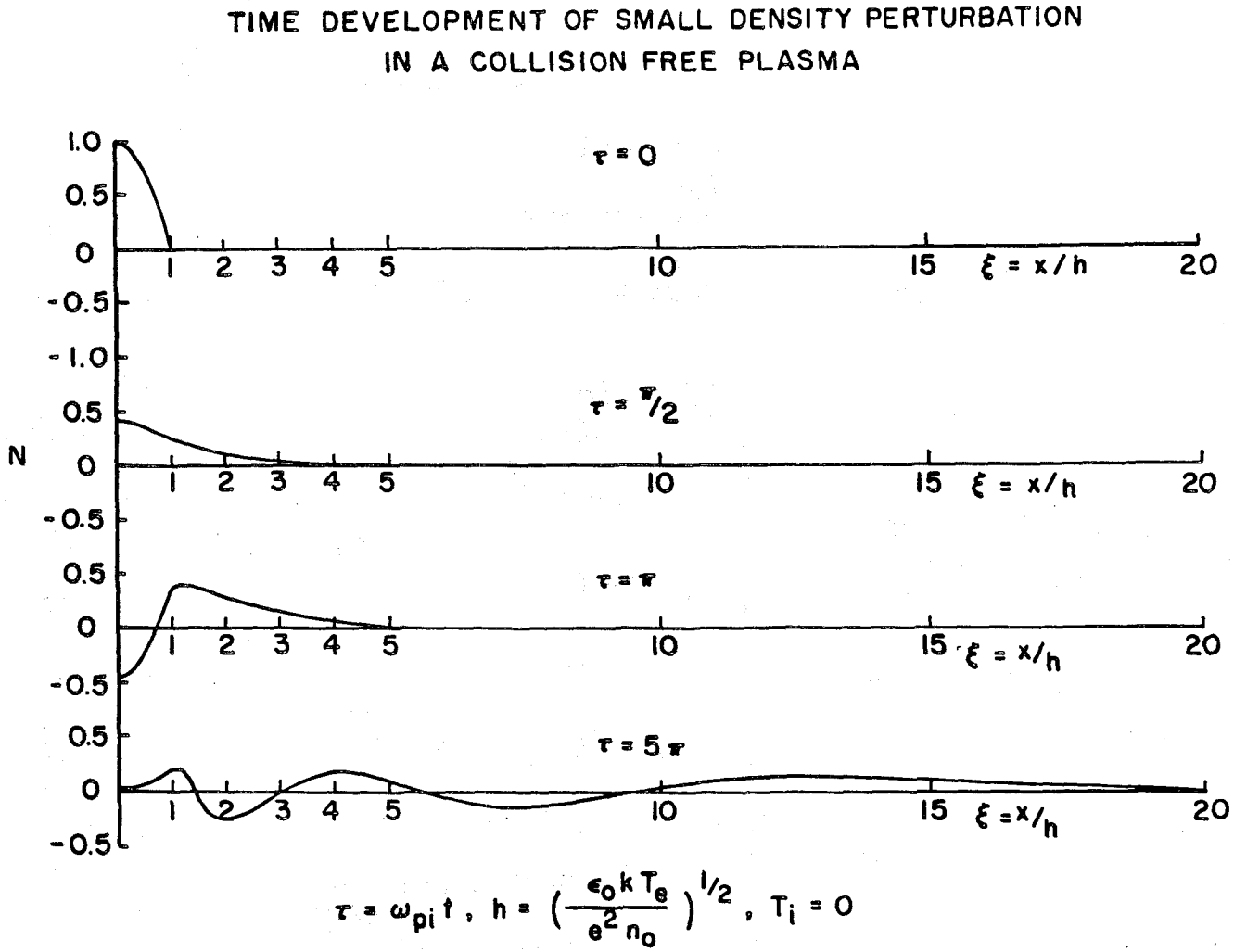

Figure 5.3 Development of a Narrow Density Disturbance in a One-Dimensional Plasma (2b/h = 2).

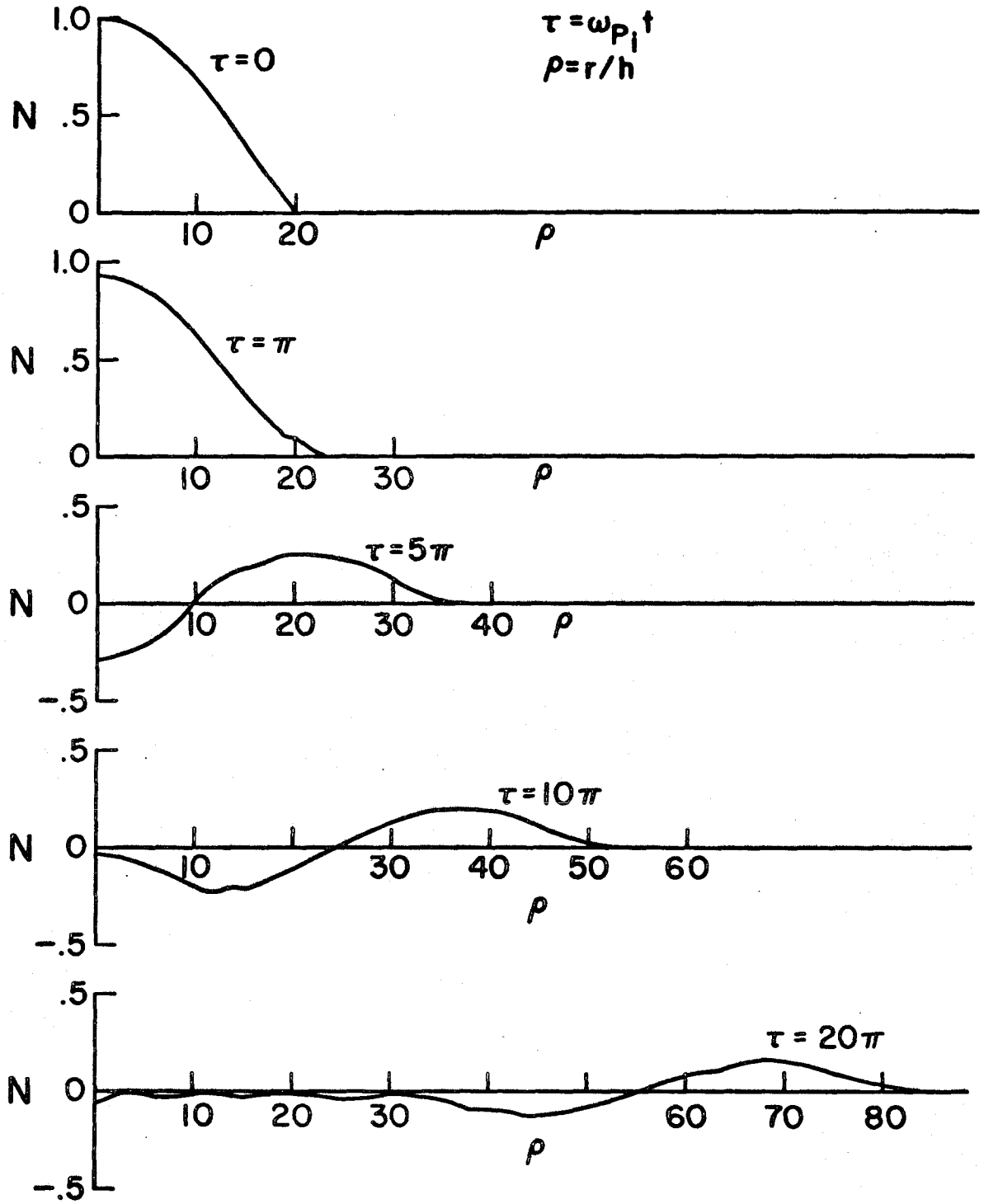

CYLINDRICAL CASE
J_0 DISTRIBUTION, b = 20

Figure 5.4 Development of a Wide Cylindrical Density Disturbance (2b/h = 40).

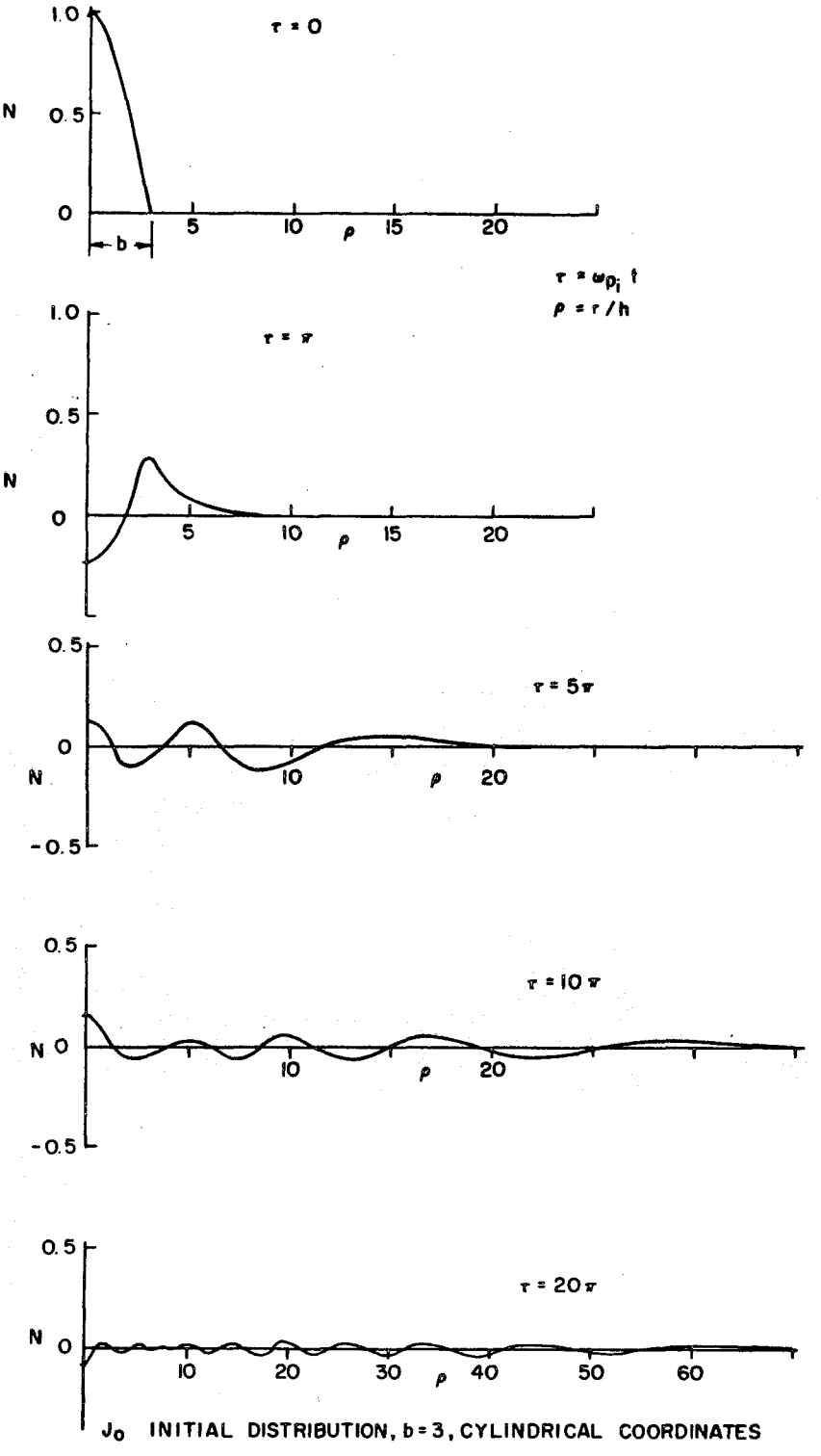

Figure 5.5 Development of a Cylindrical Density Disturbance (2b/h = 6).

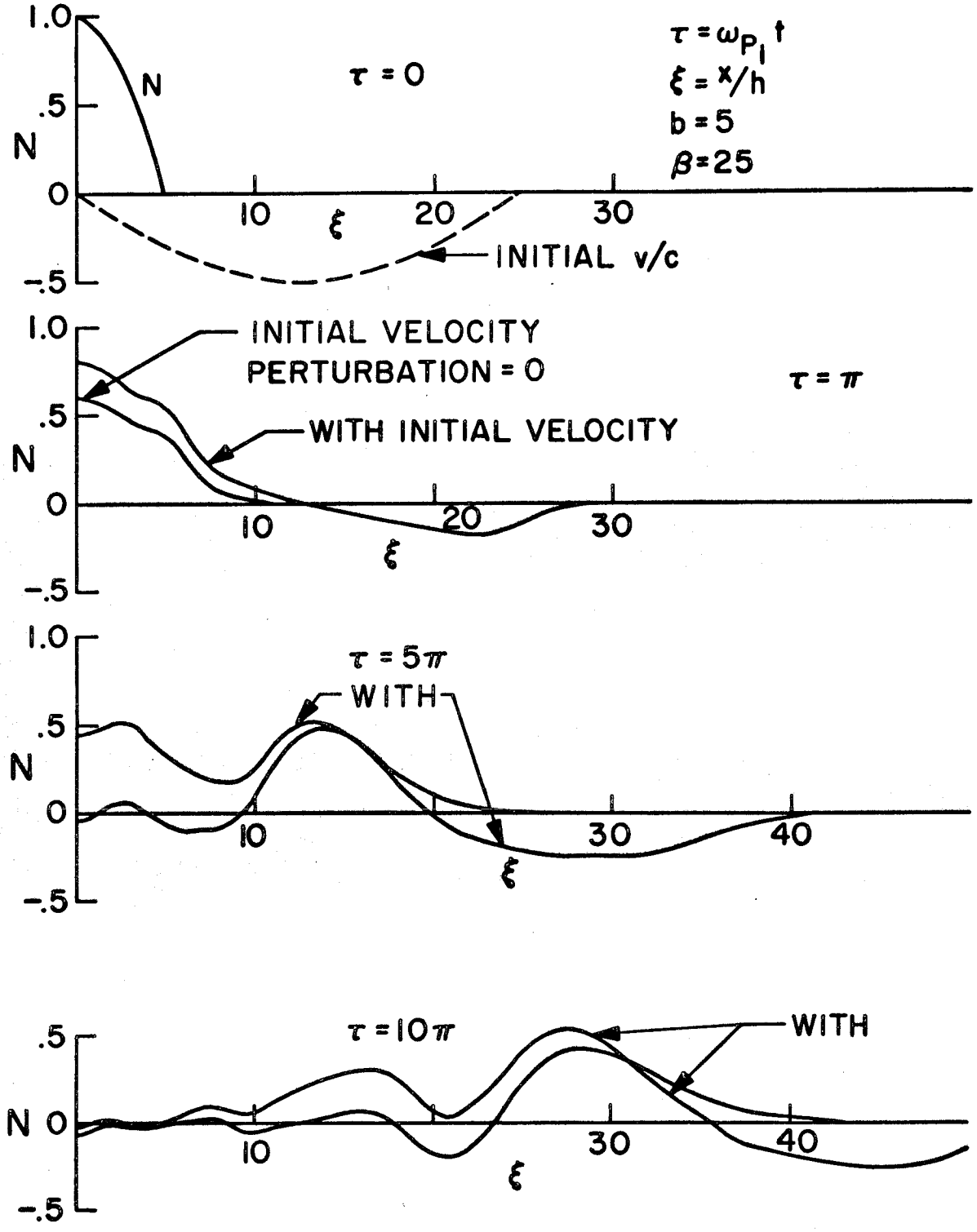

ONE DIMENSIONAL COSINE INITIAL DENSITY DISTRIBUTION, SINE VELOCITY DISTRIBUTION

Figure 5.6 Development of a Cylindrical Density Disturbance with Zero and Non-zero Initial Velocity Perturbation.

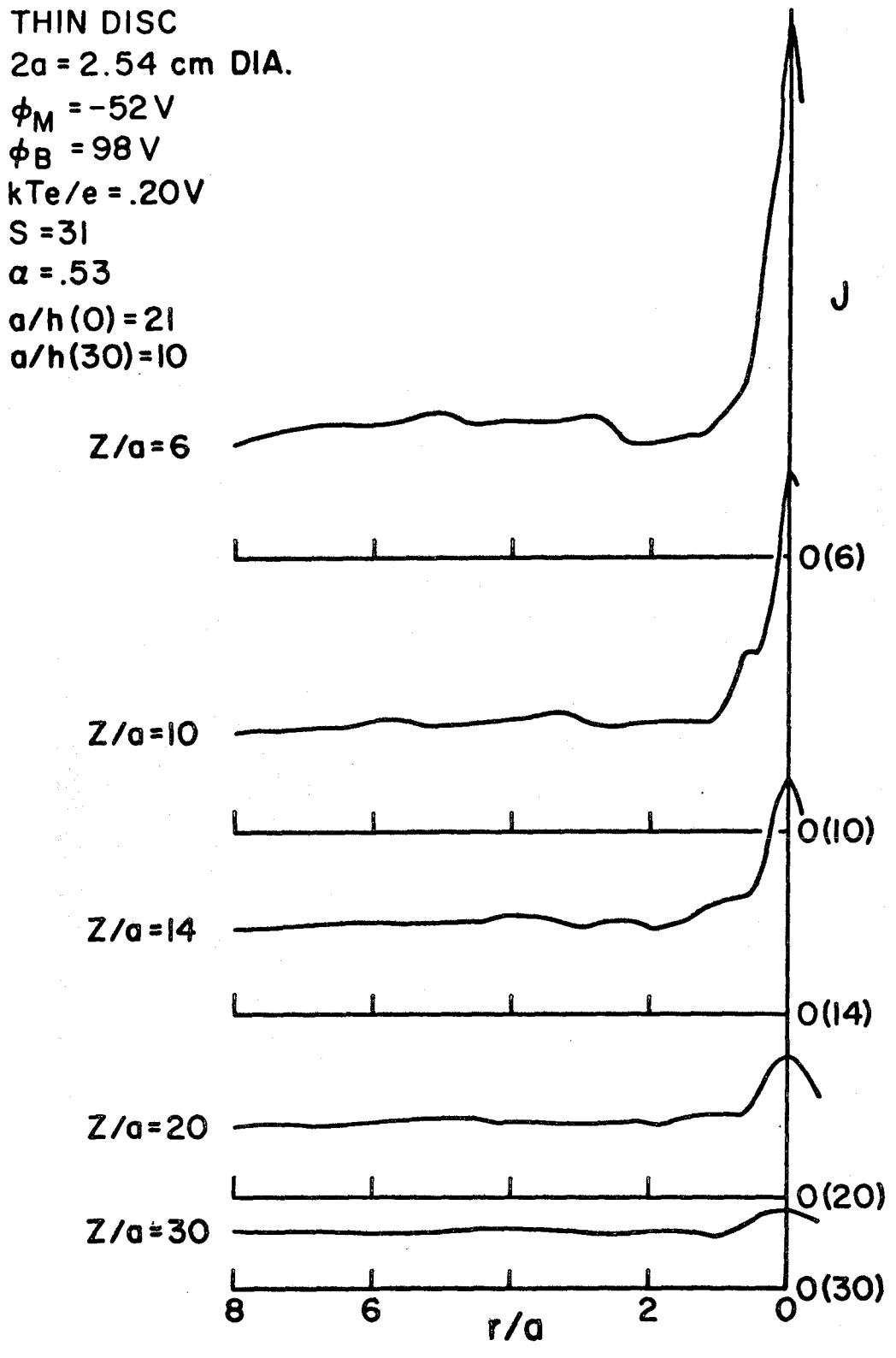

Figure 5.7 Far Wake of a Highly Negative Thin Disc for S = 31.

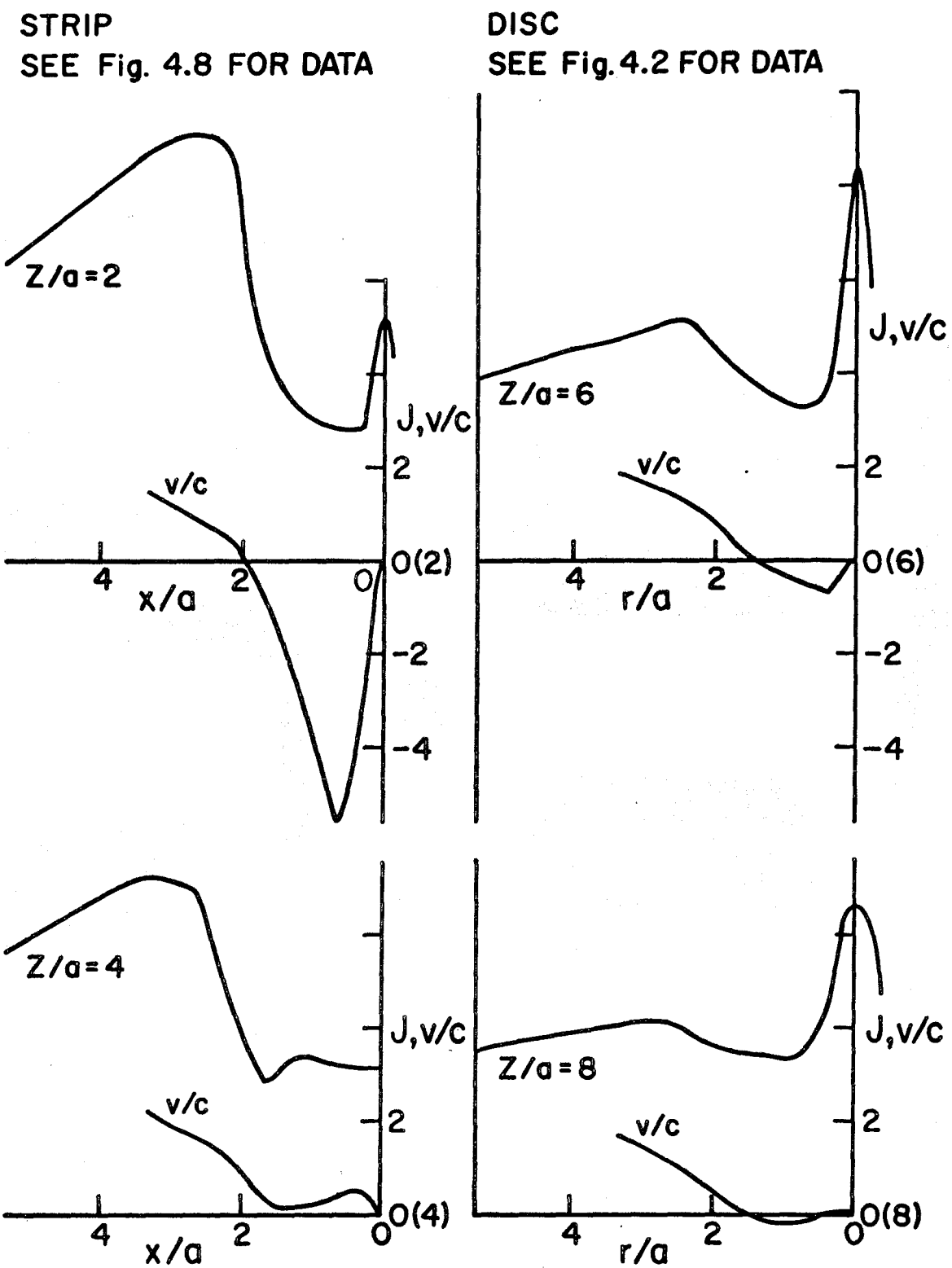

Figure 5.8 Radial Ion Velocity and Axial Flux Profiles for the First Far Wake Traces of a Thin Disc and a Thin Strip.

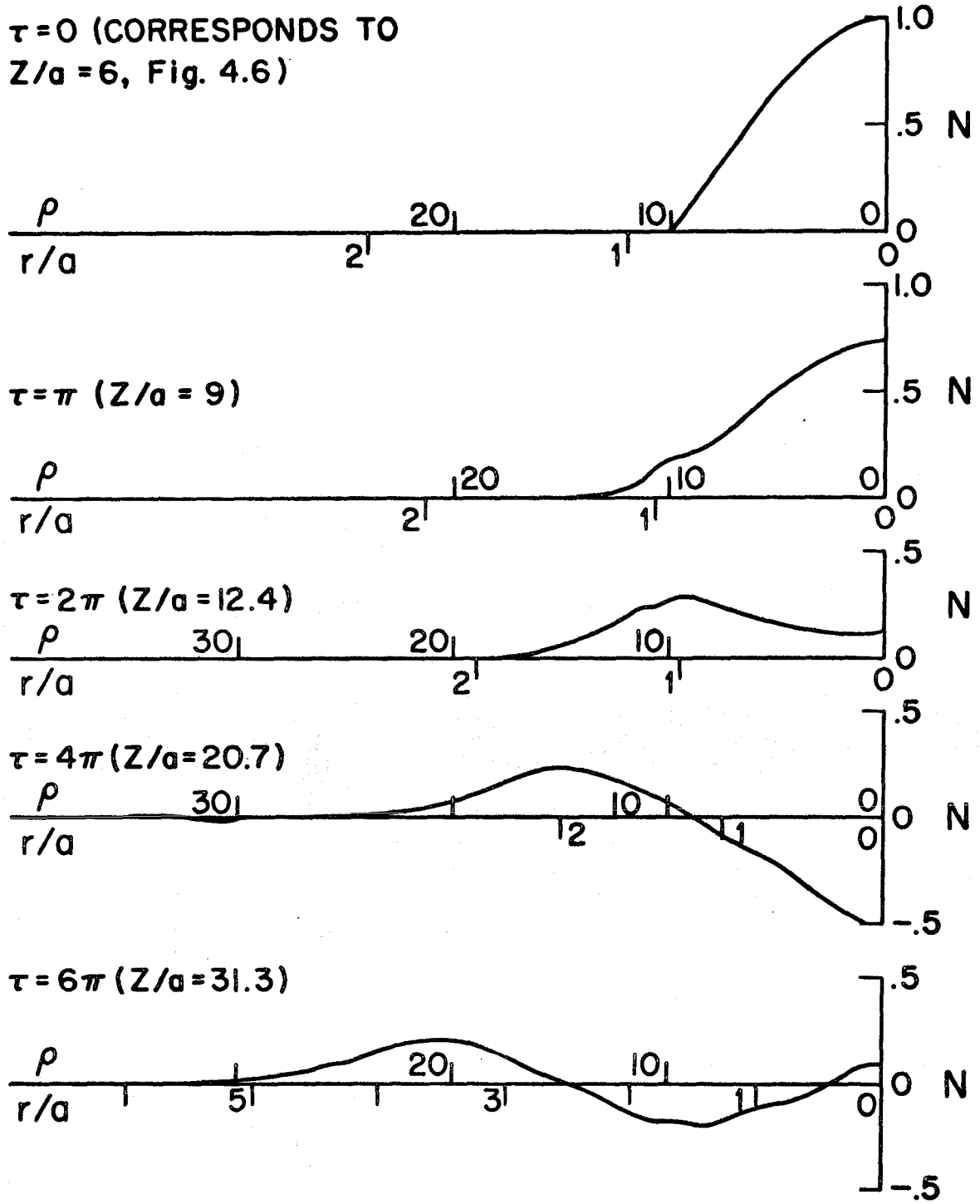

Figure 5.9 Theoretical Development of the Far Wake for an Initial Condition Similar to the Z/a = 6 Flux Profile of Figure 4.6. Radial velocities are assumed to be zero at $\tau = 0$.

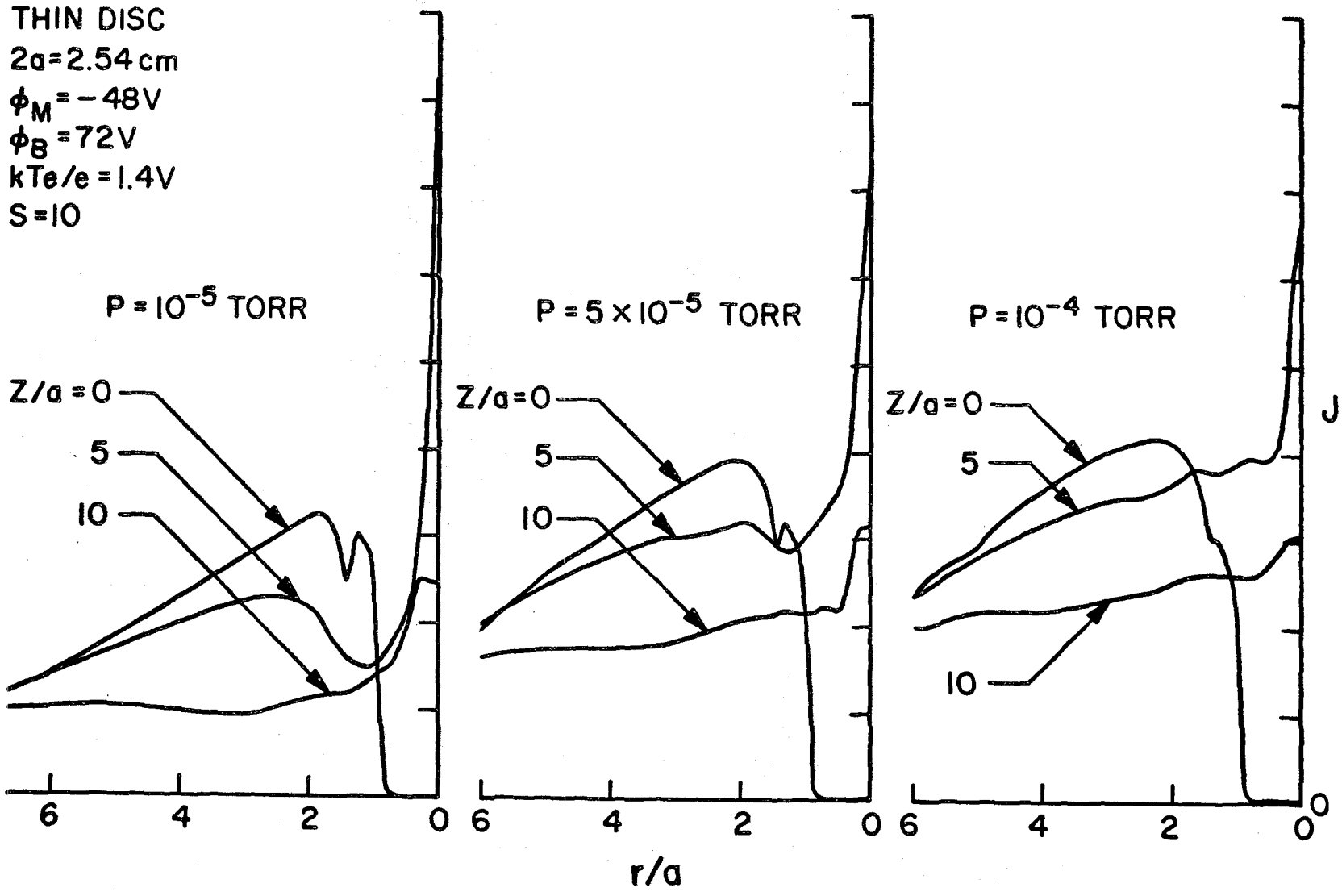

Figure 6.1 Dependence of the Near Wake of a Highly Negative Thin Disc on Background Pressure.

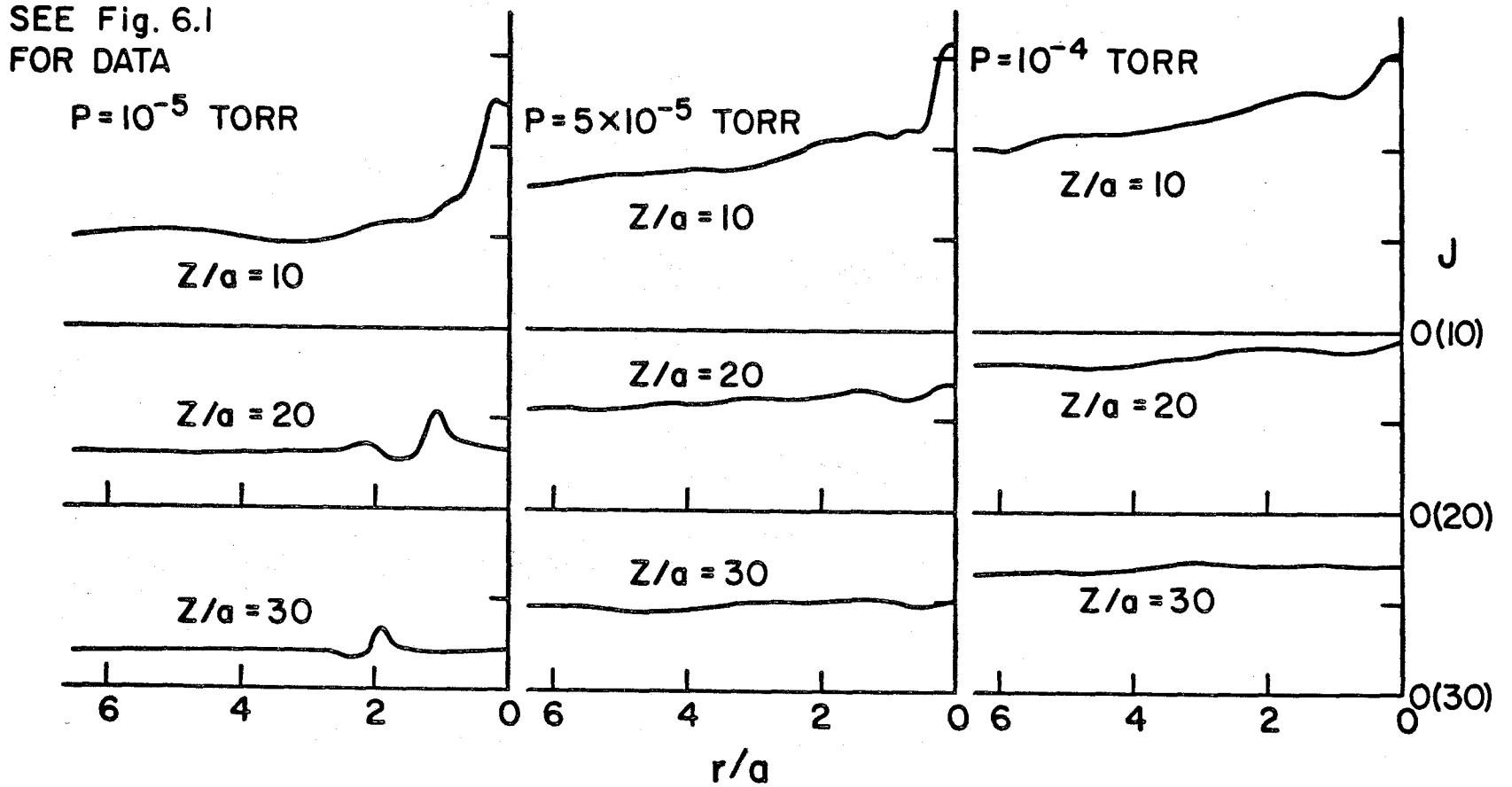

Figure 6.2 Dependence of the Far Wake of a Highly Negative Thin Disc on Background Pressure.

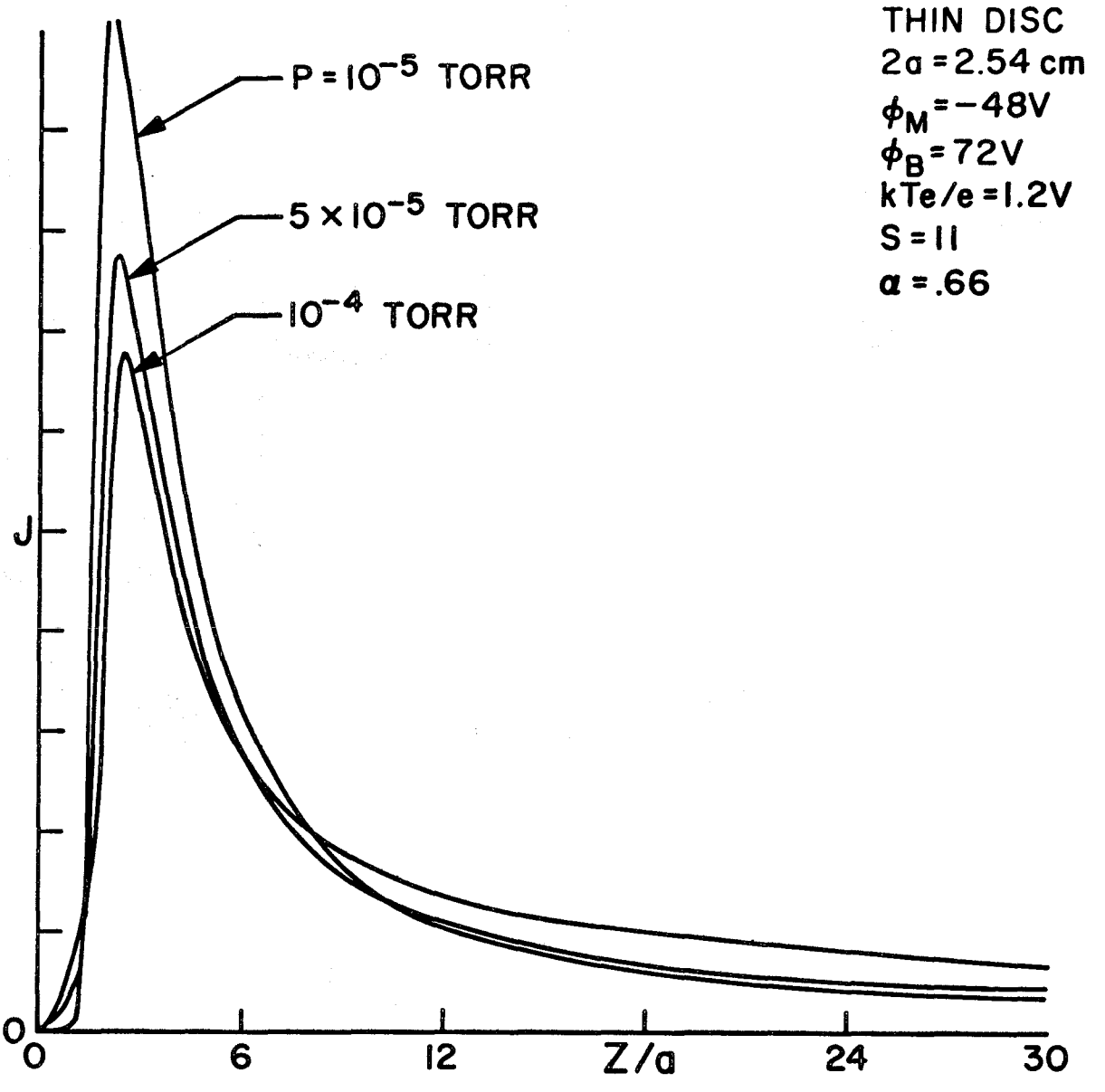

Figure 6.3 Effect of Background Pressure on the Wake of a Highly Negative Thin Disc (Axial Traces).

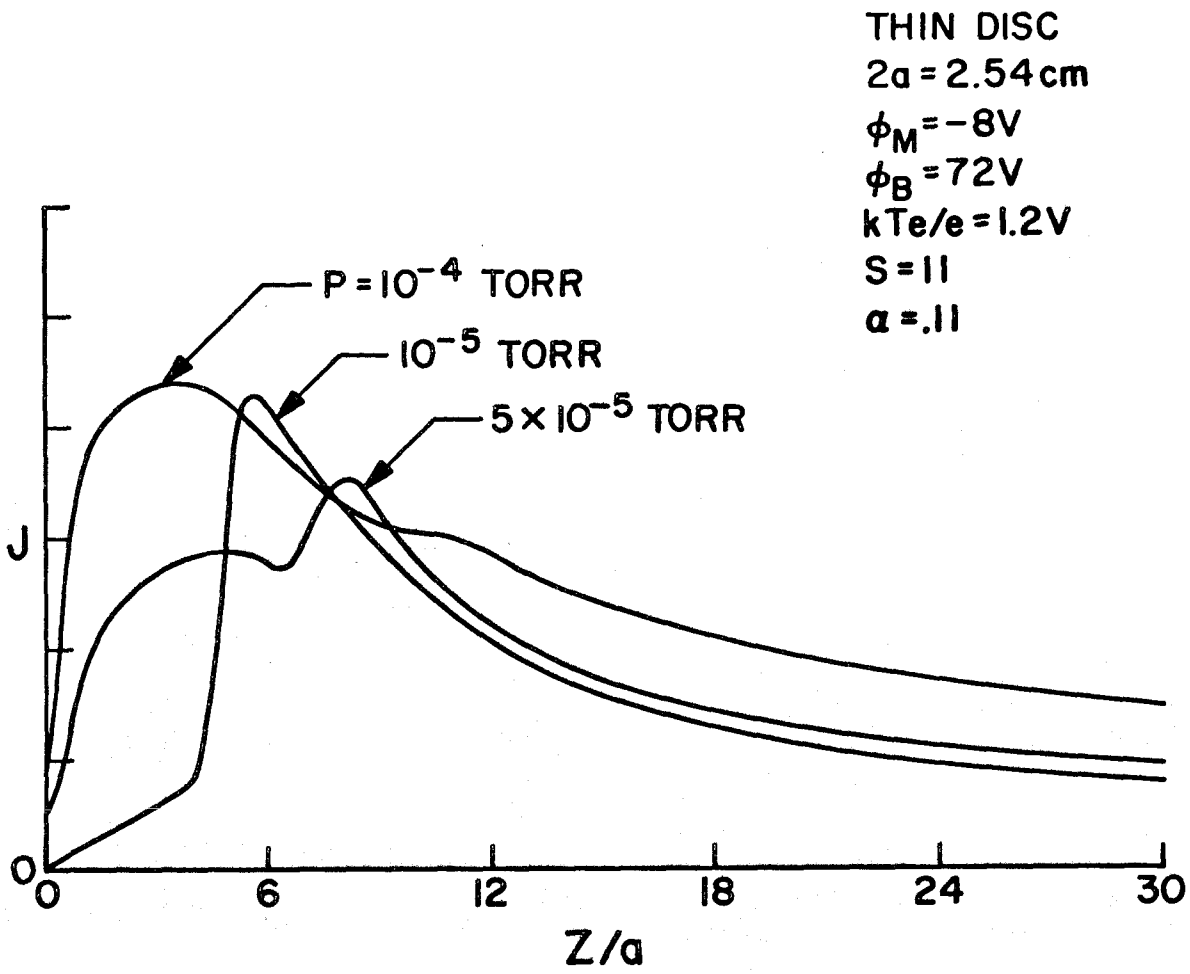

Figure 6.4 Effect of Background Pressure on the Wake of a Slightly Negative Thin Disc (Axial Traces).

APPENDIX I

First Generation Ion Source and Beam

The original ion source differed from the standard Kaufman type ion engine[35] in that it was designed to operate without the use of any containing magnetic field.

It was similar to the ones used by Meckel[21] and by Pitts and Knechtel.[22] A schematic drawing of the ion source, associated circuitry and the vacuum system is shown on Fig. A. 1. 1. All components were made of non-magnetic materials, mostly stainless steel.

The ion energy was variable from 60 to 600 eV, although most measurements were made at 100 eV, corresponding to a velocity of 22 km/sec in the case of the argon gas used. The ion density of the beam was adjustable from 3×10^7 to 3×10^8 ions/cm^3, as measured on the axis 35 cm downstream of the accelerator grid. At the model position, about 23 cm from the source grid, the beam density varied less than 15% within a radius of about 5 cm from the chamber axis; it then decayed gradually toward the chamber walls. Thus there was a fairly large area of uniform flow, and relatively large models could be tested. The beam energy for this source could be varied from 60 to 600 eV, although 100 eV was generally used.

Neutralizing electrons were supplied by hot tungsten filaments located downstream of and near to the accelerator grid. The electron temperature could be varied from 1. 5 to 6 volts by adjusting the bias of the neutralizer filament. The electron temperature and plasma potential both decreased slightly going downstream and radially outwards from the axis. The temperature variation was usually within 20% and the plasma potential within a few volts. The plasma potential

was generally within 3 or 4 KT_e/e of the grounded grid.

The plasma potential and floating potential were strongly dependent on neutralizer filament temperature which determined the amount of electron emission. When the beam was properly neutralized, the plasma potential was of the order several volts.

The source had a large accelerating grid (30 cm diameter) which made it possible to test quite large bodies (7.5 cm diameter). Because of the large grid area, the source had to be operated at the chamber background pressure. The engine could operate stably down to around 1.5×10^{-4} torr in argon, but the most frequently used set of conditions was at about 2×10^{-4} torr background pressure and 100 eV beam energy.

Most of our early data were taken at the conditions mentioned above, but upon analyzing the data, the effects of low energy ion production became apparent, as did the need for much lower background pressures.

Since the electrostatic probe is mostly sensitive to fast ion flux, a good indication of the beam ion-neutral atom mean free path could be found by measuring the flux decrease as a function of Z. For relatively short mean-free-paths, most of the decrease is due to the scattering of beam ions. At the usual operating conditions, the ion-atom free path was found to be about 25 cm which was on the order of the wake dimensions. At first this did not appear to be too great a problem. However, rough calculations soon indicated that because of the large radius of the chamber and the short mean free path, a high density of collision-produced low energy ions was likely.

This estimate was soon confirmed using the resonance probe, and it was necessary to go to a lower background pressure to eliminate the undesirable slow ions. This source was housed completely in the 50 cm diameter stainless steel vacuum chamber described in Chapter II. The chamber was identical to that used with the modified source but did not include the extension to accomodate the 40 cm pump (see Fig. A. 1. 1.

The original pumping system consisted of a 15 cm CVC diffusion pump, a liquid nitrogen baffle, a 15 cm gate valve, and a 300 L/min Welch mechanical forepump. This system could nominally handle a flow rate of 1, 400 L/sec at our normal operating pressure of 2×10^{-4} torr and would normally provide an ultimate pressure of 10^{-6} torr. With no leaks and a thorough cleaning, an ultimate pressure of 3×10^{-8} torr has been achieved.

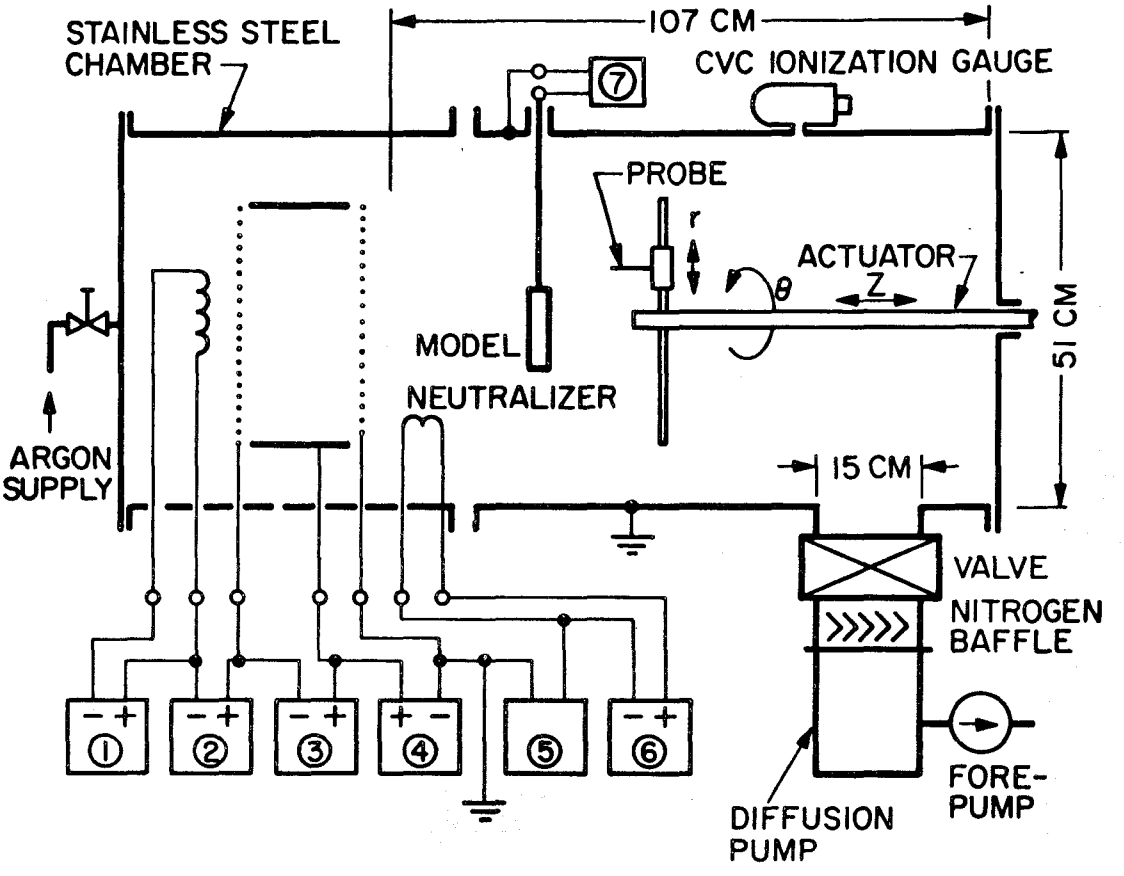

POWER SUPPLIES FOR:

1. SOURCE FILAMENT HEATER
2. ELECTRON GRID
3. ANODE
4. ACCELERATOR GRID
5. NEUTRALIZER BIAS
6. NEUTRALIZER HEATER
7. MODEL BIAS

Figure A. 1. 1 First Generation Plasma Beam Source and Chamber.

APPENDIX 2

The Resonance Probe

The resonance probe work connected with this investigation was performed by M. Sajben. Since it is an important part of the study, a short description of the probe and techniques follows. This description is taken from Ref. 26.

The density of low energy ions can be determined through independent measurement of electron density, by the following method. The Langmuir probe measures the flux of the fast directed ions, while low energy ions contribute little to the collected current unless their densities are much greater than the fast ion densities. If one assumes charge neutrality in the beam and finds the fast ion flux (and thus fast ion density) from Langmuir probe measurements, then the slow ion density can be found by subtracting the fast ion density from the electron density: $N_s = n_e - N_f$. This method will fail if the slow ion density is small compared to the electron density.

The independent electron density measurements were performed using the resonance probe technique first proposed by Takayama and his co-workers,[41] later refined by Harp, Crawford[42] and many others. The method is based on the fact that the RF admittance of the plasma sheath - plasma system has a maximum at a frequency near the electron plasma frequency. Further information on this technique can be found in Ref. 42. One of the probes and the circuit used in this experiment are shown on Fig. A. 2. 1. Cable capacitance effects were compensated for by using an exact duplicate of the probe in a completely symmetric arrangement, so that the

imbalance current measured by the two Tektronix CT-2 transformers represented the true plasma RF current. The electron density was computed from the resonance frequency using Harp's Theory for spherical resonance probes.[42]

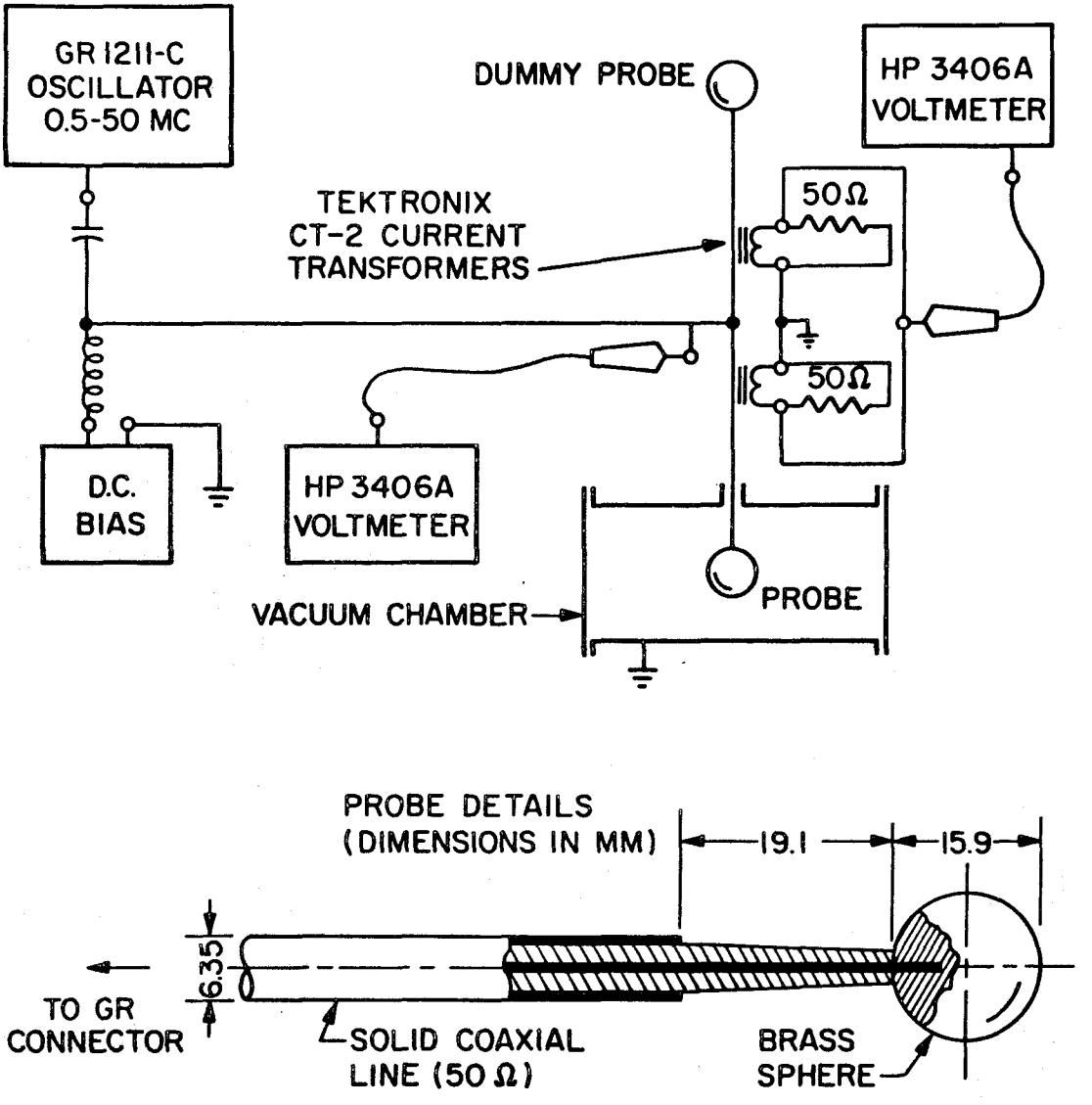

Figure A. 2. 1 Resonance Probe and Circuitry.

APPENDIX 3

Effects of Pressure and Collisions

We have mentioned that at the operational pressures of the large source described in Appendix I, collisions and the formation of slow ions are important considerations. We have also mentioned that at pressures of around 10^{-5} torr, well within the range of the second generation source, low energy ions are no longer a problem. The following is a short justification of these statements.

The large beam was normally operated at a pressure of 0.2μ which is a sufficiently high pressure to warrant an examination of the effects on the experimental results of collisions between beam ions and background neutral atoms. At 100 eV ion energy the argon ion-argon atom resonance charge transfer cross section is 28×10^{-16} cm^2, [43] and the elastic momentum transfer cross section is 20×10^{-16} cm^2. [44] The corresponding mean free paths are of the order of the test section length, and thus a large fraction of the beam ions will suffer some type of collision before reaching the end of the vacuum chamber.

The resultant density variation in the axial direction is not in itself particularly troublesome. Since the characteristic length scale of decay is much longer than the body size, it is certainly not expected to influence directly the structure of the near wake. The resultant secondary ions, however, contribute to the space charge, tend to attenuate electric fields, and thereby influence the motion of the fast ions. Secondary ions were presumably present in the experiments of Meckel[21] and Pitts,[22] while Clayden and Hurdle[24] were apparently the first to estimate and indirectly measure their density.

The secondary ion density can be estimated for an axial symmetric, uniform, parallel beam, provided that the beam radius is much less than the mean free path. Such an estimate was carried out by M. Sajben[26] and is included here.

For the above conditions, the axial decay of the beam can be neglected for the purposes of a rough approximation, and the mass balance for a cylindrical control volume of radius r can be written as

$$N_f U N_n Q r^2 \pi = N_s u_s 2 \pi r \qquad \text{(A. 3. 1)}$$

where N_f, N_n and N_s are the beam, background neutral and secondary ion densities respectively, Q is a collision cross section further specified below and u_s is the radial component of the mean velocity of secondary ions. Letting $\lambda \equiv (N_n Q)^{-1}$, we can write

$$\frac{N_s(r)}{N_f} = \frac{U_r}{2u_s(r)\lambda} \qquad \text{(A. 3. 2)}$$

The key problem is clearly the correct determination of u_s. Clayden assumed $u_s = (KT_e/M_i)^{\frac{1}{2}}$, which seems to imply that the scattered ions were accelerated across a radial potential difference of KT_e/e. Since we found our beams to be very nearly field free, the secondary ion motion in our case must be governed by the scattering process directly. The beam particles are deflected by the target atoms according to the differential cross section for elastic collisions and travel along straight lines afterwards. Since the mean free path is large compared to the beam radius, most of them will leave the beam without additional encounters with background neutrals. If the angles of deflection and the charge transfer probability are both

known as functions of the impact parameter, u_s can be calculated in a straightforward, although laborious way, using a first collision theory. In what follows we shall restrict ourselves here to the estimation of lower and upper limits for u_s, using two simple collision models.

In order to obtain a low estimate for N_s, we seek a high approximation for u_s, which requires a model having relatively large cross sections for large deflection angles. The hard sphere model is appropriate for this purpose, since its differential cross section in the laboratory frame varies as Cos θ, while real ion-atom cross sections typically have a sharp peak at small θ values.[45] The estimate will also be lowered by neglecting charge exchange reactions altogether and considering the effects of elastic deflections only. Detailed first collision calculations, not described here, show that in this case the secondary ion density on the axis is obtained by the formula:

$$\left[\frac{N_s(0)}{N_f}\right]_{min} = \frac{URN_nQ_e}{2(U/\pi)} = \frac{\pi}{2}\cdot\frac{R}{\lambda_e} \qquad \text{(A. 3. 3)}$$

where R is the beam radius and Q_e is the momentum transfer cross section. This formula is similar to and made feasible by Eq. A. 3. 2.

A high estimate is obtained if we assume that the neutral atoms gain no momentum in a collision, but will lose an electron to ions passing within a distance given by $(Q_c/\pi)^{\frac{1}{2}}$ where Q_c is the charge exchange cross section. The secondary ions produced by this mechanism would possess a Maxwellian distribution at the neutral atom temperature, T_n. Detailed calculations, omitted here, show that the

secondary ion density on the axis is then given by

$$\left[\frac{N_s(0)}{N_f}\right]_{max} = \frac{1}{2\pi}\,\frac{URN_nQ_c}{\left(\frac{8KT_n}{\pi M_n}\right)^{\frac{1}{2}}} = \frac{1}{2\pi}\,\frac{U}{\sqrt{\frac{8KT_n}{\pi M_n}}}\,\frac{R}{\lambda_c} \qquad \text{(A. 3. 4)}$$

where Q_c is the differential cross section for charge exchange at the beam energy.

For the experimental conditions, the two limits given differ by a factor of approximately 24. This ratio may be reduced through the use of more realistic differential cross sections, if necessary. However, the consideration of the lower limit alone is sufficient to point out that rather stringent requirements must be placed on the highest permissible pressure if one wishes to keep the secondary ion concentration low. Prescribing 5% secondary ion fraction, it is quickly found that the mean free path must be at least 31 times the beam radius!

From these estimates it is clear that substantial secondary ion densities had to exist in our first experiment.

Verification of this fact was obtained through the resonance probe measurements performed by M. Sajben (Appendix 2). Fig. A.2.1 shows the measured electron densities on the axis, 51 cm from the accelerator, normalized by the fast ion density. Despite the scatter, the data indicate a roughly linear relation between the pressure and secondary ion density, bounded by the two limits given in Eqs. A. 3. 3 and A. 3. 4. It may be concluded that secondary ions cannot be ignored in an argon beam of this size unless the test section pressure is well below 10^{-5} torr. For the smaller beam of the low pressure source,

10^{-5} torr should be sufficiently low for secondary ions to be ignored. This has been confirmed by our measurements and is in agreement with the results of Hester and Sonin.[27]

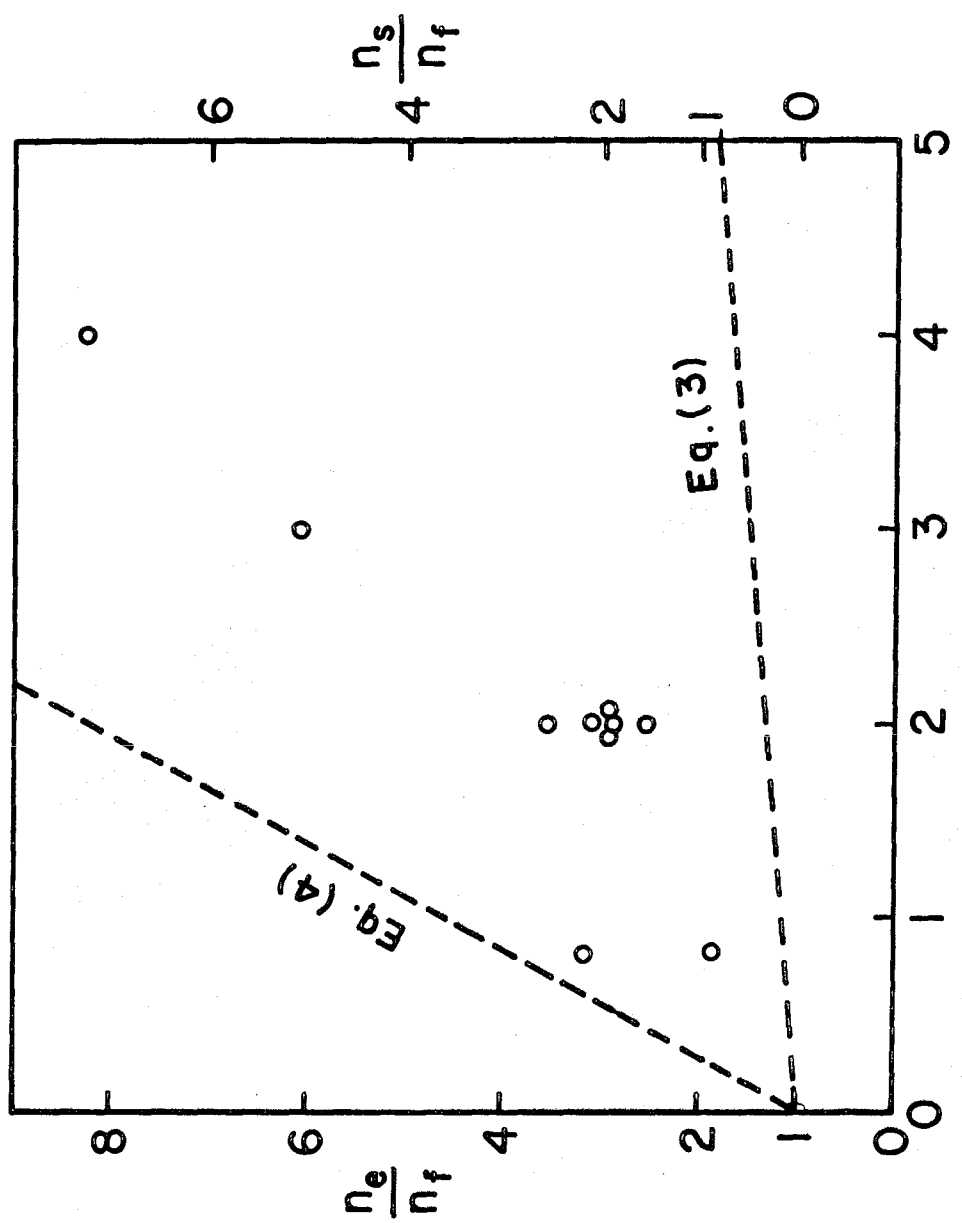

Figure A. 3.1 Electron and Secondary Ion Densities on the Axis 51 cm from Accelerator Grid of Original Source Compared to Estimates of Appendix 3.

APPENDIX 4

Estimate of the Relative Magnitudes of the Electric Fields in the Void and Sheath Regions

For a crude estimate of the ratio of the field in the void to the field in the sheath, assume the sheath field (E_s) is on the order of $|\varphi_M|/h$ and the void field (E_v) is approximately $|\varphi_v|/a$, where φ_v is the potential on the axis in the void region. Thus:

$$|E_s| \sim \frac{|\varphi_M|}{h} \tag{A.4.1}$$

and

$$|E_v| \sim \frac{|\varphi_v|}{a} \quad . \tag{A.4.2}$$

The potential on the axis of a cylindrical volume filled with Maxwellian electrons is known exactly (Ref. 46). Using this value as an estimate for the void region, we have

$$|\varphi_v| \approx \left(\frac{KT_e}{e}\right) \ell n \left[\frac{1}{8}\left(\frac{a}{h}\right)^2\right] \quad . \tag{A.4.3}$$

(Eq. A.4.3 overestimates $|\varphi_v|$.) One finds

$$\frac{|E_v|}{|E_s|} \sim \frac{\frac{h}{a}\ \ell n\left[\frac{1}{8}\left(\frac{a}{h}\right)^2\right]}{\frac{e\varphi_M}{KT_e}} \quad . \tag{A.4.4}$$

For the slightly negative case of Fig. 4.1,

$a/h = 21$ and $\frac{e\varphi_M}{KT_e} = 9$. Thus

$$\frac{|E_v|}{|E_s|} \sim \frac{\ell n\ 55}{21 \times 9} = 0.0212 << 1$$

For a floating body, $\frac{e\varphi_M}{KT_e}$ is approximately 3 and the above ratio would be about 0.06.

The ratio of the inward momentum due to the void and the sheath can also be estimated. The momentum change in the radial direction should be approximately proportional to the radial field strength times the time for which an ion is in this field. If the beam speed stays approximately constant, this time will be proportional to a characteristic length for the field. An ion is in the sheath field for a distance of about $L + 2h$ and is in the void field for a distance on the order of a model radius. Thus:

$$\Delta(M_i V)_s \sim E_s (L+2h) \qquad \text{(A.4.5)}$$

and

$$\Delta(M_i V)_v \sim E_v a \quad . \qquad \text{(A.4.6)}$$

The ratio of the radial momentum changes due to the void and the sheath is then given by

$$\frac{\Delta(M_i V)_v}{\Delta(M_i V)_s} \sim \frac{|E_v|}{|E_s|} \frac{a}{L+2h} \quad . \qquad \text{(A.4.7)}$$

For a floating thin disc where $a/h = 21$ and $L/h \ll 1$,

$$\frac{\Delta(M_i V)_v}{\Delta(M_i V)_s} \sim 0.06\ (11) = 0.66$$

For a highly negative thick disc where $a/h = 21$, $L/h = 10$ and $\frac{e\varphi_M}{KT_e} = 50$,

$$\frac{\Delta(M_i V)_v}{\Delta(M_i V)_s} \sim 0.0038\ (\frac{21}{12}) = .0066 \quad .$$

Thus the effect of the electric field in the void region on the wake is comparable to that of the field in the sheath region only for

very weakly charged bodies. The estimates given here apply to the disc case; similar results can also be obtained for the strip case.

APPENDIX 5

Wakes of Segmented Sphere and Screen Models

Segmented Sphere

This appendix describes the wakes of two models not discussed in the text. The segmented sphere is shown in Fig. 2.9. The ring around the center of the model can be biased separately from the rest of the sphere. This model was used to show that it may be possible to modify the wake of a real satellite by means of onboard power supplies.

Fig. A.5.1 contains axial probe traces behind the sphere for three different model conditions. The strongest peak is obtained when all surfaces of the sphere are biased highly negatively ($\alpha = .66$). The weakest peak results if all parts of the model are connected together and the assembly is at floating potential ($\alpha = .11$). The third wake is for the ring biased 40V negative with respect to the rest of the model but the model as a whole is floating. It is clear from Fig. A.5.1 that the peak position and strength can be influenced by biasing one part of a model or satellite with respect to another. The radial traces for this model were similar to those at the thick disc. Figs. A.5.2 and A.5.3 show radial traces for the model floating. The traces for the other two cases were similar, except for the variations in peak position.

Screen

The screen model was approximately the same size as the thin disc model, but it was made of brass screening identical to that used in the ion grid of the source. The screen was much thinner than a

Debye length and had about 70% open area. The grid spacing was approximately 0.5 mm. This model was included to demonstrate that the fine structure of the far wake is affected by variations in the conditions presented by the near wake. Figs. A.5.4 and A.5.5 show radial traces at the wake at the slightly negative screen. Note how the complicated upstream condition ($Z/a = 8$) generates a quite complicated far wake structure. The last trace on Fig. A.5.5 is a repeat at the $Z/a = 30$ curve enlarged five times.

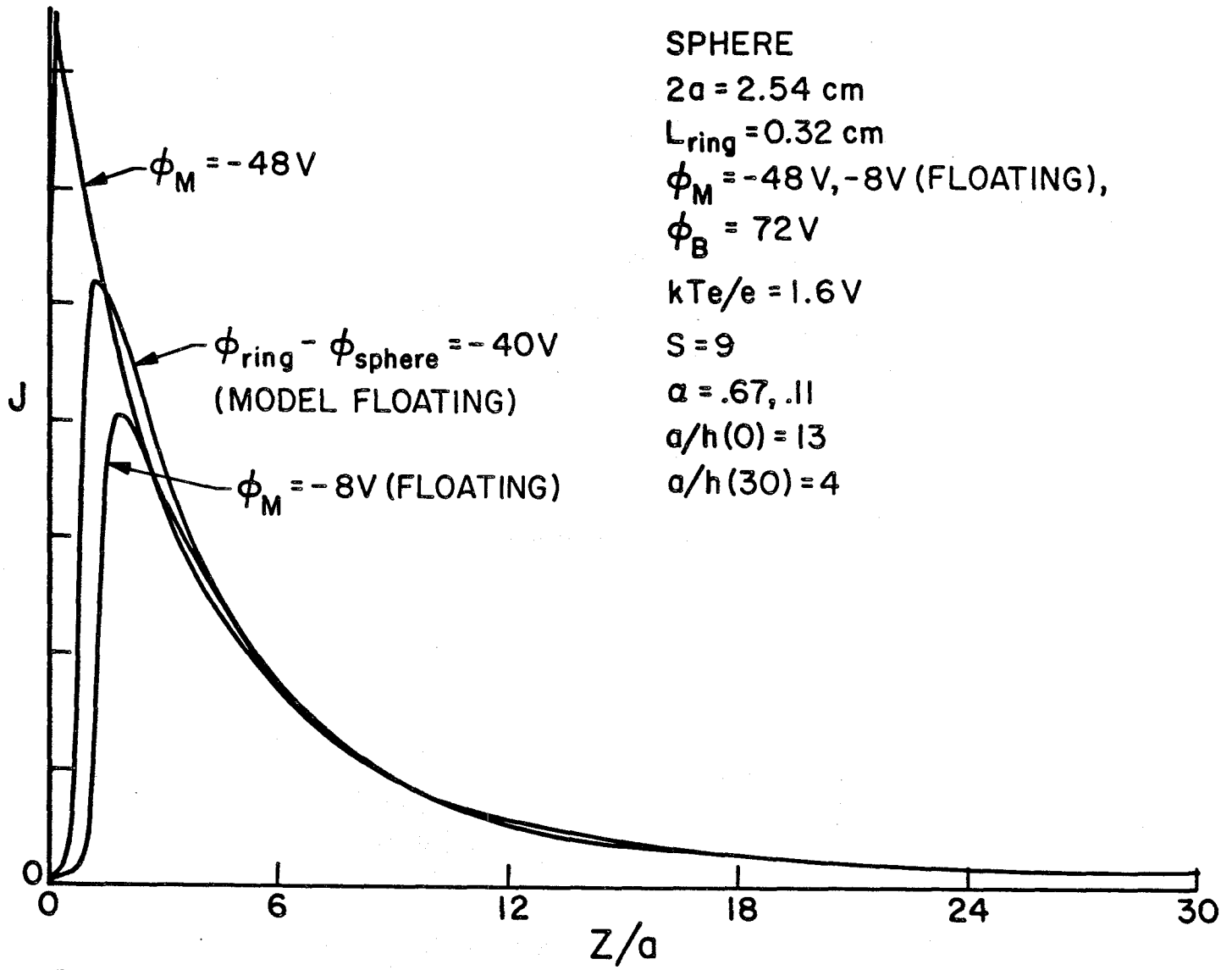

Figure A. 5. 1 Effect of Model Potential Distribution on the Wake of a Segmented Sphere (Axial Traces).

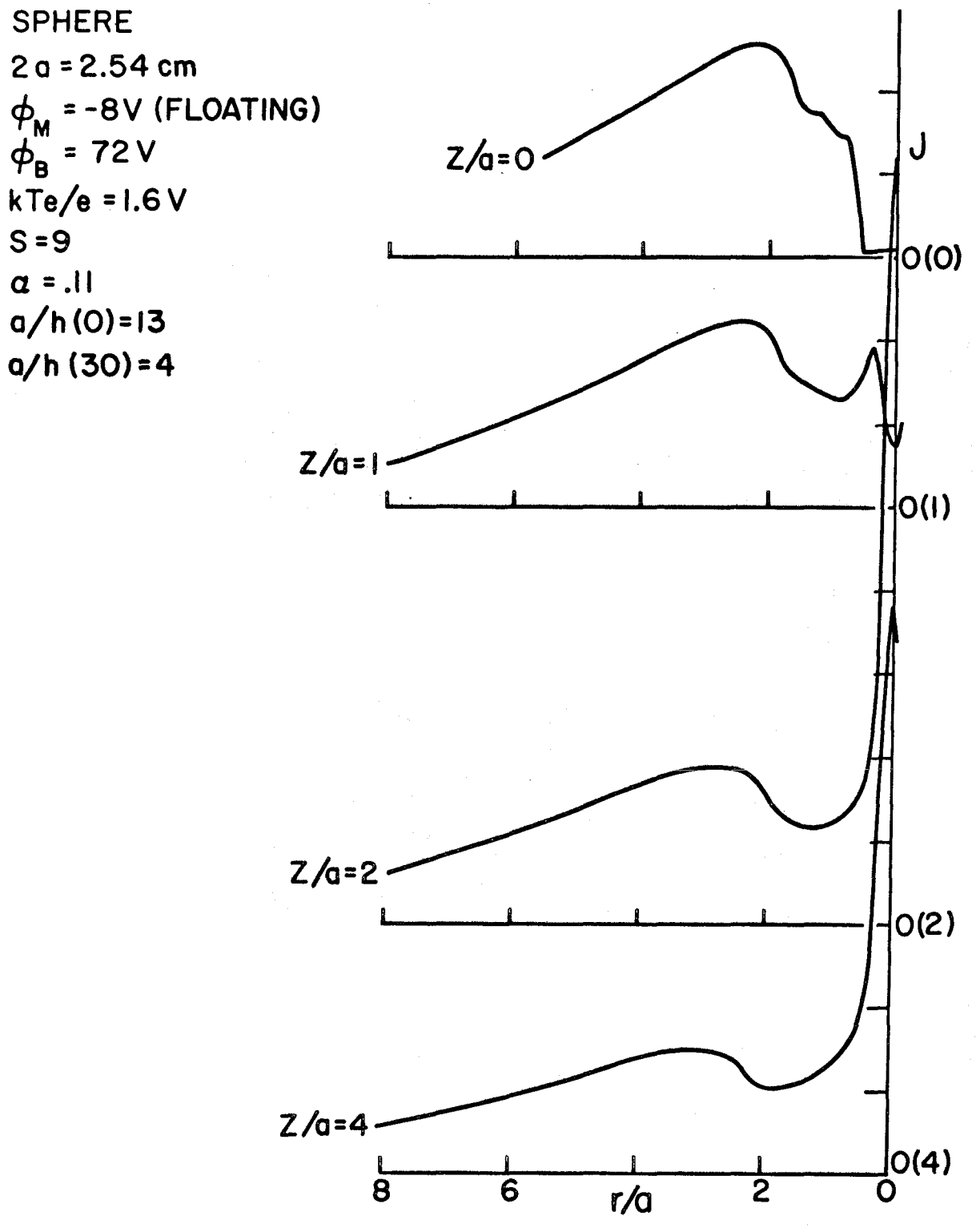

Figure A. 5. 2 Near Wake of a Floating Sphere.

SPHERE

$2a = 2.54$ cm

$\phi_M = -8V$ (FLOATING)

$\phi_B = 72V$

$kTe/e = 1.6V$

$S = 9$

$\alpha = .11$

$a/h(0) = 13$

$a/h(30) = 4$

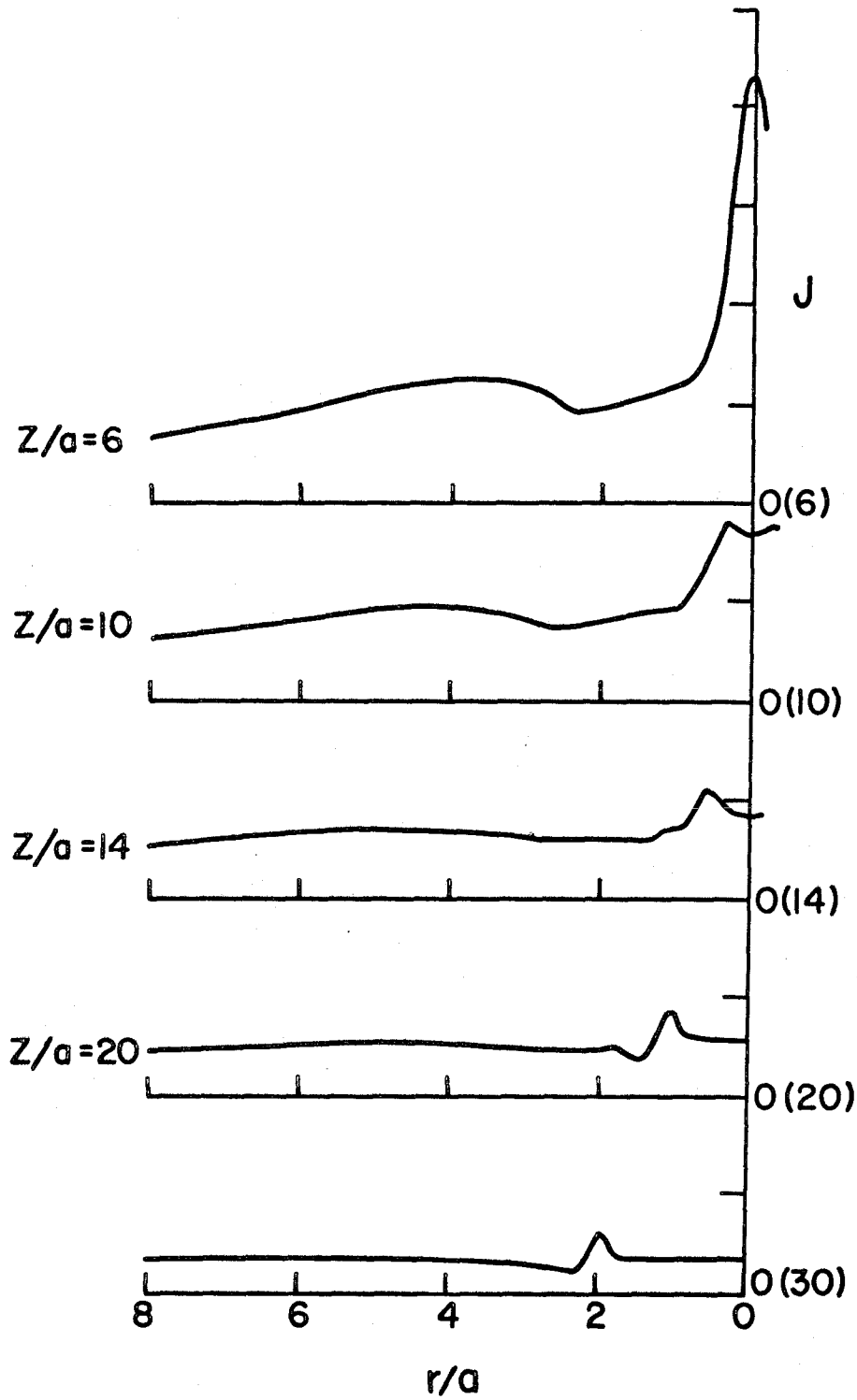

Figure A. 5. 3 Far Wake of a Floating Sphere.

THIN SCREEN
2a = 2.54 cm
ϕ_M = -10 V
ϕ_B = 70 V
kTe/e = 2.1 V
S = 7
α = .14
a/h (0) = 12
a/h (30) = 5

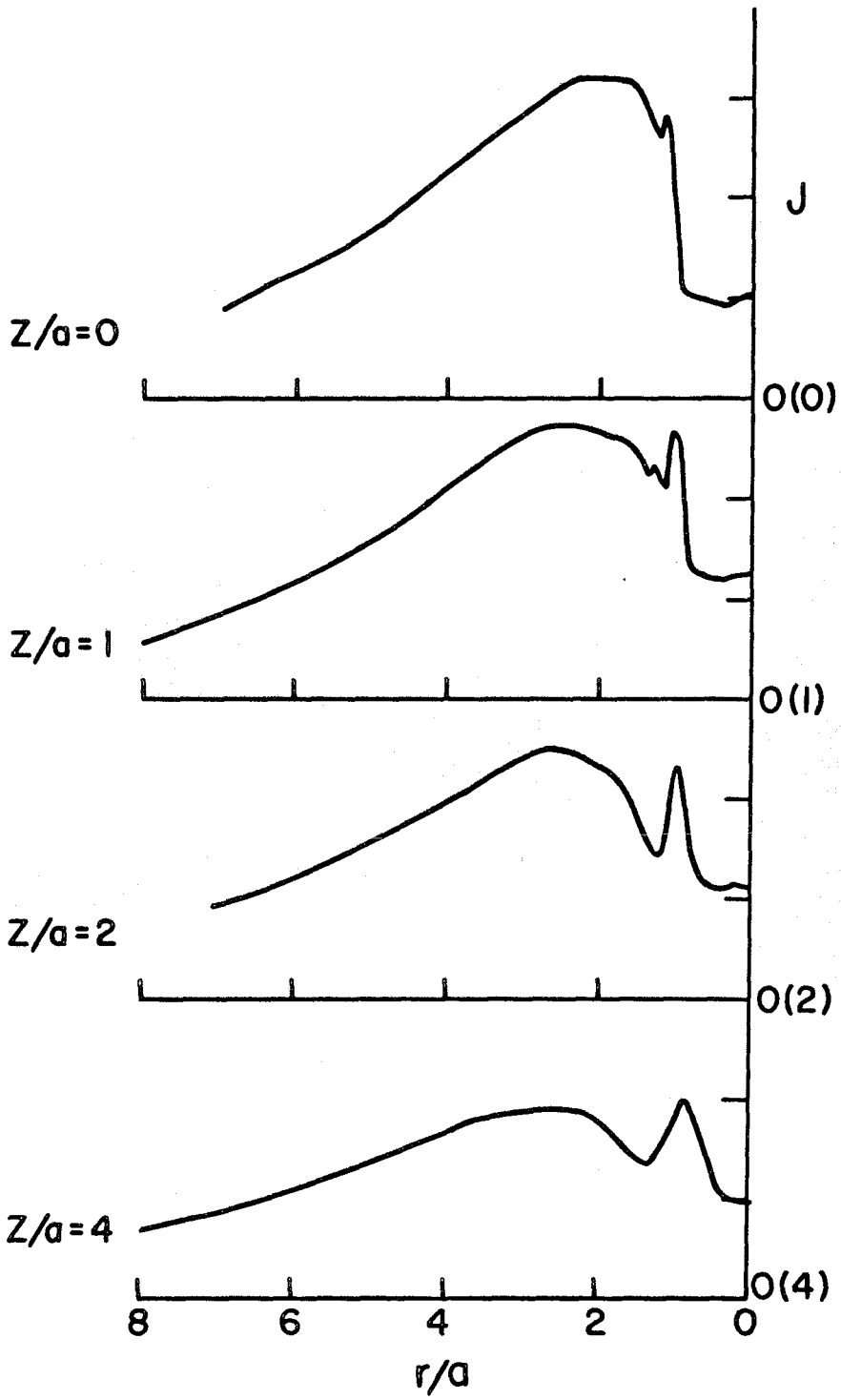

Figure A. 5. 4 Near Wake of a Slightly Negative Thin Disc-shaped Screen.

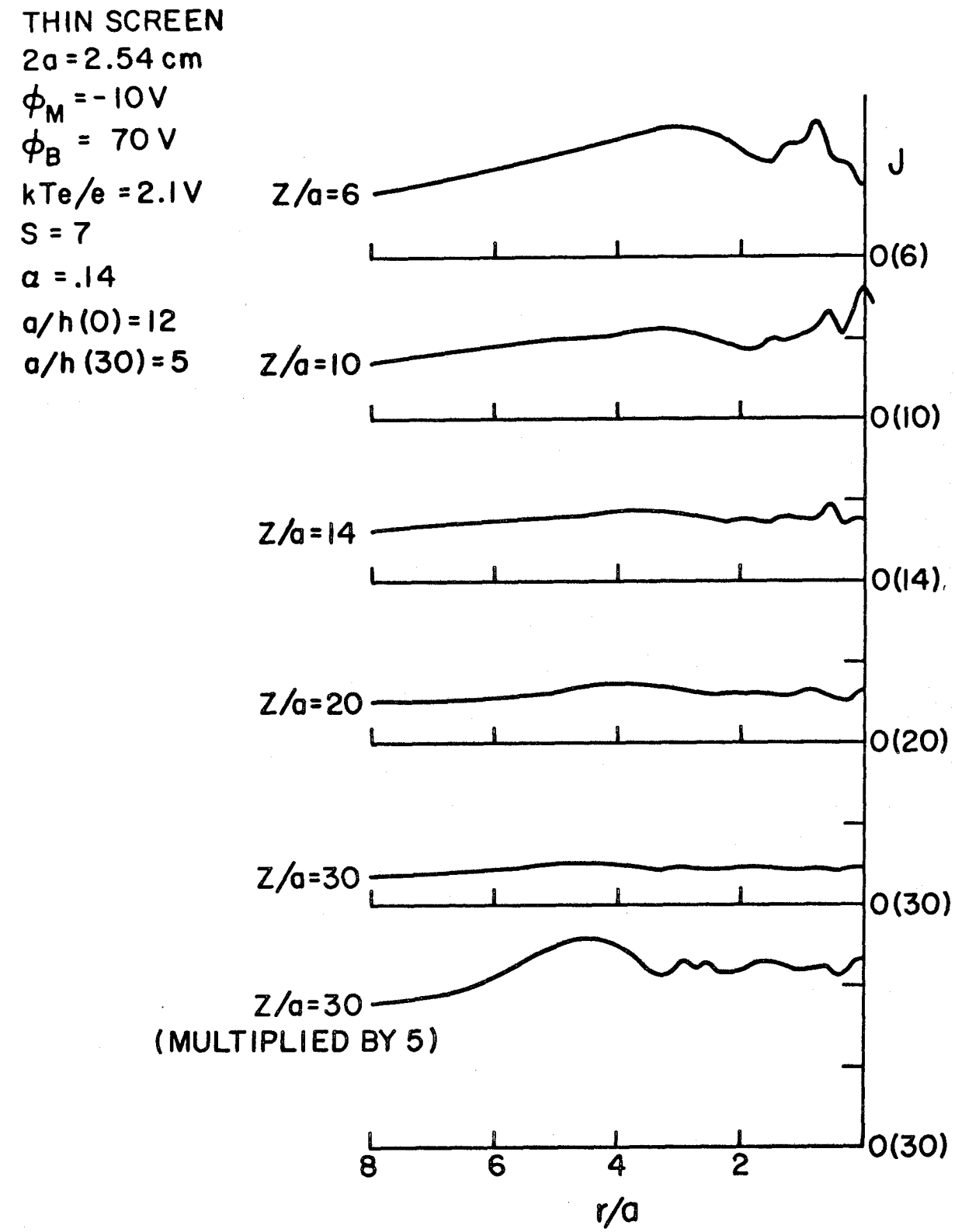

Figure A. 5. 5 Far Wake of a Slightly Negative Thin Disc-shaped Screen.

APPENDIX 6

Details of the Near Wake Theory of Chapter IV

The following is a more detailed derivation of the crude theoretical results for peak position presented in Chapter IV. 5. This theory applies to a conducting strip or disc with a radius or width much larger than the Debye length and with: $a >> L >> h$.

Fig. 4.13 shows the geometry of the interaction of the beam ions with the disc. We assume that all interaction between the beam ions and the disc takes place in the shaded region. The Z velocity (U) of the ions remains constant throughout the interaction, and any ions which hit the model are absorbed. Since all the model dimensions are much greater than the Debye length and most of the beam-model interaction is close to the body, the body can be assumed locally flat and any transverse curvature can be ignored. We also assume that once an ion leaves the shaded region it travels in a straight line. To find the peak position we must know the radial velocity, v, of the ion which just misses the body at $Z = 0$.

The ion motion is governed by the following momentum equation:

$$Mv = \int_0^t e E \, dt \qquad \text{(A. 6. 1)}$$

where M is the ion mass and v is the radial velocity. Since U is constant we can rewrite this as:

$$Mv = M \frac{dr}{dt} = M \frac{dr}{dZ} U = \int_{-L}^{0} e E \frac{dZ}{U} \qquad \text{(A. 6. 2)}$$

The potential in the interaction region is defined by:

$$\varphi = \varphi_M \exp(-\frac{r-a}{h}) \qquad \text{(A. 6. 3)}$$

Thus: $E = -\frac{d\varphi}{dr} = \frac{\varphi_M}{h} \exp(-\frac{r-a}{h})$ (A. 6. 4)

and:
$$Mv = M\frac{dr}{dZ}U = \int_{-L}^{0} e\frac{\varphi_M}{h} \exp\left[-\frac{r-a}{h}\right]\frac{dZ}{U} \quad . \qquad \text{(A. 6. 5)}$$

to find v we must solve for $r(Z)$.

The solution is found as follows: differential Eq. (A. 6. 5) to get:

$$M\frac{d^2r}{dZ^2}U = \frac{e\varphi_M}{Uh} \exp\left[-\frac{r-a}{h}\right]$$

or

$$\frac{d^2r}{dZ^2} = \underbrace{\frac{e\varphi_M}{\frac{1}{2}MU^2}}_{-\alpha}\frac{1}{2h} \exp\left[-\frac{r-a}{h}\right] \qquad \text{(A. 6. 6)}$$

Next let $\frac{dr}{dZ} = \psi$, then,

$$\frac{d}{dZ}\frac{dr}{dZ} = \frac{1}{2}\frac{d}{dr}(\psi^2) \qquad \text{(A. 6. 7)}$$

or $$\frac{1}{2}\frac{d}{dr}(\psi^2) = -\frac{\alpha}{2h} \exp\left[-\frac{r-a}{h}\right] \quad . \qquad \text{(A. 6. 8)}$$

Integrating:

$$\psi^2 = \alpha \exp\left[-\frac{r-a}{h}\right] + \text{const.} \qquad \text{(A. 6. 9)}$$

Since $v = \frac{dr}{dt} = 0$ at $Z = -L$, $\frac{dr}{dZ} = \psi = 0$

at $r = r_i$, where r_i is the initial radius of the ion entering the shaded interaction area of Fig. 4. 13. Thus:

$$\psi = \frac{dr}{dZ} = \sqrt{\alpha}\left(\exp\left[-\frac{r-a}{h}\right] - \exp\left[-\frac{r_i-a}{h}\right]\right)^{\frac{1}{2}} \qquad \text{(A. 6. 10)}$$

Rearranging:

$$\sqrt{\alpha}\exp\left[-\tfrac{1}{2}\frac{r_i-a}{h}\right]dZ = \frac{dr}{(\exp[-(r-r_i)/h]-1)^{\frac{1}{2}}}$$

or
$$\sqrt{\alpha}\exp\left[-\tfrac{1}{2}\frac{r_i-a}{h}\right](Z+L) = \int_{r_i}^{r}\frac{dr}{(\exp[-(r-r_i)/h]-1)^{\frac{1}{2}}} \qquad \text{(A. 6. 11)}$$

To evaluate the integral, let $r-r_i = r'$ to get:

$$\int_0^{r-r_0}\frac{dr'}{(\exp[-r'/h]-1)^{\frac{1}{2}}} = \int_{r_i}^{r}\frac{dr}{(\exp[-(r-r_i)/h]-1)^{\frac{1}{2}}} \qquad \text{(A. 6. 12)}$$

Then let $\exp\left(\frac{-r'}{h}\right) = y$ to give:

$$dr' = -h\frac{dy}{y} \quad .$$

Substituting into the integral and using Dwight #192. 11[47]

$$-h\int_1^{e^{-(r-r_i)/h}}\frac{dy}{y(y-1)^{\frac{1}{2}}} = -h\left[2\tan^{-1}(y-1)^{\frac{1}{2}}\right]_1^{e^{-(r-r_i)/h}} \qquad \text{(A. 6. 13)}$$

Substituting the right side of (A. 6. 13) for the integral in (A. 6. 11) and rearranging, we obtain:

$$r = r_i - 2h\,\ell n\left[\mathrm{Sec}\left\{\left(e^{-\frac{r_i-a}{2h}}\right)\frac{\sqrt{\alpha}(Z+L)}{2h}\right\}\right] \qquad \text{(A. 6. 14)}$$

For convenience we define:

$$\beta = \frac{\sqrt{\alpha}}{2h}\exp\left[-\frac{r_i-a}{2h}\right]$$

Then $r = r_i - 2h\,\ell n\,[\mathrm{Sec}\,\beta(Z+L)]$ (A. 6.14a)

The radial velocity of an ion in the interaction region is then given by:

$$\frac{v}{U} = \frac{dr}{dZ} = -2h\beta\tan[\beta(Z+L)] \qquad \text{(A. 6. 15)}$$

The ion will leave the interaction region with the radial velocity given by setting Z = 0 in Eq. (A. 6. 15).

It is easy to see that for any φ_M and L, there will be a minimum r_i for particles to enter the wake. All ions with r_i less than this $r_{0,\,min}$ will hit the model. $r_{0,\,min.}$ is found by setting $r(Z=0) = 0$. Thus from (A. 6. 14)

$$r_{0,\,min} = a+2h\,\ell n\ [Sec(\beta_0 L)] \tag{A. 6. 16}$$

where: $$\beta_0 = \frac{\sqrt{\alpha}}{2h}\ \exp\left[-\frac{r_0-a}{2h}\right]$$

or

$$\exp\left[\frac{r_0-a}{2h}\right] = \mathrm{Cos}\left\{\left(\exp\left[\frac{r_0-a}{2h}\right]\right)\frac{\sqrt{\alpha}\,L}{2h}\right\} \tag{A. 6. 17}$$

The peak position is the point where an ion starting at $r_{0,\,min}$ hits the axis. This point is given by

$$Z_p/a = \frac{v(r_i=r_0,\ Z=0)}{u} \tag{A. 6. 18}$$

If we define $Y_p = 2L\beta_0$, then from (A. 6. 17) we get an implicit equation for Y_p:

$$\boxed{Y_p = (L/h)\sqrt{\alpha}\ \mathrm{Cos}(Y_p/2)} \tag{A. 6. 19}$$

and from (A. 6. 15) and (A. 6. 18)

$$\boxed{Z_p/a = L/h\ [Y_p \tan(Y_p/2)]^{-1}}$$

This analysis assumes that the sheath is very thin compared to the model dimensions and that model curvature can be ignored. To show that this is indeed the case, it is useful to look at a few values of $R_{0,\,min}$ for various values of α and L/h. The following table lists

a few such values:

L/h	α	$r_{0,\,min}/h$
5	.1	.44
10	.1	1.04
15	.1	1.55
100	.1	4.74
5	.5	1.18
10	.5	2.14
15	.5	2.78
100	.5	6.3

One can see from the table that $r_{0,\,min}/h$ is always small compared to L/h and a/h.

APPENDIX 7

Some Details of the Far Wake Solutions of Chapter V

In this appendix, we will present some of the details of the specific solutions for N given in Chapter V. 1. To find $N(\rho, \tau)$ or $N(\xi, \tau)$ for any given initial condition, one must evaluate Eq. 5.18 or 5.22. To do this, one must first find $\bar{N}(k, 0)$ and $\frac{\partial \bar{N}(k, 0)}{\partial \tau}$. The integrals given in Eqs. 5.18 and 5.22 can then be calculated on the computer. We will derive $\bar{N}(k, 0)$ and $\frac{\partial \bar{N}}{\partial \tau}(k, 0)$ for the various initial conditions presented in Chapter V. 1 and also for some step function initial density distributions. The step function results for N will be presented at the end of this appendix.

One Dimensional Case

Let us first look at the one-dimensional cosine initial distribution used for Fig. 5.4. $N(\xi, 0)$ is given by Eq. (5.24):

$$\begin{aligned} N(\xi, 0) &= \cos\left(\frac{\pi}{2}\frac{\xi}{b}\right) && 0 \le |\xi| \le b \\ &= 0 && b < |\xi| \end{aligned} \qquad \text{(A. 7. 1)}$$

In this case $v(\xi, 0) = 0$, so using Eq. (5.17) the second integral of Eq. (5.18) is zero. Since $N(\xi, 0)$ is symmetric about $\xi = 0$ we can write from Eq. (5.14)

$$\bar{N}(k, 0) = \sqrt{\frac{2}{\pi}} \int_0^\infty N(\xi, 0) \cos(k\xi)\, d\xi \qquad \text{(A. 7. 2)}$$

From (A. 7. 2) it is also clear that $\bar{N}(k, 0)$ is an even function and Eq. (5.18) can be written

$$N(\xi, \tau) = \sqrt{\frac{2}{\pi}} \int_0^\infty \bar{N}(k, 0) \cos\{\omega(k)\tau\} \cos(k\xi) dk \qquad \text{(A. 7. 3)}$$

where $\omega(k) = \sqrt{\frac{k^2}{1+k^2}}$.

Substituting (A. 7. 1) into (A. 7. 2) and evaluating the integral we get:

$$\bar{N}(k, 0) = \sqrt{\frac{\pi}{2}}\, b \left(\frac{\mathrm{Cos}\{k\, b\}}{\frac{\pi^2}{4} - k^2 b^2} \right) \qquad \text{(A. 7. 4)}$$

This leaves Eq. (A. 7. 3) as

$$N(\xi, \tau) = b \int_0^\infty \frac{\mathrm{Cos}\, k b}{\frac{\pi^2}{4} - k^2 b^2} \mathrm{Cos}\{\omega(k)\, \tau\} \mathrm{Cos}\, k \xi\, dk \qquad \text{(A. 7. 5)}$$

This can be evaluated on the computer for various values of ξ, τ, and b to give the results shown in Figs. 5. 3, 5. 4 and 5. 5. For b = 5 this also gives the "without" curves of Fig. 5. 9.

To get the "with" curves of Fig. 3. 29, we must add the effects of an initial velocity distribution and thus must include the second integral of Eq. (3. 2. 18). For Fig. 5. 9, we assumed an initial velocity distribution given by Eq. (5. 32) of:

$$\begin{aligned} \frac{v}{c}(\xi, 0) &= -\frac{v_0}{c} \mathrm{Sin}\left(\pi \frac{\xi}{\beta}\right) && |\xi| < \beta \\ &= 0 && |\xi| \geq \beta \end{aligned} \qquad \text{(A. 7. 6)}$$

Using Eq. (5. 17) and the fact that $\frac{\partial v(\xi, 0)}{\partial \xi}$ is even, we get:

$$\begin{aligned} \frac{1}{\omega} \frac{\partial \bar{N}(k, 0)}{\partial \tau} &= +\sqrt{\frac{\pi}{2}} \frac{v_0}{\omega \beta c} \int_0^\beta 2 \,\mathrm{Cos}\, \pi \frac{\xi}{\beta} \,\mathrm{Cos}\, k \xi\, d\xi \\ &= \sqrt{2\pi} \frac{v_0}{c} \beta \frac{k}{\omega} \frac{\mathrm{Sin}\, k \beta}{\pi^2 - k^2 \beta^2} \end{aligned} \qquad \text{(A. 7. 6a)}$$

Thus using Eq. (5. 18) and the fact that $\frac{1}{\omega} \frac{\partial \bar{N}}{\partial \tau}(k, 0)$ is even with respect to k:

$$N(\xi, \tau) = b \int_0^\infty \frac{\text{Cos } k\,b}{\frac{\pi^2}{4} - k^2 b^2} \text{Cos}(\omega(k)\tau)\ \text{Cos}(k\,\xi)dk + 2\,\frac{v_0}{c}\,\beta \int_0^\infty \frac{\sqrt{1+k^2}}{\pi^2 - k^2\beta^2} \text{Sin}(k\beta)\text{Sin}(\omega\tau)\text{Cos}(k\xi)dk \tag{A.7.7}$$

The integrals in Eq. (A. 7. 7) are integrated on the computer to give the results shown in Fig. 5. 9.

While looking at the one-dimensional solutions it is interesting to work out the case of a step function initial distribution with an initial velocity. We have examined the solution for an initial distribution given by:

$$\begin{aligned} N(\xi, 0) &= 1 \qquad 0 \le |\xi| \le b \\ &= 0 \qquad |\xi| > b \end{aligned} \tag{A. 7. 8}$$

Using Eq. (A. 7. 2), $\bar{N}(k, 0)$ is given by:

$$\bar{N}(k, 0) = \sqrt{\frac{2}{\pi}}\ \frac{\text{Sin } k\,b}{k} \tag{A. 7. 9}$$

Since $\bar{N}(k, 0)$ is even, we can use Eq. (A. 7. 3) to get

$$N(\xi, \tau) = \frac{2}{\pi} \int_0^\infty \frac{\text{Cos}(\omega\tau)\ \text{Cos}(k\xi)\ \text{Sin}(kb)}{k}\, dk \tag{A.7.10}$$

Figs. (A. 7. 1) and (A. 7. 2) show $N(\xi, \tau)$ for b = 3 and b = 20. It is worth noting that the small disturbance in the b = 3 case develops much like the cosine b = 3 case of Fig. 5. 4. The b = 20 case also develops similarly to the cosine b = 20 disturbance of Fig. 5. 3, but there is a considerable amount of small wavelength disturbance

superimposed on the step function disturbance. This is probably due to the fact that the step function initial disturbance is actually composed of superimposed disturbances of all wavelengths.

Cylindrical Case

The solutions for the cylindrical case are given by Eq. (5.22). Since we did not examine initial velocity distributions in cylindrical coordinates, we are only concerned with cases where the second integral of Eq. (5.22) is zero. For the results shown in Figs. 5.6, 5.7, and 5.8, we assumed a Bessel function initial distribution given by:

$$\begin{aligned} N(\rho, 0) &= J_0(\alpha_1 \tfrac{\rho}{b}) && \rho \le b \\ &= 0 && \rho > b \end{aligned} \qquad \text{(A.7.11)}$$

where α_1 is the first root of J_0. $\overline{N}(\rho, 0)$ is then given by:

$$\begin{aligned} \overline{N}(\rho, 0) &= \int_0^b J_0\left(\frac{\alpha_1}{b}\rho\right) J_0(k\rho)\, \rho\, d\rho \\ &= \frac{\alpha_1 b^2}{k^2 b^2 - \alpha_1^2} J_0(kb) J_1(\alpha_1) \quad \text{if } \alpha_1/b \neq k \\ &= \frac{b^2}{2} [J_1(\alpha_1)]^2 \quad \text{if } \alpha_1/b = k \end{aligned} \qquad \text{(A.7.12)}$$

$N(\rho, \tau)$ is then given by Eq. (5.22) as

$$N(\rho, \tau) = \int_0^\infty \left(\frac{\cos(\omega\tau) J_0(k\rho) k}{\alpha_1^2 - k^2 b^2} \alpha_1 b^2 J_0(kb) J_1(\alpha_1) \right) dk \quad , \qquad \text{(A.7.13)}$$

where $\omega = \sqrt{k^2/1+k^2}$.

When $\alpha_1/b = k$, the integrand is given by:

$$\cos(\omega\tau) J_0(k\rho) \frac{b^2}{2} [J_1(\alpha_1)]^2 \quad ,$$

where $\alpha_1 = 2.4048$ and $J_1(\alpha_1) = .5191$. Eq. (A. 7. 13) was integrated numerically to give the results in Figs. 5. 6, 5. 7 and 5. 8.

We have also worked out the step function case in cylindrical coordinates. The disturbances resulting from the step function initial distribution compare to the Bessel function disturbances in much the same way as the one-dimensional step function results compared to those at the cosine distribution. The initial distribution $N(\rho, 0)$ is given by:

$$\begin{aligned} N(\rho, 0) &= 1 \qquad \rho \leq b \\ &= 0 \qquad \rho > b \end{aligned} \tag{A.7.14}$$

This gives:

$$\overline{N}(k, 0) = \frac{b}{k} J_1(kb) \tag{A.7.15}$$

and

$$N(\rho, \tau) = \int_0^\infty b\, J_1(kb)\, J_0(k\rho)\, \mathrm{Cos}(\omega\tau)\, dk \tag{A.7.16}$$

The results of Eq. (A. 7. 16) for b = 3 and b = 20 are given in Figs. A. 7. 3 and A. 7. 4.

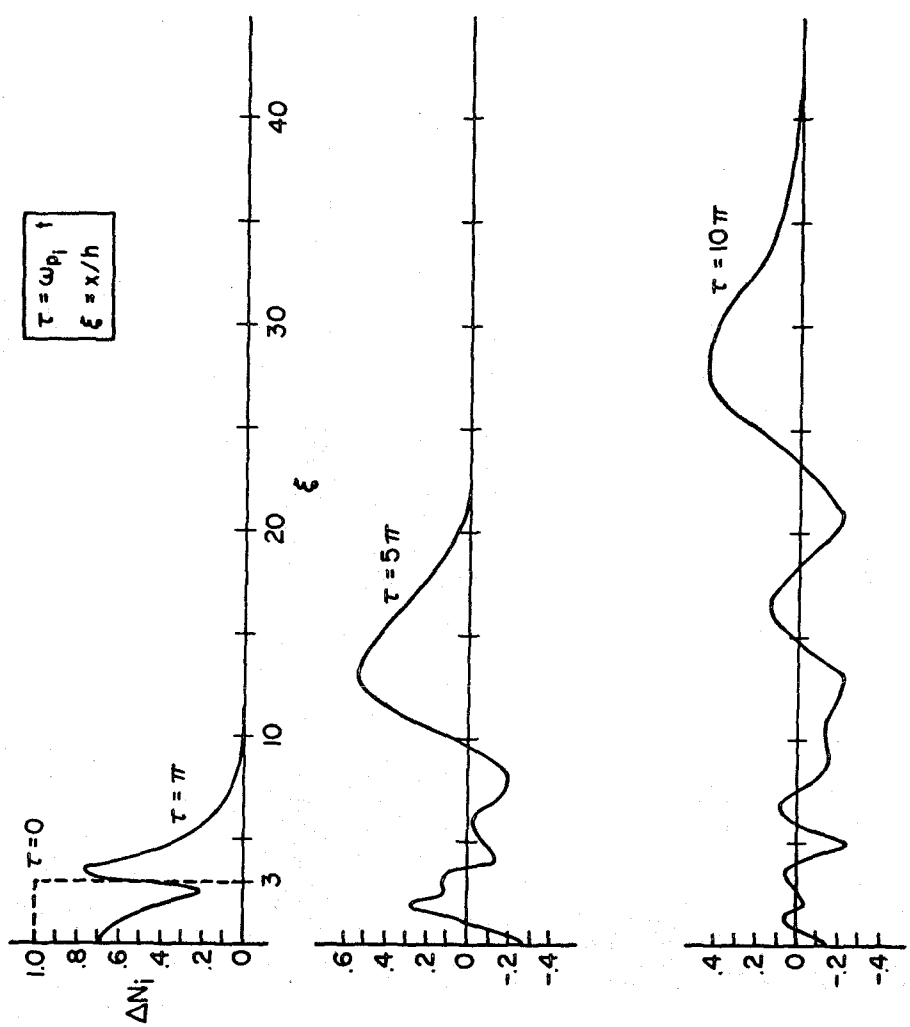

Figure A. 7. 1 Development of a One-dimensional Step Function Density Disturbance (2b/h = 6).

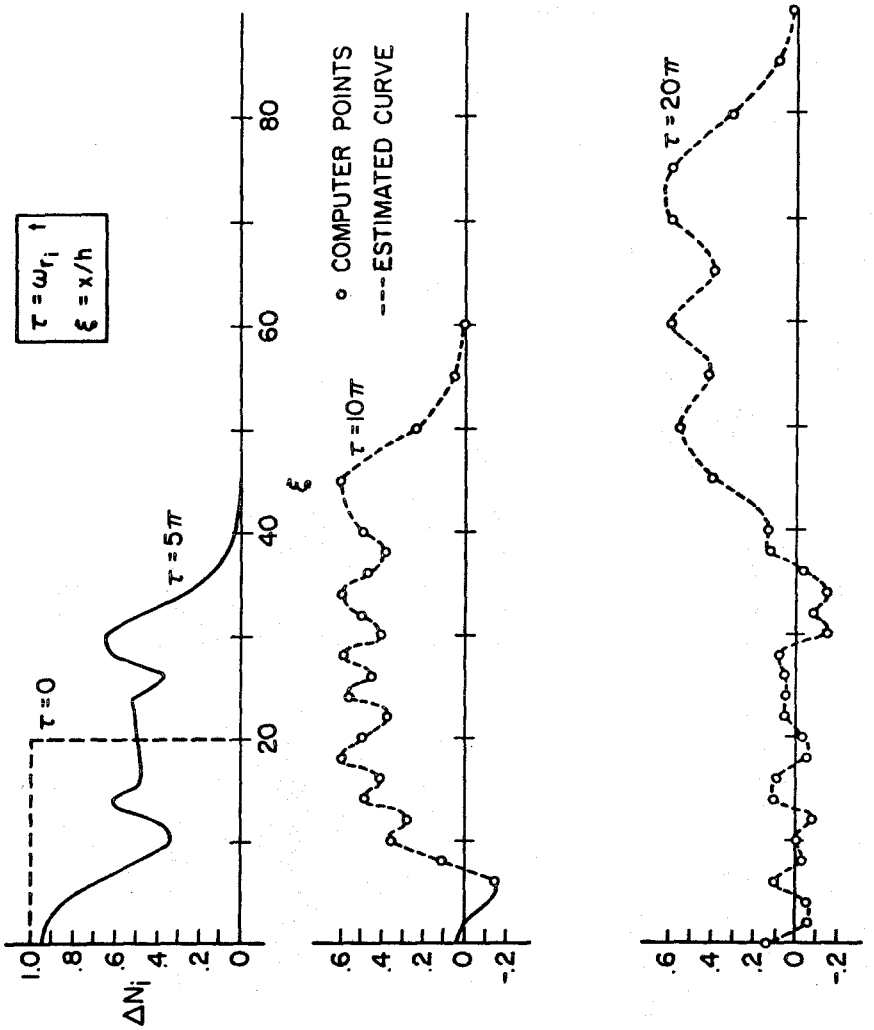

Figure A. 7. 2 Development of a One-dimensional Step Function Density Disturbance (2b/h = 40).

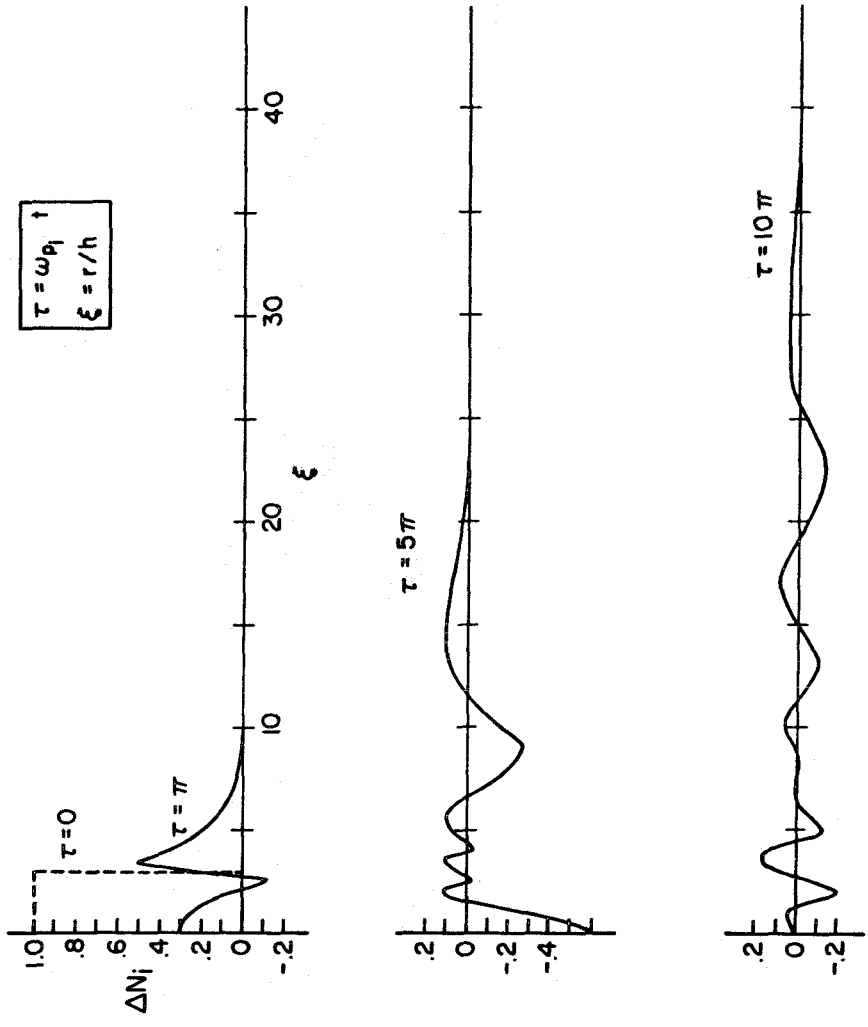

CYLINDRICAL CASE

STEP FUNCTION INITIAL DISTRIBUTION (b=3)

Figure A. 7. 3 Development of a Cylindrical Step Function Density Disturbance (2b/h = 6).

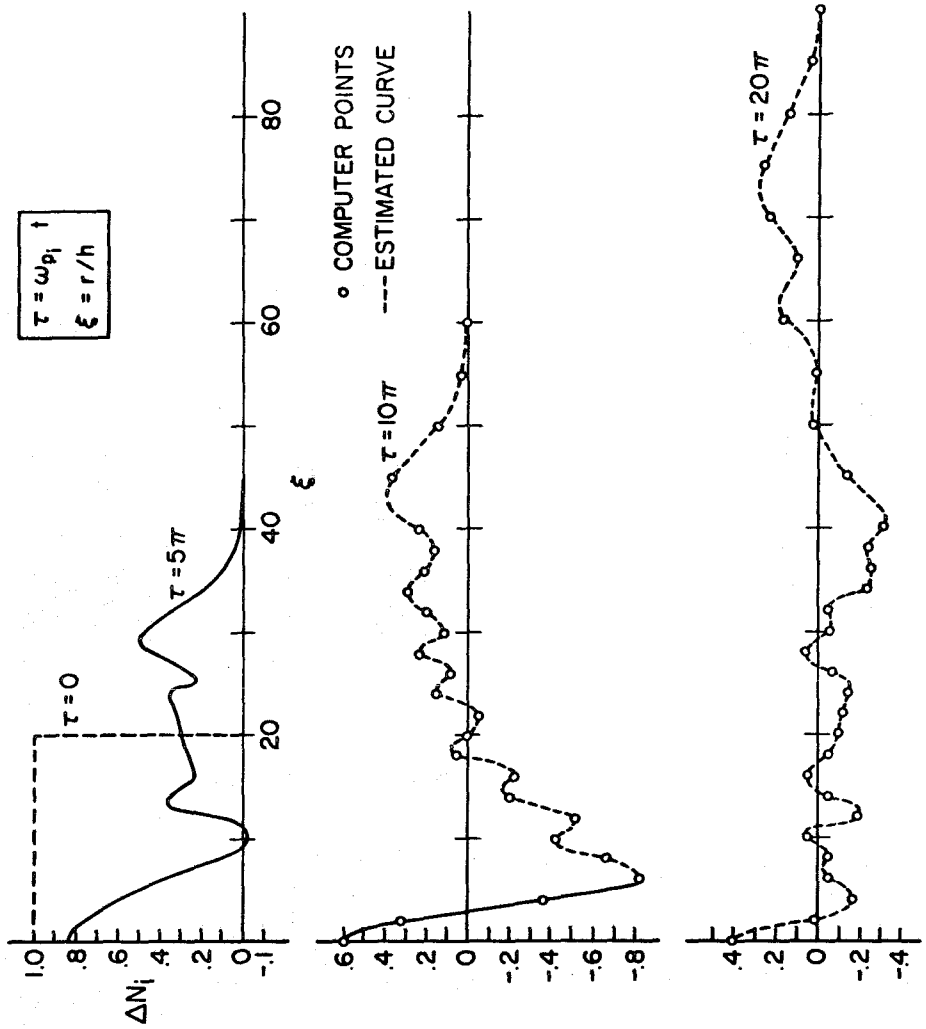

Figure A. 7. 4 Development of a Cylindrical Step Function Density Disturbance (2b/h = 40).

REFERENCES

1. Rand, S. and Albini, F.: "Radar Return from Vehicles in the Ionosphere," AIAA J. 5:6 (1967).

2. Al'pert, Ya. L., Gurevich, A. V. and Pitaevskii, L. P.: Space Physics with Artificial Satellites, Consultants Bureau, New York (1965).

3. de Leeuw, J. H.: "A Brief Introduction to Ionospheric Aerodynamics," Rarefied Gas Dynamics, Suppl. 4, Vol. II (C. L. Brundin, ed.), 1561-1586, Academic Press, New York (1967).

4. Al'pert, J. L., Gurevic, A. V. and Pitaevskii, L. P.: "Effects Due to an Artificial Earth Satellite in Rapid Motion Through the Ionosphere or the Interplanetary Medium," Space Sci. Rev. 2, 680-748 (1963).

5. Rand, S.: "Wake of a Satellite Traversing the Ionosphere," Phys. Fl. 3, 265-273 (1960).

6. Kraus, L. and Yoshihara, H.: "Electrogasdynamic Motion of a Charged Body in a Plasma," J. Aero. Space Sci. 27, 229-233 (1960).

7. Davis, A. H. and Harris, I.: "Interaction of a Charged Satellite with the Ionosphere," Rarefied Gas Dynamics, Suppl. 1 (L. Talbot, ed.), 691-699, Academic Press, New York (1961).

8. Kiel, R. E., Gey, F. C. and Gustafson, W. A.: "Electrostatic Potential Fields of an Ionosphere Satellite," AIAA J. 6, 690-694 (1968).

9. Singer, S. F.: Interactions of Space Vehicles with an Ionized Atmosphere, Pergamon Press (1965).

10. Liu, V. C. and Jew, H.: "Near Wake of the Rarefied Plasma Flows at Mesothermal Speeds," AIAA Paper No. 68-169 (1968).

11. Pan, Y. S. and Vaglio-Laurin, R.: "Trail of an Ionospheric Satellite I," AIAA J. 10, 1801 (1967).

12. Pan, Y. S. and Vaglio-Laurin, R.: "Trail of an Ionospheric Satellite II," Rarefied Gas Dynamics, Suppl. 4, Vol. II (C. L. Brundin, ed.), 1687-1702, Academic Press, New York (1967).

13. Taylor, J. C.: "Disturbance of a Rarefied Plasma by a Supersonic Body on the Basis of the Poisson-Vlasov Equations-II," Planet. Space Sci. 15, 463 (1967).

References (Cont'd)

14. Taylor, J. C.: "Disturbance of a Rarefied Plasma by a Supersonic Body on the basis of the Poisson-Vlasov Equations--II," Planet. Space Sci. 15, 463 (1967).

15. Maslennikov, M. V. and Sigov, Yu S.: "Discrete Model of Medium in a Problem on Rarefied Plasma Stream Interaction with a Charged Body," Rarefied Gas Dynamics, Suppl. 4, Vol. II (C. L. Brundin, ed.), 1657-1670, Academic Press, New York (1967).

16. Maslennikov, M. V., Sigov, Yu S. and Churkina, G. P.: "Numerical Experiments on Flow of Rarefied Plasma Around Bodies of Various Shapes. 1," Cosmic Investigations, 6:2, 220-227 (1968).

17. Maslennikov, M. V. and Sigov, Yu. S.: "Plasma Stream interaction with charged bodies of various forms," Rarefied Gas Dynamics, Suppl. 5 (L. Trilling and H. Wachman, eds.) Acad. Press, N. Y. (1969).

18. Samir, U. and Willmore, A. P.: "The Equilibrium Potential of a Spacecraft in the Ionosphere," Planetary and Space Sci. 14, 1131-1137 (1966).

19. Samir, U. and Willmore, A. P.: "The Distribution of Charged Particles Near a Moving Spacecraft," Planetary and Space Sci. 13, 285-296 (1965).

20. Madved, D. B.: "Experimental Measurements of Ion Wake and Body Effects with the Gemini/Agena Satellite," Rarefied Gas Dynamics, Suppl. 5, (L. Trilling and H. Wachman, eds.), Academic Press, New York (1969).

21. Meckel, B. B.: "Experimental Study of the Interaction of a Moving Body with a Plasma," Rarefied Gas Dynamics Symposium, 701-714 (1961).

22. Pitts, W. C. and Knechtel, E. D.: "Experimental Investigation of Electric Drag on Spherical Satellite Models," NASA TN D-3619, Feb. 1965.

23. Hall, D. F., Kemp, R. F. and Sellen, J. M. Jr.: "Plasma-Vehicle Interaction in a Plasma Stream" AIAA J. 2, 1032-1039, (1964).

24. Clayden, W. A. and Hurdle, C. V.: "An Experimental Study of Plasma-Vehicle Interaction," Fifth Rarefied Gas Dynamics Symposium, Vol. 2, 1717-1731 (1966).

References (Cont'd)

25. Skvortsov, V. V. and Nosachev, L. V.: "Cosmic Investigations 6 (1968).

26. Sajben, M. and Blumenthal, D. L.: "Experimental Study of a Rarefied Plasma Stream and its Interaction with Simple Bodies," AIAA Paper No. 69-79 (1969).

27. Hester, S. D. and Sonin, A. A.: " A Laboratory Study of the Electrodynamic Influences on the Wakes of Ionospheric Satellites," AIAA Paper No. 69-673 (1969).

28. Hester, S. D.: "A Laboratory Study of the Plasma Disturbance Produced by the Passage of a Satellite Through the Ionosphere," Ph. D. Thesis, M. I. T. (1969).

29. Mason, R. J.: Bulletin, Am. Phys. Soc. 14, 1043 (1969).

30. Mason, R J.: "Structure of Evolving Ion Acoustic Fronts in Collisionless Plasmas," Phys. of Fl. 13, 1042 (1970).

31. Moiseev, S. S. and Sagdeev, R. Z.: J. Nucl. Energy, Pt. C5, 43 (1963).

32. Hill, J.: Unpublished Ph. D. Thesis, Caltech (1966).

33. Lees, L.: Private Communication (1968).

34. Hayes, W. D. and Probstein, R. F.: Hypersonic Flow Theory, Vol. 1, Academic Press, New York (1966).

35. Kaufman, H. R.: "An Ion Rocket with an Electron-Bombardment Ion Source," NASA TN D-585 (1961).

36. Reader, P. D.: "Investigation of a 10 Centimeter Diameter Diameter Electron Bombardment Ion Rocket," NASA TN D-1163 (1962).

37. Reader, P. D.: "The Operation of an Electron Bombardment Ion Source with Various Gases," First Int. Conv. on Electron and Ion Beam Sci. and Technology (1964).

38. Reader, P. D.: "Experimental Effects of Propellant-Introduction Mode on Electron-Bombardment Ion Rocket Performance," NASA TN D-2587 (1965).

39. Chen, F. F. "Electric Probes," Plasma Diagnostic Techniques (R. H. Huddlestone and S. L. Leonard, eds.), 113-200, Academic Press, New York (1965).

References (Cont'd)

40. Sonin, A. A.: "Free-molecule Langmuir Probe and its use in Flow Field Studies," AIAA J. 4, 1588 (1966).

41. Takayama, K., Ikegami, H. and Miyasaki, S.: "Plasma Resonance in a Radio Frequency Probe," Phys. Rev. Letters 5, 238-240 (1960).

42. Harp, R. S. and Crawford, F. W.: "Characteristics of the Plasma Resonance Probe," J. Appl. Phys. 35, 343 (1964).

43. Rapp, D. and Francis, W. E.: "Charge Exchange between Gaseous Ions and Atoms," J. Chem. Phys. 37, 2631-2645 (1962)

44. McDaniel, E. W.: Collision Phenomena in Ionized Gases, John Wiley and Sons, Inc. (1964).

45. Hasted, J. B.: Physics of Atomic Collisions, Butterworths, London, (1964).

46. Sajben, M.: "An Exact Solution for Axially Symmetric Equilibrium Electron Density Distributions," Phys. of Fluids 11, (1968).

47. Dwight, H. B.: Tables of Integrals and other Mathematical Data, McMillan (1961).